

Methods¹

H. Tobin, T. Hirose, D. Saffer, S. Toczko, L. Maeda, Y. Kubo, B. Boston, A. Broderick, K. Brown, A. Crespo-Blanc, E. Even, S. Fuchida, R. Fukuchi, S. Hammerschmidt, P. Henry, M. Josh, M.J. Jurado, H. Kitajima, M. Kitamura, A. Maia, M. Otsubo, J. Sample, A. Schleicher, H. Sone, C. Song, R. Valdez, Y. Yamamoto, K. Yang, Y. Sanada, Y. Kido, and Y. Hamada²

Chapter contents

Introduction and operations	1
Lithology	5
Structural geology	8
Biostratigraphy and paleomagnetism	10
Geochemistry	13
Physical properties	20
Downhole measurements	27
Logging	28
X-ray computed tomography	31
References	32
Figures	36
Tables	63

Introduction and operations

This section documents the methods used for shipboard measurements and analyses during Integrated Ocean Drilling Program (IODP) Expedition 348. During Expedition 348, we conducted riser drilling from 860.3 to 3058.5 meters below seafloor (mbsf) at Site C0002 (see Table T4 in the “Site C0002” chapter [Tobin et al., 2015]) as a continuation of riser drilling in Hole C0002F begun during Expedition 326 in 2010 (Expedition 326 Scientists, 2011) and deepened during Expedition 338 in late 2012 and early 2013 (Strasser et al., 2014b). Operations began with connection of the riser to the Hole C0002F wellhead and sidetrack drilling of the cement shoe at 860.3 mbsf to establish a new hole, parallel to previous Hole C0002F drilling but laterally offset by ~16 m. This new sidetrack was designated as Hole C0002N to distinguish it from the overlapping interval in Hole C0002F. Previous IODP work at Site C0002 included logging and coring for Nankai Trough Seismogenic Zone Experiment (NanTroSEIZE) Stages 1 and 2 during IODP Expeditions 314 (logging while drilling [LWD]), 315 (riserless coring), 326 (riser tophole installation), 332 (LWD and long-term monitoring observatory installation), and 338 (riser drilling and riserless coring) (Expedition 314 Scientists, 2009; Expedition 315 Scientists, 2009b; Expedition 326 Scientists, 2011; Expedition 332 Scientists, 2011; Strasser et al., 2014b).

During riser operations, we collected drilling mud gas, cuttings, downhole logs by LWD instruments, downhole pressure data, flow data, core samples, and drilling parameters (including mud flow rate, weight on bit, and torque, among others). Gas from drilling mud was analyzed in near-real time in a mud-gas monitoring laboratory and was sampled for further postexpedition research. Continuous LWD data were collected and displayed in real time (except for a loss of measurement-while-drilling [MWD] telemetry during drilling to total depth in Hole C0002P) for quality control and for initial assessment of borehole environment and formation properties. Recorded-mode LWD data provided higher spatial sampling of downhole parameters and conditions. Cuttings were sampled for standard shipboard analyses and for shore-based research. Coring of a portion of Hole C0002P provided core for standard shipboard and shore-based research. Additionally, Hole C0002M was drilled to 512.5 mbsf as a test of the developmental small-diameter rotary core barrel (SD-RCB) system, and

¹Tobin, H., Hirose, T., Saffer, D., Toczko, S., Maeda, L., Kubo, Y., Boston, B., Broderick, A., Brown, K., Crespo-Blanc, A., Even, E., Fuchida, S., Fukuchi, R., Hammerschmidt, S., Henry, P., Josh, M., Jurado, M.J., Kitajima, H., Kitamura, M., Maia, A., Otsubo, M., Sample, J., Schleicher, A., Sone, H., Song, C., Valdez, R., Yamamoto, Y., Yang, K., Sanada, Y., Kido, Y., and Hamada, Y., 2015. Methods. In Tobin, H., Hirose, T., Saffer, D., Toczko, S., Maeda, L., Kubo, Y., and the Expedition 348 Scientists, *Proc. IODP*, 348: College Station, TX (Integrated Ocean Drilling Program). doi:10.2204/iodp.proc.348.102.2015

²Expedition 348 Scientists' addresses.



four cores were taken from 475 to 512.5 mbsf. These SD-RCB cores are currently designated as the “R” core type in the data management system, but they differ from normal RCB cores in that they are larger in diameter: 73 mm instead of 66 mm.

Site C0002 drilling operations

Operations at Site C0002 during Expedition 348 were entirely riser drilling. With the riser attached to the wellhead, drilling mud was circulated to clean the hole of cuttings, prevent wellbore failure, and maintain borehole pressure to balance stresses and pore pressure in the formation. IODP riser drilling on the D/V *Chikyu* differs from riserless drilling in ways that impact science, most notably in that cuttings can be collected continuously whenever the drill bit is advancing, and core physical properties and chemistry may be affected by the invasion of components of drilling mud (e.g., Saffer, McNeill, Byrne, Araki, Toczko, Eguchi, Takahashi, and the Expedition 319 Scientists, 2010).

Continuous monitoring of mud weight, annular pressure, mud loss, and other circulation data during riser drilling can provide useful constraints on formation pore fluid pressure and state of stress (e.g., Zoback, 2007). Problems related to mud weight or hole collapse may impact successful drilling or casing of the borehole itself, as well as the ability to conduct downhole measurements or to achieve post-drilling scientific objectives, including observatory installations and active source seismic experiments. Because riser drilling remains relatively new in IODP, we follow recent proceedings from Expeditions 319 and 338 to describe key observations related to downhole (borehole) pressure, mud weight, and hole conditions during drilling of Holes C0002N and C0002P.

Reference depths

Depths of each measurement or sample are here reported referenced to the drilling vessel rig floor (rotary table) in meters below rotary table (m BRT) and meters below seafloor (mbsf) (Table T1). These depths are determined by drill pipe and wireline length and are correlated to each other by use of distinct reference points. Drilling engineers refer to pipe length when reporting depth and report it as drilling depth below rig floor (DRF) in meters. Core depths are based on drilling depth below rig floor to the top of the cored interval and curated length of the recovered core. During Expedition 348, core depths were converted to core depth below seafloor, method A (CSF-A), which allows overlap relative to cored interval and section boundaries in cases of >100% core recovery due to expansion after coring (see IODP

depth terminology at www.iodp.org/program-policies). Cuttings and mud depths are reported as mud depth below rig floor (MRF) or mud depth below seafloor (MSF), based on DRF and the calculated lag depth of the cuttings (see below for further details).

In referring to LWD results, depth was measured as LWD depth below rig floor (LRF) and sometimes reported as LWD depth below seafloor (LSF) (see “Logging” for further details). Depths reported in DRF and MRF are converted to depths below seafloor (drilling depth below seafloor [DSF] or CSF-A and mud depth below seafloor [MSF], respectively) by subtracting water depth and the height of the rig floor rotary table from the sea surface (28.5 m), with corrections relative to drilling depth where appropriate. These depths below seafloor (DSF, CSF-A, MSF, and LSF) are therefore all referenced to an equivalent datum. Seismic depths are reported in either time (seconds) or depth (meters). For time sections, a two-way traveltime in seconds is used. For depth sections, seismic depth below seafloor (SSF) or seismic depth below sea level (SSL) are used.

Because Holes C0002N and C0002P are sidetracked holes (see “Site C0002 drilling operations” for further details), there is a ~1–2 m difference between the true vertical depth and the measured depth along the hole that is used for all onboard measurements. Therefore, a measured depth (MD-m BRT and MD-mbsf) as well as a true vertical depth (TVD-m BRT and TVD-mbsf) are defined for any position along the boreholes. Because the difference is small, we used measured depth rather than true vertical depth for all measurements reported in this volume, unless otherwise explicitly noted (i.e., in this volume “mbsf” refers to “MD-mbsf” everywhere). Correlations between measured and true vertical depths at key depths, such as casing shoe and unit boundaries, are summarized in Table T2.

Although all of these depths are defined explicitly (Table T1), depths are reported throughout the Site C0002 chapter simply in mbsf or m BRT in most cases, unless a specific distinction is drawn among logging, coring, and mud depths for a given value.

Cuttings and mud depths

During riser drilling, drilling mud circulates down the drilling pipe, out at the drill bit, then up the borehole annulus into the riser pipe, and back up to the drillship. As the drill bit cuts through the formation, cuttings are suspended in the drilling mud and carried with the drill mud, formation fluid, and formation gas back to the ship. A cuttings sample is assumed to be a mixture of rock fragments, sediment, and drilling fluid from the sampled interval. The time between when the formation is cut by the drill

bit and when these cuttings arrive at the ship is known as the “lag time,” which is a function of drilling mud pumping rate and annular mud volume, and is used to calculate the “lag depth.” At a constant pump rate, lag time and lag depth increase as the hole is deepened and the volume of circulating mud increases. All of the depths recorded for cuttings and mud gas in Holes C0002N and C0002P have been corrected for this calculated lag. Because cuttings disperse and mix as they are carried to the surface, any given cuttings sample is believed to be representative of a depth-averaged volume; precision of their depth of origin is assumed to be ~5 m under normal conditions, and it is always possible that cavings and material from higher positions in the hole can be present at misleading lag depth.

Sampling and classification of material transported by drilling mud

A total of 293 cutting samples between 870.5 and 2330 mbsf and 231 cutting samples between 2107.5 and 3058.5 mbsf were collected during drilling in Holes C0002N and C0002P, respectively (see Hole C0002N and C0002P cuttings smear slides in SMEARSLD in “[Supplementary material](#)”). Cuttings were collected at every 5 m depth interval from the shale shakers. Drilling mud and mud gas were also regularly sampled during drilling (see “[Geochemistry](#)”). Mud gas, fluid, and cuttings samples were classified by drill site and hole using a sequential material number followed by an abbreviation describing the type of material. The material type identifiers are

SMW = solid taken from drilling mud (cuttings),
 LMW = liquid taken from drilling mud, and
 GMW = gas taken from drilling mud.

Additional information for individual samples (e.g., cuttings size fraction) is provided in the comments section of the J-CORES database and reported in the report text as, for example, “348-C0002N-123-SMW, 1–4 mm” (for the 1–4 mm size fraction aliquot of the one hundred twenty-third cuttings sample recovered from Hole C0002N during Expedition 348).

Influence of drilling mud composition on cuttings

Because of the recirculation of drilling mud and continuous production of formation cuttings and fluids, contamination of cuttings samples is common. Expedition 319 Scientists (2010b) discuss the possible effects of contamination on different types of measurements. New observations of contamination and artifacts induced by riser drilling operation and further QA/QC analysis during Expedition 348 were

performed and are reported in the individual methods and site chapters.

Cuttings handling

Every 5 m between 870.5 and 2330 mbsf in Hole C0002N and between 2107.5 and 3058.5 mbsf in Hole C0002P, we routinely collected 2500–4500 cm³ of drilling mud containing cuttings from the shale shaker for onboard analysis, long-term archiving, and personal samples for shore-based postexpedition research. The variable initial sampling volume from the shale shaker is due to varying amounts of personal research samples needed at a specific depth. Between 870.5 and 2330 mbsf, the Marine Works Japan technicians processed all samples following the standard shipboard analysis procedure outlined below, excluding lithologic and structural description and micropaleontological investigation, because the science party had not yet boarded. Description of cuttings at every 10 m interval, as well as additional shipboard measurement and analysis at selected depth intervals, was performed after the science party embarked. Archive samples and an archive split of all processed cuttings samples were sent to the Kochi Core Center (KCC) (Japan) for permanent archiving.

The standard cutting laboratory flow is summarized in Figure F1. Unwashed cuttings samples were taken for the following objectives:

- 70 cm³ for lithology description and
- 400 cm³ for measuring natural gamma radiation (NGR) (see “[Physical properties](#)” for further details) and archiving at the KCC.

The remaining cuttings were washed gently with seawater in a 250 µm sieve at the core cutting area. Samples were then further washed and sieved with seawater using 0.25, 1, and 4 mm mesh. During sieving, a hand magnet was used to remove iron contaminants originating from drilling tools and casing. Cuttings were separated by size fraction as 0.25–1, 1–4, and >4 mm. Splits of the 1–4 and >4 mm fractions were used for bulk moisture and density (MAD) measurements.

For Hole C0002N, 220 cm³ of the 1–4 and >4 mm fractions was vacuum dried. Aliquots (15 cm³) from each size fraction were sent as bulk samples for grinding for X-ray diffraction (XRD), X-ray fluorescence (XRF), and organic geochemistry analysis (total organic carbon [TOC], total carbon [TC], and total nitrogen [TN]). The remaining cuttings were described and analyzed for structures and lithology, including microscopy-based observations of thin sections from selected cuttings. On the other hand, for Hole C0002P, washed >4 mm fractions before vac-

uum drying were sent for structural description. The samples were hand-washed to pick up intact cuttings (see “**Structural geology**”), were described, and the intact cuttings which exhibited no deformation were used for MAD.

Occasionally after dividing and description, samples of interest that were divided by major and minor lithology were selected for additional XRD, XRF, TOC, TC, and TN analysis.

For description and analysis of cuttings during Expedition 348, cuttings samples were divided into three types: (1) drilling-induced cohesive aggregate (DICA), (2) pillowed cuttings, and (3) intact (or formation) cuttings (Fig. F2). DICAs were first defined during Expedition 338 as an aggregate that contains less-sorted angular mineral grains and fragments of small formation cuttings in a drilling-mud matrix (Strasser et al., 2014a). These were characteristically easily disaggregated when exposed to water. Their properties are considered not representative of the in situ formation. Pillowed cuttings, the most abundant type of cuttings, were characterized by an accordion-like surface, likely formed by drill bit cutting action, and therefore also significantly altered from their in situ condition. Intact cuttings are considered to represent the formation and were collected by handpicking during the washing and sieving processes. Types of cuttings used for onboard description and standard measurements are summarized in Table T3.

Drilling mud handling

Drilling mud samples were collected at two locations, the mud tanks and the mud return ditch. Sampling was carried out regularly every 2–3 days. Drilling mud samples were used for measuring background and contamination effects for NGR, interstitial water (IW), and carbon analysis (see “**Physical properties**” and “**Organic geochemistry**”). Additional mud-gas samples were collected once every 12 h (100 mL each) for archiving as reference material.

Mud-gas handling

Mud gas was extracted from drilling mud immediately after the mud returned from the borehole. A degasser with an agitator was installed on the bypass mudflow line, and the gas extracted in the degasser chamber was pumped to the mud-gas monitoring laboratory through a polyvinyl chloride tube. After problems were identified in producing adequate levels of extracted gas, the degasser unit was moved to the mud return ditch, just “upstream” of the shale shakers. Analysis in the unit is described in “**Geochemistry.**”

Core handling

Standard IODP coring tools, including plastic core liners (6.6 cm in inner diameter), were used in Hole C0002P. In addition to the standard tools, SD-RCB coring with both plastic and aluminum core liners was tested at 475–512.5 mbsf in Hole C0002M. Cores were typically cut into ~1.4 m sections at the core cutting area and logged and labeled by the onboard curator.

Figure F3 shows the basic core processing flow chart. A small volume (~5–10 cm³) of sample was taken for micropaleontology from the core catcher section. For time-sensitive whole-round sampling for interstitial water analysis, microbiological analysis, and anelastic strain recovery (ASR), selected core sections were first run through the X-ray computed tomography (XRCT) scanner to identify suitable interval for sampling. Core watchdogs then ensured that the samples could be used and did not contain any critical structures. Interstitial water sample lengths varied depending on core recovery and estimated volumetric fluid in the formation. Microbiological and ASR samples were ~10 cm long. All other core sections were taken to the core processing deck for standard XRCT scanning and core logging with the whole-round multisensor core logger (MSCL-W).

After XRCT scanning and MSCL-W logging, community and approved personal research whole-round samples as long as ~20 cm were taken where intact, relatively homogeneous sections could be identified. The number of community whole rounds was limited by core recovery and core quality. All whole rounds were stored at 4°C. Adjacent to whole-round samples (including the time-sensitive, community, and personal whole rounds), a cluster sample was taken at least once per section. The cluster sample is used for routine MAD, XRD, XRF, carbon, and nitrogen analyses shipboard. Some cluster samples were used for shore-based research on clay-fraction XRD and grain size analysis.

The core sections remaining after whole-round core sampling were split into working and archive halves. The former was used for structural description and sampling and the latter for lithological description. Digital images of archive-half sections were taken with the photo image logger (MSCL-I) before visual core description (VCD) by sedimentologists and color reflectance measurement by the color spectrometry logger (MSCL-C). Thermal conductivity measurements were performed on samples from the working half of the cores using the half-space method. Discrete cubes for *P*-wave velocity and impedance analysis were sampled from the working half. Additional samples were taken for MAD, XRD, XRF, and carbon analyses. After the expedition, all

cores were transported in refrigerated reefers for archiving at the KCC.

Authorship of site chapters

The separate sections of the site and “Methods” chapters were written by the following shipboard scientists (authors are listed in alphabetical order):

- Expedition summary: Expedition 348 Scientists
 - Logging: Boston, Jurado*, Sone
 - Lithology: Fukuchi, Maia, Schleicher*, Yang
 - Structural geology: Brown, Crespo-Blanc, Otsubo, Yamamoto*
 - Biostratigraphy/Paleomagnetism: Broderick, Kanamatsu (shore-based scientist)
 - Geochemistry: Even, Fuchida, Hammerschmidt, Sample*
 - Physical properties: Henry, Josh, Kitajima,* Kitamura, Valdez
 - Downhole Measurements: Saffer, Sone, Tobin
- * Team leader

Lithology

At Site C0002 (Holes C0002N and C0002P), cuttings data, core data between 2163 and 2217.5 mbsf in Hole C0002P, and LWD data (including NGR, resistivity imaging, ultraseismic caliper, and sonic data) were used to identify lithologic boundaries and units. Methods applied to core description during Expedition 348 draw upon the protocols of IODP Expeditions 315 (Expedition 315 Scientists, 2009a) and 338 (Strasser et al., 2014a), whereas methods applied to description of cuttings rely upon procedures established during Expedition 319 (Expedition 319 Scientists, 2010b), in particular the *Cuttings Cookbook* (Center for Deep Earth Exploration [CDEX], 2012).

Cuttings samples from Holes C0002N and C0002P were described based on the examination of a 70 cm³ aliquot of bulk cuttings. Descriptions included

- Macroscopic observations of percent silty claystone versus percent sandstone,
- Microscopic observations (including smear slides), and
- Bulk mineralogical data by XRD and bulk elemental data by XRF.

Depths reported for cuttings are on the MSF depth scale (Table T1).

Core samples were described based on

- Macroscopic observations following standard IODP VCD protocols and also observation of XRCT,
- Microscopic observations (including smear slides and thin sections),

- Bulk mineralogical data collected by XRD and bulk elemental data collected by XRF, and
- Intervals of interest selected for XRF core logger images.

Depths reported for cores and samples are on the CSF depth scale (Table T1). Figures F4 and F5 show the graphic patterns for the lithologies encountered in core and cuttings during Expedition 348.

Macroscopic observations of cuttings

Cuttings typically occur as small fragments of rock, generally 0.25–8 mm in size of various lithologies, produced during drilling. Cuttings were taken for the first time in IODP operations during Expedition 319 (Saffer, McNeill, Byrne, Araki, Toczko, Eguchi, Takahashi, and the Expedition 319 Scientists, 2010). Sampling and analysis of cuttings follow the *Cuttings Cookbook* (CDEX, 2012) developed during Expedition 319, with some additions and modifications. Cuttings were separated by sieving by laboratory technicians into rock-chip fractions of different sizes (0.25–1, 1–4, and >4 mm). However, at shallow depths solid fragments from the formation are sometimes suspended in drilling mud and mixed with trace amounts of clay-bearing drilling additives (e.g., bentonite). Rigorous separation of drilling-related mud from formation cuttings is not always possible, especially in the case of very soft cuttings. This hampers quantification of the true clay content. The procedure for separating cuttings from drilling mud and the division into different sizes is explained in the *Cuttings Cookbook* (CDEX, 2012).

Cuttings were collected at 5 m intervals at 875.5–2330 and 1941.5–3058.5 mbsf in Holes C0002N and C0002P, respectively, with samples analyzed and described every 10 m. Based on general visual observations of the bulk cleaned cuttings material, we estimated the relative amount of silty claystone and sandstone; the consolidation state; the shape; and the occurrence of wood, fossils, and artificial contamination (Fig. F5). All macroscopic observations were recorded on visual cuttings description forms and summarized in VCDSCAN in “[Supplementary material](#).”

Macroscopic observations of core

We followed conventional Ocean Drilling Program (ODP) and IODP procedures for recording sedimentologic information on VCD forms on a section-by-section basis (Mazzullo and Graham, 1988). VCDs were transferred to section-scale templates using J-CORES software and then converted to core-scale depictions using Strater (Golden Software). Texture, which is defined by the relative proportions of sand,

silt, and clay, follows the classification of Shepard (1954). The classification scheme for siliciclastic lithologies follows Mazzullo et al. (1988).

Where applicable in core, bioturbation intensity in deposits was estimated using the semiquantitative ichnofabric index as described by Droser and Bottjer (1986, 1991). The index refers to the degree of biogenic disruption of primary fabric such as lamination and ranges from 1 for nonbioturbated sediment to 6 for total homogenization:

- 1 = No bioturbation recorded; all original sedimentary structures preserved.
- 2 = Discrete, isolated trace fossils; <10% of original bedding disturbed.
- 3 = Approximately 10%–40% of original bedding disturbed. Burrows are generally isolated but locally overlap.
- 4 = Last vestiges of bedding discernible; ~40%–60% disturbed. Burrows overlap and are not always well defined.
- 5 = Bedding is completely disturbed, but burrows are still discrete in places and the fabric is not mixed.
- 6 = Bedding is nearly or totally homogenized.

The ichnofabric index in cores was identified with the help of visual comparative charts (Heard and Pickering, 2008). Distinct burrows that could be identified as particular ichnotaxa were also recorded.

The Graphic lithology column on each VCD plots all beds that are ≥ 2 cm thick to scale. Interlayers <2 cm thick are identified as laminae in the Sedimentary structures column. It is difficult to discriminate between the dominant lithologies of silty claystone and clayey siltstone without quantitative grain-size analysis; therefore, we grouped this entire range of textures into the category “silty claystone” on all illustrations. A more detailed description of rock texture was attempted on the smear slide description sheets, which are provided (see smear slides in “[Core descriptions](#)”). Separate patterns were not used for more heavily indurated examples of the same lithologies (e.g., silty clay versus silty claystone) because the dividing line is arbitrary. Figure F4 shows symbols for sedimentary structures, soft-sediment deformation structures, severity of core disturbance, and features observed in XRCT images in both soft sediment and indurated sedimentary rock.

X-ray computed tomography

XRCT imaging provided real-time information for core logging and sampling strategies. We used a methodology similar to that used during Expedition 316 (Expedition 316 scientists, 2009). XRCT scans were used routinely during this expedition on all

core samples. XRCT scanning was done immediately after cores were cut into sections so that time-sensitive whole-round samples (e.g., those for interstitial water) could be included in this screening process. The scans were used to provide an assessment of core recovery, determine the appropriateness of whole-round and interstitial water sampling (e.g., to avoid destructive testing on core samples with critical structural features), identify the location of subtle features that warrant detailed study and special handling during visual core description and sampling, and determine the 3-D geometry, crosscutting and other spatial relations, and orientation of primary and secondary features.

Microscopic observation of cuttings

Microscopic investigations of the washed >63 μm sand-sized fraction using a binocular microscope allowed us to distinguish different minerals in the sand-sized fraction of the sediment; their abundance, roundness, and sorting; and the relative abundances of wood/lignite fragments and fossils. The mineralogy in the mudstone could not be determined because of the small grain sizes of the minerals. The data are summarized in “[Lithology](#)” and Figure F8 in the “Site C0002” chapter (Tobin et al., 2015) (see also VCDSCAN in “[Supplementary material](#)”). Errors can be large, however, especially for fine silt- and silt-sized fractions. Thus, it would be misleading to report values as exact percentages. Instead, the visual estimates are grouped into the following categories:

- D = dominant (>50%).
- A = abundant (>10%–50%).
- C = common (>1%–10%).
- F = few (0.1%–1%).
- R = rare (<0.1%).

Smear slides

Smear slides are useful for identifying and reporting basic sediment attributes (texture and composition) in samples of both cuttings and cores, but the results are semiquantitative at best (Marsaglia et al., 2013). We estimated the abundance of biogenic, volcanoclastic, and siliciclastic constituents using a visual comparison chart (Rothwell, 1989). Cuttings pieces were chosen for smear slide production based upon the dominant lithology present in a given interval. If a distinct minor lithology was abundant, an additional smear slide was made for that interval. For cuttings, we estimated the percentage of minerals observed, normalized to 100%. Smear slide images and scanned smear slide forms of cuttings are presented in the SMEARSLD folder in “[Supplementary material](#).”

For core, estimates of sand, silt, and clay percentages were entered into the J-CORES samples database along with abundance intervals for the observed grain types, as given above. Additional observations, including visual estimates for normalized percentages of grain size and mineral abundance, were handwritten on the paper smear slide forms, which were scanned and are included in SMEARSLD in **“Supplementary material.”** The sample location for each smear slide was entered into the J-CORES database with a sample code “SS.” The relative abundance of major components was also validated by XRD (see **“X-ray diffraction”**), and the absolute weight percent of carbonate was verified by coulometric analysis (see **“Geochemistry”**).

Smear slides were observed in transmitted light using an Axioskop 40A polarizing microscope (Carl Zeiss) equipped with a Nikon DS-Fi1 digital camera.

X-ray diffraction

The principal goal of XRD analysis of cuttings and cores was to estimate the relative weight percentages of total clay minerals, quartz, feldspar, and calcite from peak areas. For cuttings, XRD analysis was conducted on a 10 g subsample of the 1–4 mm size fraction every 10 m. These measurements were also made on the >4 mm size fraction, for comparison. For cores, material for XRD was obtained from a 10 cm³ sample that was also used for XRF and carbonate analyses. All samples were vacuum-dried, crushed with a ball mill, and mounted as randomly oriented bulk powders. Routine powder XRD analyses of bulk powders were performed using a PANalytical CubiX PRO (PW3800) diffractometer. XRD instrument settings were as follows:

Generator = 45 kV.
 Current = 40 mA.
 Tube anode = Cu.
 Wavelength = 1.54060 (K α 1) and 1.54443 (K α 2) Å.
 Step spacing = 0.005°2 θ .
 Scan step time = 0.648 s.
 Divergent slit = automatic.
 Irradiated length = 10 mm.
 Scanning range = 2°–60°2 θ .
 Spinning = yes.

In order to maintain consistency with previous NanTroSEIZE results, we used the software MacDiff 4.2.5 for data processing (<http://www.ccp14.ac.uk/ccp/web-mirrors/krumm/macsoftware/macdiff/MacDiff.html>). We adjusted each peak's upper and lower limits following the guidelines shown in Table T4. Calculations of relative mineral abundance utilized a matrix of normalization factors derived from integrated peak areas and singular value decomposition

(SVD). As described by Fisher and Underwood (1995), calibration of SVD factors depends on the analysis of known weight-percent mixtures of mineral standards that are appropriate matches for natural sediment. SVD normalization factors were recalculated during Expeditions 315 and 338 after the diffractometer's high-voltage power supply and X-ray tube were replaced (Expedition 315 Scientists, 2009a). The mixtures were rerun at the beginning of Expedition 348 (Table T5). Bulk powder mixtures for the Nankai Trough are the same as those reported by Underwood et al. (2003): quartz (Saint Peter sandstone), feldspar (Ca-rich albite), calcite (Cyprus chalk), smectite (Ca-montmorillonite), illite (Clay Mineral Society IMt-2, 2M1 polytype), and chlorite (Clay Mineral Society CCa-2). Examples of diffractograms for standard mixtures are shown in Figure F6.

Average errors (SVD-derived estimates versus true weight percent) of the standard mineral mixtures are total clay minerals = 3.3%; quartz = 2.1%; plagioclase = 1.4%, and calcite = 1.9%. Despite its precision with standard mixtures, the SVD method is only semi-quantitative, and results for natural specimens should be interpreted with caution. One of the fundamental problems with any bulk powder XRD method is the difference in peak response between poorly crystalline minerals at low diffraction angles (e.g., clay minerals) and highly crystalline minerals at higher diffraction angles (e.g., quartz and plagioclase). Clay mineral content is best characterized by measuring the peak area, whereas peak intensity may more accurately quantify quartz, feldspar, and calcite. Analyzing oriented aggregates enhances basal reflections of the clay minerals, but this is time consuming and requires isolation of the clay-sized fraction to be effective. For clay mineral assemblages in bulk powders, the two options are to individually measure one peak for each mineral and add the estimates together (thereby propagating the error) or to measure a single composite peak at 19.4°–20.4°2 θ . Other sources of error are contamination of mineral standards by impurities such as quartz (e.g., the illite standard contains ~20% quartz) and differences in crystallinity between standards and natural clay minerals. For trace quantities of a mineral and peaks with low intensity, use of negative SVD normalization factors may result in negative values of absolute weight percent. In such cases, we inserted the numerical value of 0.1% as a proxy for “trace.”

Therefore, calculated mineral abundances should be regarded as relative percentages within a four-component system of clay minerals + quartz + feldspar + calcite. How close those estimates are to their absolute percentages within the total solids depends on the abundance of amorphous solids (e.g., biogenic

opal and volcanic glass), as well as the total of all other minerals that occur in minor or trace quantities. For most natural samples, the difference between calculated and absolute abundance percentage is probably between 5% and 10%. To compound the error, the XRD data from cuttings show effects of contamination by drilling fluid. The severity of these artifacts is especially obvious in the calculated values of percent calcite. Figures and tables are available in “**Lithology**” in the “Site C0002” chapter (Tobin et al., 2015).

X-ray fluorescence

Analyses were obtained in two modes: analysis of whole-rock powders and scanning of the whole-core surface on some selected intervals.

Whole-rock quantitative XRF spectrometry analysis was undertaken for major elements on cuttings and cores. For cuttings, XRF analysis was conducted on a 10 g powdered subsample of the 1–4 mm size fraction every 10 m. These measurements were also made on the >4 mm size fraction for comparison. For cores, material for XRF was obtained from a 10 cm³ sample that was also used for XRD and carbonate analyses.

For both cuttings and cores, all samples were vacuum-dried and crushed with a ball mill. Major elements were measured using the fused glass bead method and are presented as weight percent oxide proportions (Na₂O, MgO, Al₂O₃, SiO₂, P₂O₅, K₂O, CaO, TiO₂, MnO, and Fe₂O₃). An aliquot of 0.9 g of ignited sample powder was fused with 4.5 g of SmeltA12 flux for 7 min at 1150°C to create glass beads. Loss on ignition (LOI) was measured using weight changes on heating at 1000°C for 3 h. Analyses were performed on the wavelength-dispersive XRF spectrometer Supermini (Rigaku) equipped with a 200 W Pd anode X-ray tube at 50 kV and 4 mA. Analytical details and measuring conditions for each component are given in Table T6. Rock standards of the National Institute of Advanced Industrial Science and Technology (Geological Survey of Japan) were used as the reference materials for quantitative analysis. Table T7 lists the results for selected standard samples. A calibration curve was created with matrix corrections provided by the operating software, using the average content of each component. Processed data were uploaded into an Excel spreadsheet and are shown in “**Lithology**” in the “Site C0002” chapter (Tobin et al., 2015).

XRF core scanning

XRF core scanning analysis was performed using the JEOL TATSCAN-F2 energy dispersive spectrometry–

based core scanner (Sakamoto et al., 2006). The Rh X-ray source was operated at 30 kV accelerating voltage and a current of 0.170 mA. Data are reported as total counts on the peak and also as semiquantitative oxide weight percent. Semiquantitative analysis was performed using a 200 s accumulation. The following oxides were measured: Na₂O, MgO, Al₂O₃, SiO₂, P₂O₅, K₂O, CaO, TiO₂, MnO, and Fe₂O₃. This is the same methodology as the one used during Expeditions 316 (Expedition 316 Scientists, 2009) and 338 (Strasser et al., 2014a). The archive half was scanned because this technique is nondestructive to the core material. Sections 348-C0002P-5R-4, 35–91 cm, and 5R-5, 0–59 cm, were scanned at a spatial resolution of 0.5 cm and an analytical spot size of 1 cm × 1 cm. The scanning line was located along the center axis of the core section.

Identification of lithologic units

In Holes C0002N and C0002P, we used LWD data (see details in “**Logging**”) in conjunction with analyses of cuttings and core to identify lithologic units and boundaries. We identified compositional and textural attributes of the formation mainly using gamma radiation data, resistivity and sonic logs, and resistivity images along with macroscopic, microscopic, and mineralogical data from cuttings. After evaluating log data quality through the examination of the potential effects of borehole diameter, borehole conditions, and drilling parameters, we defined units using changes in log responses interpreted to reflect differences in rock properties. For this analysis, gamma radiation and resistivity logs were the main input. Integrated interpretation of all the available logs focused on (1) definition and characterization of units and unit boundaries, (2) identification of composition and physical properties within each unit, and (3) interpretation in terms of geological features (unit boundaries, boundaries, transitions, sequences, and lithologic composition).

We interpreted lithologic units within the core, as with cuttings, using a broad suite of data including logs, VCDs, smear slides, thin sections, XRD, XRF, carbonate analysis, and XRCT images.

Structural geology

During Expedition 348, two types of sample material were used for structural geology analyses:

1. Cuttings (>4 mm size fraction) sampled at 5–10 m intervals between 870.5 and 2325.5 mbsf during riser drilling of Hole C0002N and between 1941.5 and 3058.5 mbsf during riser drilling of Hole C0002P.

2. Cores recovered from 475 to 507.64 mbsf in Hole C0002M and from 2163 to 2218.5 mbsf in Hole C0002P.

The methods we used to document the structural geology data of Expedition 348 cores and cuttings are largely based on those used by Expedition 315, 319, and 338 structural geologists (Expedition 315 Scientists, 2009a; Expedition 319 Scientists, 2010b; Strasser et al., 2014a). However, the method for cuttings description was modified to eliminate pillowed cuttings and DICA and to improve statistical counting of structural features. Depths reported for cores and cuttings are reported in CSF-A and MSF depths, respectively.

Description and data collection

Cuttings

Cuttings were investigated at 10 m depth intervals from 870.5 to 2325.5 mbsf in Hole C0002N and from 1941.5 to 3058.5 mbsf in Hole C0002P. Structural descriptions were conducted on sieved, washed, and vacuum-dried (see cuttings workflow in Fig. F1) cuttings collected from 870.5 to 2325.5 mbsf in Hole C0002N and just sieved and washed (wet) cuttings collected from 1941.5 to 3058.5 mbsf in Hole C0002P. Each cuttings bag was thoroughly washed again with seawater for several minutes on the core processing deck to reduce the percentage of DICA and pillowed cuttings. The samples were wet and left to stand for at least 5 min. This allowed the dried DICA and pillowed cuttings to soak up water and disaggregate into mush. Subsequent washing continued until the large majority of the pillowed cuttings were broken down and washed away. Sieving with a 4 and 1 mm mesh then allowed us to extract the >4 and 1–4 mm sized real lithologic cuttings (intact cuttings) for structural analysis. In some samples, 70%–95% of the total initial cuttings disaggregated entirely. The weak lithologies tended to be mostly disaggregated and mixed or destroyed by the drilling process. This potentially induces a bias toward more indurated lithologies (silty sandstone and siltstone). The assumption was that including the drilling-induced disturbances would incorrectly bias the statistical results for the different natural structural elements.

The washed and handpicked formation cuttings were studied with a binocular or digital microscope. For both the 1–4 and >4 mm size fractions, we recorded the total number of intact cuttings investigated and the number of cuttings containing deformation structures, together with the description of each structure, in an Excel spreadsheet.

Deformation structures recognized in the cuttings include bedding, carbonate or pyrite veins (sometimes brecciated), slickenlined surfaces (or slickensides), cataclastic bands, deformation bands (Maltman et al., 1993), web structures (Byrne, 1984), and scaly fabric. Thin sections were made and observed under optical microscope and scanning electron microscope (SEM) to describe representative or particularly interesting structural elements.

Cores

Structures preserved in the cores were documented on split cores and on XRCT images of unsplit cores (see “[X-ray computed tomography](#)”). Observations on split cores were hand logged onto the structural geology observation sheet (Fig. F7) at the core table and then transferred to both a calculation sheet and the J-CORES database (see “[Data processing](#)”). Core observations and measurements followed procedures of previous ODP and IODP expeditions in Nankai and Costa Rica subduction zones (e.g., ODP Legs 131, 170, and 190 and IODP Expeditions 315, 316, 319, 322, 333, 334, 338, and 344). We measured the orientations of all structures observed in cores using a modified plastic protractor (Fig. F8) and then noted the measurements on the structural geology observation sheet along with descriptions and sketches of structures. The orientations of planar or linear features in cores were defined with respect to the core reference frame, for which the core axis is defined as “vertical” and the double line marked on the working half of the core liner is arbitrarily called “north,” 0° or 360° (Fig. F9; in unoriented core, this does not correspond to true north). We followed the techniques developed during Leg 131 (Shipboard Scientific Party, 1991) and later refined during Expeditions 315, 316, 319, 322, 333, and 338 (Expedition 315 Scientists, 2009a; Expedition 316 Scientists, 2009; Expedition 319 Scientists, 2010b; Expedition 322 Scientists, 2010; Expedition 333 Scientists, 2012; Strasser et al., 2014a). To determine the orientations of planes in this core reference frame (Fig. F9), the apparent dip angle of any planar feature was measured in two independent sections parallel to the core axis (Fig. F10). The orientation was then calculated using a calculation sheet (see “[Data processing](#)”). In practice, one section is typically the split surface of the core, on which the trace of the plane has a bearing (α_1) and a plunge angle (β_1) in the core reference frame. α_1 is either 90° or 270°. The other section is, in most cases, a cut or fractured surface at a right or high angle to the split core surface, on which the bearing (α_2) and plunge angle (β_2) of the trace of the plane are measured. In the case

where the second measurement surface is perpendicular to the core split surface, bearing α_2 is either 0° or 180° (Fig. F10). Both β_1 and β_2 are between 0° and 90° . Similar measurements were made for planar features visible in XRCT images.

Linear features (e.g., slickenlines) were commonly observed on planar structures (typically fault or shear zone surfaces). Their orientations were determined in the core reference frame by measuring either their bearing and plunge or their rakes (or pitches) (ϕ_a) on the planes (Fig. F11). We used the following convention in order to avoid confusion between two lines having the same rake but raking toward two opposite azimuths (e.g., a $N45^\circ E-60^\circ SE$ fault bearing two striations, one raking $30^\circ NE$ and the other raking $30^\circ SW$). If the linear feature rakes from an azimuth between $N1^\circ E$ and $179^\circ E$ or between $N181^\circ E$ and $N359^\circ E$, then 90° or 270° , respectively, will follow the value of the rake. In the example depicted in Figure F11, 270° would be added after the ϕ_a value. In the case of subvertical planes, $+1^\circ$ would follow the rake value to indicate rakes from the top of the core and -1° to indicate rakes from the bottom of the core. The calculation sheet takes this information into account for data processing.

All the above-mentioned data as well as any necessary descriptive information were recorded on the structural geology observation sheet. We observed a variety of deformation structures in Expedition 348 cores (see “Structural geology” in the “Site C0002” chapter [Tobin et al., 2015]). These structures include bedding, fault planes, brittle fault zones, deformation bands, calcite-cemented breccia, fissility, and scaly foliation (or scaly fabric). These structures were observed by using the microscope, thin section, and SEM, as necessary.

Data processing

Orientation data calculation and true north correction

A spreadsheet developed during Expeditions 315, 316, 322, 319, 333, 334, 338, and 344 was used to calculate orientation data in the core reference frame (Fig. F12) (Expedition 315 Scientists, 2009a; Expedition 316 Scientists, 2009; Expedition 319 Scientists, 2010b; Expedition 322 Scientists, 2010; Expedition 333 Scientists, 2012; Expedition 334 Scientists, 2012; Strasser et al., 2014a; Harris et al., 2013). Based on the measured bearings (α_1 and α_2) and plunge angles (β_1 and β_2), this spreadsheet determines the strikes and dip angles of the planar features in the core reference frame. Because of drilling-induced core fragmentation (e.g., biscuiting) and ensuing core recovery and core preparation operations, the orientation

of the core with respect to the present-day magnetic north is lost. A correction routine is therefore required to rotate orientations measured in the core reference frame back to the magnetic reference frame. Paleomagnetic data taken by the long-core cryogenic magnetometer on the *Chikyu* (see “Paleomagnetism”) were used to correct drilling-induced rotations of cored sediment whenever there was a paleomagnetic datum point within the same coherent interval. If paleomagnetic data are available, the spreadsheet is further used to convert the core reference data in geographic coordinates. However, reorientation using paleomagnetic measurement was skipped for cores from Holes C0002M and C0002P because of the limited number of the structures and oversized diameter of SD-RCB cores for cryogenic magnetometer onboard.

J-CORES structural database

The J-CORES database has a VCD program to store visual (macroscopic and/or microscopic) descriptions of core structures at a given section index and a record of planar structures in the core coordinate system. The orientations of such features are saved as commentary notes but do not appear on the plots from the Composite Log Viewer. During Expedition 348, only the locations of structural features were entered in J-CORES, and orientation data management and analyses were performed with the spreadsheet as described above. For final publication, structural elements were converted to core-scale depictions using Strater software.

Biostratigraphy and paleomagnetism

Biostratigraphy

During Expedition 348, calcareous nannofossils were systematically studied to assign preliminary ages to cuttings and core samples collected from Holes C0002M, C0002N, and C0002P.

Timescale and biohorizons

Biostratigraphic zones of calcareous nannofossils of sedimentary sequences recovered during Expedition 348 mainly follow the timescale used by biostratigraphic studies carried out during Expeditions 315, 316, and 338 (Expedition 315 Scientists, 2009a; Expedition 316 Scientists, 2009; Strasser et al., 2014a). The review compiled by Raffi et al. (2006) was used to assign ages for the biostratigraphic data. Calcareous nannofossil biostratigraphic zone determination was based on the studies of Martini (1971) and Okada and Bukry (1980) with zonal modification by

Young (1999). Astrochronological age estimates for the Neogene rely on the geologic timescale developed by the International Commission on Stratigraphy (ICS) in 2013 (Cohen et al., 2013). The timescale and biostratigraphic zones of calcareous nannofossils are summarized in Figure F13 and Table T8.

Downhole contamination is a common occurrence in riser drilling cuttings and is a potential problem for recognizing a zonal boundary defined by a first occurrence (FO) datum because such a boundary may appear significantly stratigraphically lower than in situ. In order to avoid this problem, a last occurrence (LO) datum, if available, is designated to approximate the zonal boundary; otherwise the biozone was combined with adjacent zones. An additional criterion was used to resolve the reworking of zonal markers (e.g., a datum was defined by the continuous occurrence of a taxon, whereas sparse occurrence was considered reworked).

Calcareous nannofossils

Taxonomic remarks

Identification of calcareous nannofossils followed the taxonomy compilation of Perch-Nielsen (1985). Species from the genus *Gephyrocapsa* are common Pleistocene biostratigraphic markers. Problems in identification can occur because species of the genus show wide variation in morphological features and size (Su, 1996). Young (1999) suggested size-defined morphological groups of this genus, and this approach was adopted during this shipboard study, including *Gephyrocapsa* spp. medium I (>3.5 to <4 μm), *Gephyrocapsa* spp. medium II (≥ 4.5 to <5.5 μm), and *Gephyrocapsa* spp. large (≥ 5.5 μm). Additionally, *Reticulofenestra pseudoumbilicus* is identified by specimens having a coccolith 7 μm in length in the upper part of its range (the lower Pliocene).

Methods

Standard smear slides were made from cuttings samples at 10 m spacing and core catcher samples within the cored interval with the use of photocuring adhesive as a mounting medium. Calcareous nannofossils were examined using standard light microscope techniques under crossed polarizers and transmitted light at 250 \times to 2500 \times magnification with a Zeiss Axio Imager A1m. Preservation and abundance of nannofossils from the core and cuttings samples investigated were recorded in the J-CORES database. The classification of calcareous nannofossil species preservation was based on the following:

VG = very good (no evidence of dissolution and/or overgrowth).

- G = good (slight dissolution and/or overgrowth; specimens are identifiable to the species level).
- M = moderate (exhibits some etching and/or overgrowth; most specimens are identifiable to the species level).
- P = poor (severely etched or overgrown; most specimens cannot be identified at the species level and/or generic level).

Relative abundances of nannofossil assemblages were based on observations in two traverses at 1250 \times magnification. Samples were further observed for zonal markers and rare species. Group abundance (at 250 \times magnification) and relative abundance of individual calcareous nannofossil species (at 1250 \times magnification) are estimated using the following scale:

- D = dominant (>50% or >50 specimens per field of view [FOV]).
- A = abundant (>15%–50% or >10 to 50 specimens per FOV).
- C = common (>5%–15% or 1 to 10 specimens per FOV).
- F = few/frequent (1%–5% or >1 specimen per 1–10 FOV).
- R = rare (<1% or >1 specimen per 20 FOV).
- T = trace (<0.1% or <1 specimen per 20 FOV).
- B = barren (0; this degree is used only for the group abundance).

Paleomagnetism

Paleomagnetic and rock magnetic investigations on board the *Chikyu* during Expedition 348 were primarily designed to determine the characteristic remanence directions for use in magnetostratigraphic and structural studies. Routine measurements on archive halves were conducted with the superconducting rock magnetometer (SRM).

Laboratory instruments

The paleomagnetism laboratory on board the *Chikyu* houses a large (7.3 m \times 2.8 m \times 1.9 m) magnetically shielded room, with its long axis parallel to the ship transverse. The total magnetic field inside the room is ~1% of Earth's magnetic field. The room is large enough to comfortably handle standard IODP core sections (~150 cm). The shielded room houses the equipment and instruments described in this section.

Superconducting rock magnetometer

The long-core 4 K SRM (2G Enterprises, model 760) uses a Cryomech pulse tube cryocooler to achieve the required 4 K operating temperatures without the

use of liquid helium. The SRM system is ~6 m long with an 8.1 cm diameter access bore. A 1.5 m split core liner can pass through a magnetometer, an alternating field (AF) demagnetizer, and an anhysteretic remanent magnetizer. The system includes three sets of superconducting pickup coils, two for transverse moment measurement (x - and y -axes) and one for axial moment measurement (z -axis). The noise level of the magnetometer is $<10^{-7}$ A/m for a 10 cm^3 volume of rock. The magnetometer includes an automated sample handler system (2G804) consisting of aluminum and fiberglass channels designated to support and guide long core movement. The core itself is positioned in a nonmagnetic fiberglass carriage that is pulled through the channels by a rope attached to a geared high-torque stepper motor. A 2G600 sample degaussing system is coupled to the SRM to allow automatic demagnetization of samples up to 100 mT. The system is controlled by an external computer and enables programming of a complete sequence of measurements and degauss cycles without removing the long core from the holder.

Spinner magnetometer

A spinner model SMD-88 (Natsuhara Giken Co., Ltd.) magnetometer was utilized during Expedition 348 for remanent magnetization measurement. The noise level is $\sim 5 \times 10^{-7}$ mAm², and the measurable range is from 5×10^{-6} to 3×10^{-1} mAm². Two holders are prepared for the measurements, one (small or short) for the weak samples and the other (large or tall) for the strong samples. Five standard samples with different intensities are prepared to calibrate the magnetometer. Standard 2.5 cm diameter \times 2.2 cm long samples taken with a minicore drill or 7 cm³ cubes can be measured in three or six positions with a typical stacking of 10 spins. The whole sequence takes ~1 and 2 min, respectively.

Alternating field demagnetizer

The DEM-95 (Natsuhara Giken Co., Ltd.) AF demagnetizer is set for demagnetization of standard discrete samples of rock or sediment. The unit is equipped with a sample tumbling system to uniformly demagnetize up to a peak AF of 180 mT.

Thermal demagnetizer

The TDS-1 (Natsuhara Giken Co., Ltd.) thermal demagnetizer has a single chamber for thermal demagnetization of dry samples over a temperature range from room temperature to 800°C. The chamber holds up to 8 or 10 cubic or cylindrical samples, depending on the exact size. The oven requires a closed system of cooling water, which is conveniently placed next to the shielded room. A fan next to the

μ -metal cylinder that houses the heating system is used to cool samples to room temperature. The measured magnetic field inside the chamber is <20 nT.

Pulse magnetizer

The MMPM 10 (Magnetic Measurement, Ltd., UK; www.magnetic-measurements.com) pulse magnetizer can produce a high-magnetic field pulse in a sample. The magnetic-field pulse is generated by discharging a bank of capacitors through a coil. A maximum field of 9 T with a pulse duration of 7 ms can be produced by the 1.25 cm diameter coil. The other coil (3.8 cm diameter) generates a maximum field of 2.9 T.

Anisotropy of magnetic susceptibility

A Kappabridge KLY 3S (AGICO, Inc.), designed for anisotropy of magnetic susceptibility (AMS) measurement, is also installed on the *Chikyu*. Data are acquired from spinning measurements around three axes perpendicular to each other. Deviatoric susceptibility tensor can then be computed. An additional measurement for bulk susceptibility completes the sequence. Sensitivity for AMS measurement is 2×10^{-8} SI. Intensity and frequency of field applied are 300 mA/m and 875 Hz, respectively. This system also includes a temperature control unit (CS-3/CS-L) for temperature variation of low-field magnetic susceptibility of samples.

Discrete samples and sampling coordinates

Discrete cubic samples ($\sim 7\text{ cm}^3$) or minicores ($\sim 11\text{ cm}^3$) were taken, two per section, from the working halves in order to determine paleomagnetic direction primarily for magnetostratigraphy. The relation between orientations of archive section and that of discrete samples is shown in Figure F14.

Magnetic reversal stratigraphy

Whenever possible, we offer an interpretation of the magnetic polarity, with the naming convention following that of correlative anomaly numbers prefaced by the letter C (Tauxe et al., 1984). Normal polarity subchrons are referred to by adding suffixes (e.g., n1, n2, etc.) that increase with age. For the younger part of the timescale (Pliocene–Pleistocene), we often use traditional names to refer to the various chrons and subchrons (e.g., Brunhes, Jaramillo, Olduvai, etc.). In general, polarity reversals occurring at core ends have been treated with extreme caution. The ages of the polarity intervals used during Expedition 348 are a composite of four previous magnetic polarity timescales (magnetostratigraphic timescale for the Neogene by Lourens et al., 2004) (Table T9).

Geochemistry

Interstitial water geochemistry for core samples

Sample preparation

When core recovery and quality allowed, 10–41.5 cm long whole-round core (WRC) samples were collected from Hole C0002P cores. Samples were not collected from Core 348-C0002P-1R due to low core recovery. Squeezed IW and ground rock interstitial normative determination (GRIND) pore water (GW) (Wheat et al., 1994) were sampled for the typical suite of shipboard measurements. In addition, IW was sampled from cores collected during testing of the SD-RCB in Hole C0002M for an experiment examination of the effect of high-pressure squeezing of clay minerals on Cl^- concentrations and stable isotopes. Before sampling for IW/GW whole-round sections, the core sections were scanned by XRCT to check for the presence of an intact interval of homogeneous sediment and to avoid structurally or lithologically important features. The section was immediately cut, capped, and then delivered to the geochemistry laboratory for processing. The sample was placed into a nitrogen-filled glove bag and removed from the core liner. Sediment along the outer surface of the WRC was scraped off, as well as along any internal fractures that came in contact with seawater or drilling fluid or had experienced smearing or oxidation. About 5 cm³ of presumably clean sediment from the inside of the core was transferred to a preweighed glass vial and immediately capped. This sample was analyzed by gas chromatograph–electron capture detector (GC-ECD) to assess the drill mud contamination by a perfluorocarbon (PFC) introduced into the drilling mud. Each cleaned WRC was then stored in a N₂-filled bag at room temperature until used for squeezing or GRIND methods.

Squeezing method

The squeezing method was used on all IW samples from Hole C0002M and on the first available IW sample from Hole C0002P (Sample 348-C0002P-2R-3, 96–137.5 cm). Indurated samples were crushed into small fragments inside the glove bag, making them easier to put into the squeezer. The portion of the cleaned WRC to be squeezed was placed in a Manheim-type titanium squeezer (Manheim, 1966).

The squeezers used during Expedition 348 were modified to work under higher squeezing pressures to increase IW extraction from lithified or low-porosity samples. The inner diameter of these squeezers was 55 mm. A newly developed “water-gathering

plate” was used in the lower filtration assembly (Fig. F15). The water gathering plate is 55 mm in diameter, 3 mm thick, and includes 32 holes (1 mm diameter each) and 8 grooves to funnel extracted water to a central 3.6 mm diameter hole for flow down and out toward a syringe. Initial experiments conducted before drilling revealed that some mud was passing around the edges of the filter assembly and into the exit port. The final filtration assembly that successfully solved this problem was, from bottom to top, a bottom dish squeezer plate, a rubber disk, a titanium dish, a disk of filter paper, the water-gathering plate, a titanium mesh disk, a second filter paper disk, the sediment sample, and a third filter paper disk (Fig. F15A). The outer portions of the water-gathering plate and the titanium mesh disk were covered with Teflon tape to improve the seal with the squeezer jacket. This assembly was used in the squeezing method for Cores 348-C0002M-1R through 4R.

To allow more extraction of pore water from low-porosity sediment during the squeezing of Section 348-C0002P-2R-3, a squeezer with a top and bottom syringe port was used (Fig. F15B); this assembly was composed of the same filtration set as for squeezing samples from Hole C0002M, on both the top and bottom of the squeezer assembly.

Both assemblies were successfully tested to an applied load of 60,000 lb for >12 h during experiments with Hole C0002M samples. Following the procedures of the Expedition 319 Scientists (2010b), the samples were presqueezed using a manually operated squeezer until a few drops of water came out. This allowed a maximum amount of IW to be collected. Then, a 25 mL acid-washed (12 M HCl) syringe was installed into the IW sample port(s) of the squeezer, and the samples were subjected to automatic squeezing.

The squeezing sequences (Table T10) comprised 6 steps for Hole C0002M and 4 steps for Hole C0002P samples. The following applied loads, with calculated internal pressures and duration of squeezing time in parentheses, were used for IW extraction from Sections 348-C0002M-1R-2 and 2R-2 on hydraulic press Number 2 (calibration of the device was made on 24 December 2013). IW was collected after preprogrammed hydraulic press recipes 1–3 (aliquot A), preprogrammed hydraulic press recipes 4–6 (aliquot B), and four larger applied forces from 30,000 to 60,000 lb (aliquot C and C'/C'') using the following parameters:

- Recipes 1–3: 15,000 lb (5 min), 17,000 lb (7 min), and 20,000 lb (10 min).
- Recipes 4–6: 21,500 lb (10 min), 23,000 lb (10 min), and 25,000 lb (10 min).

- Applied forces 30,000 lb (10 min), 40,000 lb (10 min), 50,000 lb (10 min), and 60,000 lb (720 min).

An intermediate aliquot (C') of IW was collected after 50,000 lb from Sections 3R-1 and 4R-1.

For Section 348-C0002P-2R-3, the following sequence was applied: 5,300 lb (10.9 MPa; 5 min), 10,700 lb (20.0 MPa; 10 min), 16,000 lb (30.0 MPa; 30 min), and 21,300 lb (39.9 MPa; 720 min). The maximum squeezing pressure value was chosen to avoid expulsion of interlayer water from hydrous clay minerals, according to the tests conducted on Hole C0002M core samples. Extracted water was kept at 4°C prior to analysis.

GRIND method

Squeezing applied on the first available sample from Hole C0002P (Sample 348-C0002P-2R-3, 96–137.5 cm) did not yield IW. Therefore, the GRIND method was used on all core samples from Hole C0002P, including samples from Section 348-C0002P-2R-3. The sample from Section 6R-2 was divided in two aliquots, and both were prepared identically to assess the reproducibility of the method. However, Section 6R-2 was squeezed longer to extract more water. Scraped samples were crushed to 1 cm pieces. For each GW analysis, <30 g of solid sediment was used. Fragments <1 cm in diameter of the IW core were weighed in a glass dish and dried for 24 h at 60°C in a ventilated oven to measure pore water content. A second aliquot of 80 g of the IW core was weighed in a glass beaker and transferred to an agate mill bowl with 5 agate balls. Milli-Q water (10 mL [2 × 5 mL]), purged for 24 h with nitrogen gas, was pipetted into the sediment aliquot. The sediment was crushed at 400 rpm for 5 min (Section 6R-2) or 10 min (Sections 2R-3, 3R-2, 4R-2, and 5R-2) until all hard chunks were converted to paste. The paste was then transferred into the squeezing jacket. Some drying of the paste occurred during this transfer step.

The filtration assembly for squeezing the GW samples was the same as described above. The paste was carefully transferred from the milling bowl into the squeezer jacket, and the sediment was squeezed at 5,300 lb (10.9 MPa) to 10,700 lb (20 MPa) for at least 1 h each. An additional step at 30 MPa was used on both subsamples of Section 6R-2 to recover more GRIND water.

For both the squeezing method and the GRIND method, the squeezed water was filtered with a 0.45 µm disposable filter and stored in glass or high-density polyethylene (HDPE) sample vials, previously prepared by immersion in 55°C 10% trace metal-grade 12 M HCl for at least 24 h, rinsed with Milli-Q

water, and dried in a Class 100 laminar flow clean hood. An aliquot of IW/GW was stored in a 4 mL HDPE bottle for analysis of pH, alkalinity (when water volume allowed), major anions (sulfate and bromide), and nutrients (phosphate and ammonium ions). Another aliquot of IW was stored in a 4 mL HDPE bottle acidified with 0.4 vol% 6 M HCl for analysis of major (Na, K, Ca, and Mg), minor (Ba, Si, B, Li, Mn, and Sr), and trace (V, Cu, Zn, As, Rb, Mo, Cs, Pb, and U) elements.

Assessing drilling mud contamination

Along with PFC assessment in IW/GW samples, mud water and liner-core liquid (LCL) were also analyzed to determine if IW sample contamination occurred.

Mud water

During drilling in Hole C0002N, 10 samples of drilling mud were collected from the active mud circulation pit. Mud was also collected during drilling and coring of Hole C0002P. Mud water (LMW) extracted from the drilling mud was analyzed for carbonates, pH, alkalinity, salinity, chlorinity, major anions and cations, and minor and trace (Hole C0002P only) elements. Mud samples were collected simultaneously with cuttings, and the lag time from drill bit to the surface was evaluated with a CaC₂ tracer (Strasser et al., 2014a).

Because of high viscosity, mud-water samples were diluted 10 times. A 1 mm aliquot of mud-water sample was pipetted in a Falcon tube with 9 mL of ultra-pure water and then sonicated for 1 h in an ultrasonic bath. After centrifugation at 9500 rpm (4°C) for 1 h, the supernatant was filtered at 0.45 µm and analyzed. Water content in the drilling mud was determined by drying in a vacuum oven for 48–65 h. Results are listed in Table T17 in the “Site C0002” chapter (Tobin et al., 2015).

Liner-core liquid

As soon as the cores from Hole C0002P were recovered and brought on the core deck, the LCL was collected in a 45 mL centrifuge tube. From this tube, 2.5 mL was transferred into a 20 mL preweighed glass vial and heated at 80°C for 30 min. Then, 300 µL of the liberated gas was extracted through the vial septum with a microsyringe and injected into the GC-ECD for analysis of PFC. Results are listed in Table T22 in the “Site C0002” chapter (Tobin et al., 2015).

Interstitial water analyses

The standard IODP procedure for IW analysis was modified according to the availability and function-

ality of onboard instruments (Expedition 319 Scientists, 2010b). However, because of the limited amount of extracted pore water, not all of the standard IODP measurements were conducted. When IW/GW volumes were too low, standard pH and alkalinity measurements were not made because they consume 3 mL of IW. In this case, only pH was measured using the LAQUAtwin B-712 compact pH meter, with reported accuracy of 0.1 pH.

Concentrations of numerous major and minor components in the IW/GW were analyzed. Chlorinity was measured on a 100 μL aliquot by potentiometric titration using a Metrohm autotitrator and silver nitrate (AgNO_3) as a titrant in 30 mL of 0.2 M sodium nitrate (NaNO_3) solution. Relative standard deviation (RSD) for chlorinity was better than $\pm 0.2\%$, based on repeated analyses of International Association for the Physical Sciences of the Oceans (IAPSO) standard seawater, which were conducted after every five IW samples. Bromide and sulfate concentrations were measured with a Dionex ICS-1500 ion chromatograph with an anion column. An aliquot was diluted to 1:100 (10 μL in 990 μL) with Milli-Q water. IAPSO standard seawater aliquots (2.5, 5, 7.5, and 10 μL in a total of 1000 μL) were analyzed at the beginning and end of each run for quality control and to monitor potential drift in sensitivity throughout a particular run. RSDs are $\pm 3\%$ for bromide and $\pm 1\%$ for sulfate. An ion chromatograph was used to determine the concentrations of major cations such as Na^+ , K^+ , Mg^{2+} , and Ca^{2+} . Aliquots of IW/GW samples acidified with 6 M HCl (Tamapure-AA-100 grade) were used for this measurement. These samples were diluted to 1:200. The diluted samples were placed in an autosampler together with five calibration solutions and two blank solutions (Milli-Q water). For quality control, a 1:200 solution of diluted IAPSO standard seawater was measured after every eight IW samples.

To determine the concentration of each element, standard solutions were analyzed to construct calibration curves from the measured peak area and the known concentration. For the calibration, an IAPSO standard seawater solution containing Na^+ (480 mM), K^+ (10.4 mM), Mg^{2+} (54 mM), and Ca^{2+} (10.6 mM) was diluted to four standard solutions (25%, 50%, 75%, and 100%). The resulting RSD for the measurements was less than $\pm 0.5\%$ for Na^+ , $\pm 1\%$ for K^+ , $\pm 0.7\%$ for Mg^{2+} , and $\pm 0.5\%$ for Ca^{2+} .

For PO_4^{3-} and NH_4^+ , colorimetric methods were applied. Both dissolved solids must be analyzed within 24 h because they are quickly degraded by biological activity. Ammonium adsorption of indophenol blue at 640 nm wavelength was measured with a spectro-

photometer (Shimadzu UV-2550PC), with an aliquot of 100 μL of sample IW used as the minimum volume. Standard, blank, 2, 4, 6, 8, and 10 mM NH_4^+ solutions were prepared in the same manner as the sample solutions and analyzed within 5 h. Phosphate (an aliquot of 100 μL IW) was analyzed using adsorption of molybdate blue at 885 nm wavelength with the spectrophotometer used for NH_4^+ . Standard, blank, 0.5, 1, 2.5, 5, and 7.5 mg/L solutions were prepared in the same manner as that of sample solutions. RSDs of repeated analyses of both components are $< 1\%$.

Minor element (B, Ba, Fe, Li, Mn, Si, and Sr) concentrations were determined on 500 μL aliquots using an inductively coupled plasma-atomic emission spectrometer (ICP-AES) (Horiba Jobin Yvon Ultima2). Aliquots of IW/GW acidified with 6 M HCl (Tamapure-AA-100 grade) were diluted to 1:20 with 0.15 M HNO_3 . Ultrapure primary standards (SPC Science PlasmaCAL) were prepared with a matrix solution of sulfate-free artificial seawater to fit the sample matrix, and 10 ppm Y solution was added as an internal standard. A matrix solution that approximated IAPSO standard seawater major element concentrations was prepared by mixing the following salts in 1 L of Milli-Q water acidified with 4 μL of Tamapure-AA-100-grade 6 M HCl: 26.9 g NaCl, 3.81 g MgCl_2 , 1.0 g CaCO_3 , and 0.75 g KCl. A stock standard solution was prepared from ultrapure primary standards (SPC Science PlasmaCAL) in the 1% HNO_3 solution and then diluted in the same 1% ultrapure HNO_3 solution used for IW samples to concentrations of 100%, 50%, 25%, 10%, 5%, and 1%. A 10 ppm Y solution diluted as 1% HNO_3 solution was prepared as a blank. A series of standards were made by adding 1.25 mL of each stock solution to 8.75 mL of matrix solution. The matrix-matched 100% standard solution contained the following concentrations of elements:

B	= 145 μM .
Ba	= 11.4 μM .
Fe	= 2.80 μM .
Li	= 22.5 μM .
Mn	= 2.84 μM .
Si	= 55.7 μM .
Sr	= 17.8 μM .

Because values of many of these elements in IAPSO standard seawater are either below detection limits (e.g., Fe and Mn) or variable, a standard prepared in the 10% matrix-matching solution was repeatedly analyzed to calculate the precision of the method. RSDs determined by repeated analyses of the 10% matrix-matching solution were $\pm 2.5\%$ for B, $\pm 1.5\%$ for Ba, $\pm 3.5\%$ for Fe, $\pm 4.1\%$ for Li, $\pm 2.5\%$ for Mn,

$\pm 2.5\%$ for Si, and $\pm 2.0\%$ for Sr; As, V, Cu, Zn, Rb, Mo, Cs, Pb, and U were quantified on 500 μL IW samples using ICP–mass spectrometry (ICP-MS) (Agilent 7500ce) equipped with an octopole reaction system to reduce isobaric interferences from polyatomic and double-charged ions. We used the remainder of the same aliquot after determining major and minor elements using an ion chromatograph and ICP-AES.

To correct for interferences among some of the transition metals (V, Cu, and Zn) and some major element oxides, solutions containing the metals with concentrations similar to IAPSO standard seawater values were prepared. These solutions were then analyzed at the beginning of each measurement, and an interference correction was applied based on the average ion counts per second measured on the standard solutions divided by the abundance of the interfering elements. A 500 μL aliquot of sample IW/GW was diluted with 500 μL of 500 ppb In internal standard solution and 4 mL of 1% HNO_3 based on the previous determination of detection limits and low concentrations of the elements of interest.

A primary standard solution was made to draw the calibration lines matching the maximum range of predicted concentrations based on published results of deep-sea pore fluid compositions in a variety of settings. The concentrations of the standard are as follows:

- As = 40 ppb.
- V = 40 ppb.
- Cu, Mo, Pb, and U = 40 ppb.
- Zn = 140 ppb.
- Rb = 540 ppb.
- Cs = 40 ppb.

This primary standard was diluted with 1% HNO_3 solution to relative concentrations of 100%, 50%, 25%, 10%, 5%, 1%, and blank. A 500 μL split of these standards was then further diluted by addition of the In solution, 3.5 mL of 1% HNO_3 solution, and 500 μL of a 560 mM NaCl solution to account for matrix suppression of the plasma ionization efficiency.

The 200% and 400% standard solutions were also prepared using 100% solution changing dilution rate (i.e. instead of combination of 500 μL 100% standard, 500 μL In, and 4 mL HNO_3 solutions, 1000 and 2000 μL of 100% standard solution were diluted with 500 μL In solution and 3.5 and 3.0 mL HNO_3 solutions, respectively). The 25% standard was diluted accordingly and analyzed together with eight samples throughout every analysis series for precision and to check the drift during measurements. Blanks were also analyzed every eight samples, and detection limits were determined to be three times

the standard deviation of a procedural blank of Milli-Q water acidified with 4 mL of Tamapure-AA-100 grade 0.15 M HNO_3 . The average precision of multiple determinations of the 25% ICP-AES standard was

- $\pm 4.7\%$ for ^{75}As ,
- $\pm 3.6\%$ for ^{51}V ,
- $\pm 1.7\%$ for ^{65}Cu ,
- $\pm 4.5\%$ for ^{65}Zn ,
- $\pm 1.6\%$ for ^{85}Rb ,
- $\pm 4.5\%$ for ^{95}Mo ,
- $\pm 0.6\%$ for ^{133}Cs ,
- $\pm 1.96\%$ for ^{208}Pb , and
- $\pm 2.0\%$ for ^{238}U .

Organic geochemistry

Gas analysis in core samples

Headspace analysis

For headspace analysis, $\sim 5\text{ cm}^3$ or half the volume of a 20 mL glass vial of sediment was taken from the core using a cork borer; in the case of highly consolidated sediment, pieces of sediment were crushed with a chisel or in a tungsten mortar. The sample was placed in a glass vial (20 cm^3) that was immediately sealed with a silicon septum and crimped metal cap. The exact mass of the wet sample was determined after gas analysis was finished.

For C_1 – C_4 hydrocarbon gas analysis, the vial was placed in a headspace sampler (Agilent Technologies G1888 network headspace sampler), where it was heated at 70°C for 30 min before an aliquot of the headspace gas was automatically injected into an Agilent 6890N GC equipped with a packed column (GL HayeSep R) and flame ionization detector (FID). The carrier gas was He. In the GC temperature program, the initial temperature of 100°C was held for 5.5 min before the temperature was ramped up at a rate of $50^\circ\text{C}/\text{min}$ to 140°C and maintained for 4 min. Chromatographic response of the GC was calibrated against five different authentic standards with variable quantities of low-molecular weight hydrocarbons and checked on a daily basis. Methane concentration in interstitial water was derived from the headspace concentration using the following mass balance approach (Underwood et al., 2009):

$$\text{CH}_4 = [\chi\text{M} \times P_{\text{atm}} \times \text{VH}] / [\text{R} \times T \times V_{\text{pw}}],$$

where

VH = volume of headspace in the sample vial,

V_{pw} = volume of pore water in the sediment sample,

χM = mole fraction of methane in the headspace gas (obtained from GC analysis),

P_{atm} = pressure in the vial headspace (assumed to be the measured atmospheric pressure when the vials were sealed),

R = universal gas constant, and

T = temperature of the vial headspace in Kelvin.

The volume of interstitial water in the sediment sample was determined based on the bulk mass of the wet sample (M_b), the sediment's porosity (ϕ , which was extrapolated from shipboard moisture and density (MAD) measurements in adjacent samples), grain density (ρ_s), and the density of pore water (ρ_{pw}) as

$$V_{\text{pw}} = M_{\text{pw}}/\rho_{\text{pw}} = [\phi \times \rho_{\text{pw}}]/[(1 - \phi) \rho_s] \times M_b/\rho_{\text{pw}}$$

where

M_{pw} = pore water mass,

$\rho_{\text{pw}} = 1.000\text{--}1.024 \text{ g/cm}^3$ (adjusted to salinity based on shipboard data), and

$\rho_s = 2.8 \text{ g/cm}^3$.

CHNS analysis

Total carbon (TC) and total nitrogen (TN) were analyzed using samples from cuttings and core samples, and total sulfur (TS) was measured using Hole C0002P core samples. Cuttings (10 cm³) were washed with seawater, sieved, freeze-dried under a vacuum, and ground to powder before analysis. Core samples (~60 mg) were freeze-dried under a vacuum and ground to powder. TC, TN, and TS concentrations were determined using a Thermo Finnigan Flash elemental analysis (EA) 1112 CHNS analyzer. Calibration was based on the synthetic standard sulfanilamide, which contains 41.81 wt% C, 16.27 wt% N, and 18.62 wt% S. About 15–25 mg of sediment powder was weighed and placed in a tin container for carbon and nitrogen analyses. The same amount of powdered sediment was weighed for sulfur analysis. This was mixed with an oxidizer (vanadium pentoxide V₂O₅) in a Ti container and then combusted in an oxygen stream at 900°C and 1000°C for carbon and nitrogen and for sulfur, respectively. The sample and container melt, and the tin promotes a violent reaction (flash combustion) in a temporarily enriched oxygen stream. The combustion produces CO₂, SO₂, and NO₂, which are carried by a constant flow of carrier gas. Then, NO₂ is reduced to N₂, and the mixture of N₂, CO₂, and SO₂ is separated using a GC equipped with a thermal conductivity detector (TCD). The accuracy of the analysis is confirmed using soil NCS reference material (Thermo Scientific, Milan, Italy), sulfanilamide standard (Thermo Scientific), and JMS-1 reference material.

Total organic carbon (TOC) is usually estimated by difference between the TC value and inorganic carbon (IC) value. The IC is determined with the same set of samples used for elemental analysis. Approximately 15–25 mg of sediment powder is weighed and acidified with 2 M HCl to convert the carbonate to CO₂. The released CO₂ is titrated, and the change in light transmittance is measured with a photodetection cell. The weight percentage of calcium carbonate is calculated from the IC content, assuming that all evolved CO₂ is derived from dissolution of calcium carbonate:

$$\text{CaCO}_3 \text{ (wt\%)} = \text{IC (wt\%)} \times 100/12.$$

No correction was made for the presence of other carbonate minerals. Standard deviation for the samples was less than ±0.05 wt%. NIST-SRM 88b and JSD-2 (standard reference materials) were used to check accuracy. TOC contents were calculated by subtracting IC from TC contents as determined by elemental analysis.

Gas analysis

Onboard mud-gas monitoring system

Continuous mud-gas monitoring (CMGM) is a standard method for the qualitative estimation of in situ gas concentrations in real time. In the framework of IODP, CMGM was carried out during Expedition 319 (Expedition 319 Scientists, 2010a, 2010b) using third-party tools, as well as during Expeditions 337 and 338 with onboard instruments (Expedition 337 Scientists, 2013; Strasser et al., 2014a).

In general, formation gas is liberated when the drill bit crushes the sediment or rock and is circulated upward with the drilling mud. Once onboard, gas-enriched drilling mud flows along the flow line to a degasser, where an impeller stirs the mud and a vacuum is applied to separate gases from the drilling mud. During Expedition 348, two different degassers were used and installed at two different locations along the flow line (Fig. F16). For the depth interval from 838 to 2330 mbsf, the degasser and configuration were similar to previous expeditions (e.g., Strasser et al., 2014a; see also position D1 in Fig. F16). The drilling mud passes the flow splitter, and some of the mud is bypassed to the degasser. Gas liberated from the drilling mud then migrates through polyvinyl chloride (PVC) tubing to the mud-gas monitoring laboratory (MGML). On its way to the MGML, the gas has to pass a safety valve, which protects the system against mud entering the PVC tubing in case of mud overflow. Because of continuous air contamination, a new degassing unit was installed, which was positioned in the mud trough

next to the degasser from GeoServices (position D2 in Fig. F16A). The height of the new degasser can be manually adjusted to ensure that the impeller can stir the drilling mud. The new degasser was used for drilling and coring Hole C0002P in the 1954–3058 mbsf depth interval. During Expedition 348, a jack was attached to the degasser to speed up lifting and lowering of the instrument. The liberated gas is forwarded to the MGML through PVC tubing without passing a safety valve. Inside the MGML, it was necessary to monitor the pressure of the vacuum applied to the degasser. If the pressure was less than -60 hPa (as low as approximately -73 hPa during this expedition), drilling mud forced the mud trap to close; thus the extracted gas could not enter the PVC tubing. In this case, the mud trap had to be cleaned, which took at least 10 min and caused a data gap in the Rn, methane carbon isotope analyzer (MCIA), process gas mass spectrometer (PGMS), and gas chromatograph–natural gas analyzer (GC-NGA) data. To identify drops in mud level, MCIA data were regularly compared to data from GeoServices. If the two data sets started to significantly deviate (several 100 ppm), the degasser had to be adjusted to the new mud level.

For the first configuration, the traveltime from the degasser to the MGML was estimated to be 6 min (Expedition 337 Scientists, 2013; Strasser et al., 2014a), whereas for the new system, the traveltime was reduced to 2 min. For both, diffusion loss during transportation through PVC tubing is negligible (Wiersberg and Erzinger, 2007). Upon arrival in the MGML, the gas had to pass a dehydration module, after which the dry and clean gas was distributed online to measurement instruments. Sampling was possible along a third-party sampling line and an IsoTube port located upstream of the dehydrator and through an IsoTube port located downstream of the dehydrator.

Online analysis of (non)hydrocarbon gases by gas chromatography

The first instrument along the main gas flow line in the MGML is a GC-NGA (Agilent Wasson ECE 6890N), with a gas sampling port with a multiposition valve. Theoretically, the GC-NGA allows the analysis of hydrocarbon gases (methane, ethane, propane, *i*-/*n*-butane, and pentane [i.e., C₁–C₅]), Ar, He, O₂, N₂, Xe, CO, and CO₂. Similar to Expedition 338 (Strasser et al., 2014a), nitrogen had to be used as the carrier gas because helium was one of the target components. H₂ was not used because of baseline problems. Gas analysis starts at a 50 cm capillary column that is able to retain hexane and heavier hydrocarbon components, followed by the separation of

lighter hydrocarbon gases in another 49 cm capillary column that connects to a FID. Methane was extracted from the rest of the components by an 8 inch micropack column (Wasson ECE Instrumentation, column Code 2378), whereas CO₂ was separated by a 1.27 cm capillary column (Wasson ECE Instrumentation, column Code S036). Both columns are connected to a TCD that has a detection limit of 400 ppm for CO and 200 ppm for the remaining permanent gases. The detection limit for higher hydrocarbons is <1 ppm.

Although the GC-NGA has good sensitivity, the temporal and spatial resolution of the mud-gas analysis with a GC-NGA is limited because of the long measurement time (FID = 15 min; TCD = 20 min). During Expedition 348, the TCD was only used to detect He, H₂, and Xe, and FID measurements were carried out every 12 h to determine the hydrocarbon compositions. The continuous gas flow rate was set at 50 mL/min.

The GC-NGA was calibrated once in the beginning of the expedition by using two standards. The standard mixture for calibration of permanent gases contained 1% of Ar, CO, Xe, O₂, H₂, CO₂, and He in a balance of N₂. The hydrocarbon standard mixture contained 1% C₁–C₅ in a balance of N₂. Afterward, the same standard gases were used to conduct a condition check every 24 h.

Online analysis of the stable carbon isotopic composition of methane

Methane concentrations and methane carbon isotope ratios were determined at a sampling frequency of 1 Hz using an MCIA (Los Gatos Research, Model 909-0008-0000) on the basis of cavity ring-down spectroscopy technology. The stable carbon isotopic composition of methane is reported in the $\delta^{13}\text{C}_{\text{CH}_4}$ notation relative to the Vienna Pee Dee belemnite (VPDB) standard and expressed in parts per thousand (per mil) as

$$\delta^{13}\text{C}_{\text{CH}_4} = [(R_{\text{sample}} - R_{\text{VPDB}})/R_{\text{VPDB}}] \times 1000,$$

where

$$R_{\text{sample}} = {}^{13}\text{C}_{\text{CH}_4}/{}^{12}\text{C}_{\text{CH}_4}$$

and

$$R_{\text{VPDB}} = 0.0112372 \pm 2.9 \times 10^{-6}.$$

Accuracy is $<4\%$ for gas concentrations between 200 and 400 ppm but improves to 1% for concentrations above 400 ppm. The MCIA comprises a gas dilution system that works with hydrocarbon or “zero

air" (i.e., hydrocarbon free standard gas consisting of O₂, N₂, and Ar) and allows measurement of methane concentrations in the 500–10⁶ ppm range (i.e., 100%). Unfortunately, a technical problem with the dilution system precluded the determination of absolute methane concentrations between 1 × 10⁴ and 2 × 10⁵ ppm. Carbon isotope ratios were not affected by this defect. Calibration was carried out once on 26 October 2013, whereas sensitivity was checked daily by manual injection of a gas standard. For both calibration and sensitivity checks, the standard gas (Biso-1) contained 2500 ppm CH₄ and had a δ¹³C_{CH₄} value of −54.5‰ ± 0.2‰. Monitoring took place at a continuous gas flow rate of 20–40 mL/min.

Online gas analysis by process gas mass spectrometer

Continuous monitoring of He, O₂, Ar, Xe, N₂, CO, CO₂, methane, ethane, propane, and butane (differentiation between *n*- and *i*-butane was not possible) was conducted by an AMETEK PGMS. The PGMS does not require a carrier gas, thus contamination of the drilling mud gas is unlikely. The instrument includes a quadrupole mass filter by which gases are identified based on the individual molecular masses of the desired compounds. The optimal scanning range of the mass-to-charge ratio (*m/z*) of the Faraday cup detector is 1–100 but can be extended to an *m/z* of 1–200 with a mass resolution of 0.5 at 10% peak height. Input gas flow rate was set to 50 mL/min. During Expedition 348, no full-range measurements (*m/z* = 1–200) were conducted. Instead, the system operated in "trend mode," in which a predefined set of masses was determined. Similar to Expedition 338 (Strasser et al., 2014a), the reduction of the dwell time to 120 ms allowed a sampling interval of 5 s.

For quality assurance, three different calibrations had to be carried out every 24 h:

1. Binary calibration establishes peak ratios of ion fragments by using a mixture of two gases. The binary calibration should be adjusted to the expected gas composition (e.g., by a combination of a noninterfering balance gas like Ar and a standard gas of similar concentration to the main component in the sample stream). In contrast, for our measurements only CH₄ with a concentration of 100% was used. Masses of 12, 14, and 15 were used for the determination of methane.
2. Blend calibration is necessary to diminish the effect of ionization variations. The calibration was carried out with three different gases:
 - a. Standard gas containing 1% Ar, CO, Xe, O₂, CO₂, and He in a balance of N₂;

- b. A standard gas consisting of 1% C₁–C₅ in a balance of N₂; and
- c. Zero air (i.e., O₂, N₂, and Ar). No standard gas suitable for the expected gas concentrations was available.

3. Background calibration is necessary to determine the concentration of atmospheric gases in the vacuum chamber. For this purpose, Ar and N₂ calibration gases were used, each having a concentration of 100%.

During drilling operations, the PGMS ion current became unstable. Consequently, the 1144–1163.5, 1371–1546, 1747.5–1856, and 2036.9 mbsf depth intervals were not used during the data evaluation. In general, the fraction of atmospheric components in the drilling mud gas is assessed using Ar, N₂, and O₂ concentrations. Sources of air contamination are many, including the configuration of the degasser, leaks in the main gas flow line between degasser and MGML, malfunction of the instruments and sampling systems in the MGML, and drilling operations (pipe connection, core recovery, etc.; see also Strasser et al., 2014a). Also, CO₂ concentrations were altered because of the high pH of the drilling mud (Expedition 319 Scientists, 2010b; Strasser et al., 2014a).

Online radon analysis

Radon analysis was performed with a stand-alone radon monitor (Alpha GUARD PQ2000 PRO) provided by the Japan Agency for Marine-Earth Science and Technology (JAMSTEC) Institute for Research on Earth Evolution (IFREE). The apparatus was attached to the auxiliary port of the scientific gas monitoring line parallel to other instruments. The radon monitor measures the Rn decay within an ion-counting chamber with a volume of 650 mL (effective volume = ~500 mL). Measurements were carried out every 10 min with 5 counts/min and a sensitivity of 100 Bq/m³ in the concentration range of 2 to 2 × 10⁶ Bq/m³. Internal temperature, pressure, and relative humidity were monitored as well and synchronized with Rn data. The data were not automatically included in the SSX database system but are available in the MGML.

Sampling for shore-based analysis

Samples were collected in IsoTube samplers (Isotech Laboratories, Inc.), copper tubes, and glass flasks. From 838 to 2000 mbsf, only IsoTubes were used for sampling, with a sampling interval of 100 m. Below this depth, the sampling interval was increased to 200 m. Sampling with glass flasks started between 2050 and 3058.5 mbsf with a sampling interval of 150 m. Copper tube samples were taken every 100 m between 2200 and 3050 mbsf. Additional event gas

sampling took place when gas peaks significantly above the background concentrations occurred, usually as a consequence of pipe tripping or pipe connection.

The configuration of the third-party sampling line is similar to that during Expedition 338 (Strasser et al., 2014a). Glass flasks and copper tubes were connected to a sampling port at the main gas flow line with PVC tubing. Drilling mud gas can flow from an auxiliary sampling port through the glass flasks, pass the copper tubes, and migrate back to another sampling port at the main gas flow line (Fig. F16).

After sampling, the valves at both ends of the glass flasks were closed and clamps were placed at both ends of the copper tubes. Afterward, both the glass flask and the copper tube were exchanged with empty vials.

Recording online gas analysis and monitoring drilling operations, time, and depth

Gas concentrations determined from mud gas monitoring are easily affected by drilling operations. Therefore, both the drilling parameters and the results from GC-NGA, PGMS, and MCIA measurements were stored in real time in the SSX database, together with gas data and the lag depth determined by technicians from GeoServices (Schlumberger). The SSX system provides a graphic user interface that allows real-time monitoring of the various parameters and helps detect sudden changes in gas concentration. For the PGMS data, real-time monitoring was only possible for two predefined components (O_2 and N_2). The real-time information is stored and can be accessed in the MGML and on the shipboard server. Ship time (UTC + 9 h) was used to synchronize the different parameters. The stand-alone Rn monitor used an internal clock set to UTC + 9 h because its data are not included in the SSX system.

Lag depth is based on the lag time, which includes the time the drilling mud needs to travel from the drill bit back to the ship and the time the gas needs to flow from the degasser to the MGML. Here lag depth, L (as recorded in real time in the SSX database and provided by GeoServices), was used and is calculated based on the lag time, rate of penetration, pump rate, and borehole volume. The lag depth is recorded in meters BRT. Conversion to the mbsf depth scale was done by subtracting water depth (1939 m) and the distance between mean sea level and the rotary table (28.5 m).

Data recording was continuous, even if the mud pumps were turned off because of operational issues and/or gas flow was absent. As a consequence, time periods where lag depth did not change or where gas

concentrations were below the detection limit were not included in the data evaluation.

Background control

Before the drilling mud is sent down the drill pipe, it already has a background concentration of atmospheric gases and gases that are not fully removed during gas extraction and mud recycling. In order to assess the background concentrations, drilling mud was sampled from the tank regularly and subject to headspace gas analysis. No sampling was conducted in Hole C0002N. During drilling and coring of Hole C0002P, drilling mud was sampled by the Telnite mud engineers with 50 mL plastic vials, which were completely filled and sealed with a plastic cap. In the laboratory, a fraction of the mud sample was transferred into a 20 mL glass vial, sealed with silicon septum and a metal crimped cap, and analyzed with an Agilent Technologies G1888 network headspace sampler. The sample was heated at 70°C for 30 min before an aliquot of the headspace gas was automatically injected into the GC-FID. Background concentrations of nonhydrocarbon gases could not be determined with the available instrumentation. The results of the background checks are shown in Figure F17 and Table T11. The background gas consisted almost solely of methane with concentrations up to 45.8 ppmv. Ethane and propane were only present in traces, with up to 2.2 and 0.6 ppmv, respectively. It became clear that hydrocarbons are about two orders of magnitude higher than the background concentrations when compared to the hydrocarbon gas concentrations found in the drilling mud gas, (see “Geochemistry” in the “Site C0002” chapter [Tobin et al., 2015]). Consequently, the influence of background gas concentrations in the drilling mud on the real-time measurements is believed to be small.

Physical properties

Physical property measurements provide valuable constraints on bulk physical character to augment lithologic unit characterization and to facilitate correlation of seismic reflection data with discrete core and cuttings measurements and descriptions. Thus, these data provide information necessary for reliable cuttings-core-log-seismic integration. Expedition 348 employed multiple approaches and methods to characterize the physical properties of cuttings and cores.

Prior to core physical property measurements, XRCT images were collected for all cores, and cores were equilibrated to room temperature (~20°C). After temperature equilibration, whole-round core sections were processed in the MSCL-W to measure gamma ray attenuation (GRA) density, magnetic susceptibil-

ity, natural gamma radiation (NGR), *P*-wave (compressional) velocity, and electrical resistivity. After cores were split into archive and working halves, MAD, electrical resistivity, and *P*-wave velocity measurements were performed on discrete samples of cores from the working halves. Thermal conductivity measurements were made on working halves using the TeKa thermal conductivity meter in the half-space mode (HLQ). High-resolution digital image photography and color reflectance measurements were performed on archive halves using the MSCL-I and MSCL-C.

For cuttings recovered in Holes C0002N and C0002P (870.5–2330.5 and 1955.5–3058.5 mbsf), limited measurements were conducted due to the low amount of the available material. Unwashed cuttings were analyzed for NGR employing the MSCL-W to determine variations in the radioactive counts of the samples and for correlation with LWD gamma ray measurements. Cuttings were rinsed with seawater to remove contamination from drilling mud and then sieved into 0.25–1, 1–4, and >4 mm size fractions. Washed cuttings samples (~40 cm³ each) were taken from the 1–4 and >4 mm fractions for physical property measurements, including MAD, magnetic susceptibility, dielectric permittivity, and electrical conductivity. Handpicked cuttings were also used for MAD measurements to avoid sampling the DICAs and pillow cuttings (see “[Introduction and operations](#)”). In addition, electrical resistivity and *P*-wave velocity measurements were performed on large handpicked cuttings.

MSCL-W

Whole-round cores were scanned as the core section passed through the MSCL-W. Unwashed bulk cuttings for NGR analysis were packed into a 12 cm long core liner, producing a volume of 400 cm³, and measured with the MSCL-W NGR unit.

Gamma ray attenuation density

Bulk density can be used to evaluate pore volume in sediment, which provides information on the consolidation state of the sediment. GRA density is based on the detection of a gamma ray beam produced by a cesium source. The beam, produced by a ¹³⁷Cs gamma ray source at a radiation level of 370 MBq within a lead shield with a 5 mm collimator, is directed through the whole-round cores. The gamma ray detector includes a scintillator and an integral photomultiplier tube to record the gamma rays that pass through the whole-round core. GRA bulk density (ρ_b) is calculated as

$$\rho_b = (1/\mu d) \times \ln(I_0/I),$$

where

- I_0 = gamma ray source intensity,
- I = measured intensity of gamma radiation passing through the sample,
- μ = Compton attenuation coefficient, and
- d = sample diameter.

The Compton attenuation coefficient (μ) and source intensity (I_0) are treated as constants, so ρ_b can be calculated from I . The system is calibrated with a special sealed calibration “core section” composed of a set of aligned aluminum cylinders of various diameters (e.g., 1–6 cm) surrounded by distilled water in a sealed core liner. Density depends on the diameter of the aluminum cylinder and ranges from $\rho = 1$ g/cm³ (water only) to 2.71 g/cm³ (aluminum only). To calibrate the instrument, gamma ray counts were taken for each aluminum cylinder for a count time of 60 s. The resulting $\ln(I)$ was plotted against the product of the known parameters ρ and d of the calibration core section and fitted with a regression line of the following type:

$$\ln(I) = A(\rho \times d)^2 + B(\rho \times d) + C,$$

where d is the internal diameter of the core liner (e.g., 7.3 cm for SD-RCB and 6.6 cm for standard RCB) and A , B , and C are coefficients determined from the polynomial equation fit. Density measurements on core samples were conducted perpendicular to the core axis every 4 cm along the core.

Magnetic susceptibility

Magnetic susceptibility is the degree to which a material can be magnetized by an external magnetic field. Therefore, magnetic susceptibility provides information on sediment mineral composition, but is more generally used to help correlation between boreholes drilled in the same formation. A Bartington loop sensor with an 8 cm diameter was used to measure magnetic susceptibility. An oscillator circuit in the sensor produces a low-intensity (~80 A/m root-mean-square) nonsaturating alternating magnetic field (0.565 kHz). This pulse frequency is converted into magnetic susceptibility. The spatial resolution of the loop sensor is 23–27 mm, and it is accurate to within 5%. Magnetic susceptibility data were collected every 4 cm along the core.

Natural gamma radiation

NGR measurements provide insights into sediment composition, which can be used to identify litho-

logy. Whole-round cores and unwashed cuttings packed in a 12 cm long core liner were monitored for NGR emissions to obtain spatial variability in radioactivity and to establish gamma ray logs of cores for correlation to downhole gamma ray logs. A lead-shielded counter, optically coupled to a photomultiplier tube and connected to a bias base that supplies high-voltage power and a signal preamplifier, is used. Two horizontal and two vertical sensors are mounted in a lead, cube-shaped housing. The NGR system records radioactive decay of long-period isotopes ^{40}K , ^{232}Th , and ^{238}U . NGR has a resolution of 120–170 mm and was measured every 16 cm with a count time of 30 s. Background radiation noise was determined by taking measurements on a water-filled calibration core.

P-wave velocity

P-wave velocity data can be used to evaluate small-strain moduli; to correlate among log, core, and seismic data; and to evaluate pore structure and cementation. P-wave (compressional) velocity (V_p) is defined by the time required for a compressional wave to travel a set distance:

$$V_p = d/t_{\text{core}},$$

where d is the path length of the wave across the core and t_{core} is traveltime through the core.

P-wave velocity transducers on the MSCL-W system measure total traveltime of the compressional wave between transducers. The wave travels horizontally across the whole core and core liner. The total traveltime observed is composed of

- t_{delay} = time delay related to transducer faces and electronic circuitry,
- t_{pulse} = delay related to the peak detection procedure,
- t_{liner} = transit time through the core liner, and
- t_{core} = traveltime through the sediment or rock.

The system is calibrated using a core liner filled with distilled water, which provides control for t_{delay} , t_{pulse} , and t_{liner} . With these calibrations and assuming that the core completely fills the core liner, core velocity (V_p) can be calculated on whole-round specimens in core liners as follows:

$$V_p = (d_{\text{cl}} - 2d_{\text{liner}})/(t_0 - t_{\text{pulse}} - t_{\text{delay}} - 2t_{\text{liner}}),$$

where

- d_{cl} = measured diameter of core and liner,
- d_{liner} = liner wall thickness, and
- t_0 = measured total traveltime.

Electrical resistivity

Electrical resistivity may be useful for estimating other sediment physical properties, including porosity, tortuosity, permeability, and thermal conductivity, although resistivity data must be used with caution because the value is sensitive to all of these parameters, as well as to salinity of pore fluid and mineralogy. Bulk electrical resistivity is controlled by solid grain resistivity, interstitial water resistivity, pore space distribution, and pore connectivity. The noncontact resistivity sensor on the MSCL-W system induces a high-frequency magnetic field in the core with a transmitter coil. This generates an electrical current in the bulk sediment that is inversely proportional to its resistivity. A receiver coil measures the secondary magnetic field generated by this induced electrical current. To measure this smaller magnetic field accurately, a differencing technique has been developed that compares readings from the sample core to readings from an identical set of coils operating in air. Electrical resistivity is estimated from an empirical equation,

$$\rho = a \times E^b,$$

where ρ is the electrical resistivity (Ωm) and E is the sensor response (mV).

The coefficients a and b are obtained by the calibration measurements on five reference core liners filled with different concentrations of NaCl solution (0.35, 1.75, 3.5, 17.5, and 35 g/L). Electrical resistivity data were obtained at 4 cm intervals on the MSCL-W.

Magnetic susceptibility (washed cuttings)

For magnetic susceptibility analysis, $\sim 10\text{ cm}^3$ of vacuum-dried cuttings from the 1–4 and $>4\text{ mm}$ size fractions were placed into a paleomagnetic (pmag) cube. Cubes were weighed empty and then filled with the vacuum-dried cuttings material. The prepared cube, with a volume of 7 cm^3 , was then analyzed with the Kappabridge KLY 3S system (AGICO, Inc.). Sensitivity for the measurement is $3 \times 10^{-8}\text{ SI}$, and intensity and frequency of the field applied are 300 mA/m and 875 Hz, respectively. A standard was measured once a day to ensure long-term quality of the system calibration. A blank empty cube was measured to determine background impact before each sample measurement.

Moisture and density measurements

The purpose of MAD measurements is to obtain general physical properties of sediment or rock specimens such as bulk wet density, bulk dry density, grain density, water content, porosity, and void ratio.

All these properties can be calculated using phase relations in marine sediment from the direct measurements of the wet sample mass (M_{wet}), the dry sample mass (M_{dry}), and the dry sample volume (V_{dry}) (Noorany, 1984). Standard ODP/IODP practices, which include a salt correction, were used to determine interstitial water mass and volume, salt mass and volume, and solid grain mass and volume (Blum, 1997). Standard seawater density (1.024 g/cm³) and salinity (35‰) and a constant salt density (2.22 g/cm³) were assumed for all calculations. MAD measurements were conducted on both cuttings and cores; there is no difference in measurements and calculations between the two sample types, only in sample preparation.

Sample preparation

For core samples, two discrete samples were collected per section for determination of physical properties. MAD samples were taken as a part of cluster samples adjacent to any whole-round core samples including interstitial water, community whole round, and individual requested samples. Sample intervals were chosen at minimally disturbed, homogeneous locations. Special care was taken to avoid drilling mud in MAD samples.

Cuttings samples were taken at 10 m depth intervals of drilling progress for MAD measurement. After being rinsed with seawater, the cuttings of the working portion were separated into different size fractions (0.25–1, 1–4, and >4 mm) by sieving. A volume of ~20 cm³ taken from the 1–4 mm size fraction was used for MAD measurements. Handpicked pieces from the >4 mm size fraction were also used to investigate the difference between DICAs/pillow cuttings and stiffer formation cuttings. Wet cuttings were prepared after sieving to remove excess water by gently wiping cuttings with absorbent paper until no visible water films were observed on the cuttings surfaces. The samples were then placed into a weighed glass jar.

Measurements

The wet sample mass (M_{wet}) was measured using a paired electronic balance system designed to compensate for the ship's heave. The sample mass was counterbalanced with a precisely known mass (40 g for sediment). The sample mass was determined to a precision of ±0.01 g. The balance system was calibrated twice a day or more frequently during poor weather conditions. After measurement, the wet samples were placed in a convection oven for >24 h at 105° ± 5°C to dry. The dry samples were then cooled in a desiccator for at least 1 h to equilibrate to room temperature (~20°C), and then the dry mass

and volume was measured. The dry mass (M_{dry}) was determined using the same measuring system. Dry volume (V_{dry}) was measured using a helium-displacement Quantachrome pentapycnometer with a nominal precision of ±0.04 cm³. The five-chamber system allows the measurement of four sample volumes and one calibration sphere, which was rotated between all measurement chambers to monitor for errors in each chamber. The pycnometer was calibrated at least once per 24 h. An average of four measurements was reported for each sample.

Phase relations in marine sediment

From the direct measurements of M_{wet} , M_{dry} , and V_{dry} pore fluid mass (M_f), salt mass (M_{salt}), mass of solids excluding salt (M_s), pore fluid volume (V_f), salt volume (V_{salt}), and volume of solids excluding salt (V_s) can be obtained by

$$M_f = (M_{\text{wet}} - M_{\text{dry}})/(1 - s),$$

$$M_{\text{salt}} = M_f - (M_{\text{wet}} - M_{\text{dry}})s = (M_{\text{wet}} - M_{\text{dry}})s/(1 - s),$$

$$M_s = M_{\text{wet}} - M_f = [(M_{\text{dry}} - s \times M_{\text{wet}})]/(1 - s),$$

$$V_f = M_f/\rho_f = (M_{\text{wet}} - M_{\text{dry}})/[(1 - s)\rho_f],$$

$$V_{\text{salt}} = M_{\text{salt}}/\rho_{\text{salt}} = (M_{\text{wet}} - M_{\text{dry}})s/[(1 - s)\rho_{\text{salt}}], \text{ and}$$

$$V_s = V_{\text{dry}} - V_{\text{salt}} = V_{\text{dry}} - (M_{\text{wet}} - M_{\text{dry}})s/[(1 - s)\rho_{\text{salt}}],$$

where

M_{wet} = total mass of the wet sample,

M_{dry} = mass of the dried sample,

s = salinity (3.5%),

ρ_f = density of pore fluid (1.024 g/cm³), and

ρ_{salt} = density of salt (2.220 g/cm³).

Calculations of physical properties

Water content (W_c) was determined following the methods of the American Society for Testing and Materials (ASTM) designation D2216 (ASTM International, 1990). Corrections are required for salt when measuring the water content of marine samples. In addition to the water content calculation in ASTM D2216 (i.e., the ratio of pore fluid mass to dry sediment mass as percent dry weight), we also calculated the ratio of pore fluid mass to total sample mass (percent wet weight). The equations for water content are

$$W_c (\% \text{ dry weight}) = (M_{\text{wet}} - M_{\text{dry}})/(M_{\text{dry}} - sM_{\text{wet}}) \text{ and}$$

$$W_c (\% \text{ wet weight}) = (M_{\text{wet}} - M_{\text{dry}})/[M_{\text{wet}}(1 - s)].$$

Bulk density (ρ_b), dry density (ρ_d), and grain density (ρ_g) are defined as

$$\begin{aligned}\rho_b &= M_{\text{wet}}/V_{\text{wet}} = M_{\text{wet}}/(V_{\text{dry}} + V_f - V_{\text{salt}}), \\ \rho_d &= M_{\text{dry}}/V_{\text{wet}} = M_{\text{dry}}/(V_{\text{dry}} + V_f - V_{\text{salt}}), \text{ and} \\ \rho_g &= M_s/V_s = M_s/(V_{\text{dry}} - V_{\text{salt}}),\end{aligned}$$

where V_{wet} is the bulk volume of wet sample determined from the dry volume (V_{dry}), pore fluid volume (V_f), and salt volume (V_{salt}).

Porosity (ϕ) is the volume of the pores to the total sample volume; void ratio (e) is the pore volume to the volume of the solid grains. They are calculated as

$$\begin{aligned}\phi &= V_f/V_{\text{wet}} \text{ and} \\ e &= V_f/V_s.\end{aligned}$$

***P*-wave velocity, electrical conductivity, and dielectric permittivity (cores and cuttings)**

P-wave velocity and electrical resistivity measurements were performed on cuttings and cubic samples cut from rock cores with a diamond blade saw. Cubic samples for *P*-wave velocity and electrical resistivity measurements were ~ 20 mm \times 20 mm \times 20 mm. Cubes were cut with faces orthogonal to the x -, y -, and z -axes of the core reference. This three-component measurement plan enables first-order estimation of both *P*-wave velocity and electrical resistivity anisotropies. *P*-wave measurements on cuttings were generally made in only one direction. The cuttings were sanded with medium grain abrasive paper in order to form two parallel facets at least 0.5 cm apart. For impedance measurements, handpicked cuttings were reshaped into a flat right prism with abrasive paper. This resulted in the thickness of the platelet ranging from 2.5 to 5–6 mm.

A *P*-wave logger for discrete samples (PWL-D) was used to measure *P*-wave velocity. The sample is held between two transducers acting as transmitter and receiver. The PWL-D stand has a laser distance sensor and two interchangeable sets of transducers with resonant frequencies at 230 and 500 kHz, respectively. The transmitting transducer was connected to a pulse generator, and the receiving transducer was connected to an oscilloscope synchronized with the pulse generator. The oscilloscope signal was displayed digitally, and the *P*-wave total traveltime (t) for the first arrival was picked and recorded. The laser distance sensor provided the sample length (L). The velocity in any direction (i.e., V_{px}) was defined by the sample length (i.e., L_x), total traveltime (t_x), and system-calibrated delay time (t_{delay}):

$$V_{\text{px}} = L_x/(t_x - t_{\text{delay}}).$$

Traveltime delay was determined by placing the transmitter and receiver in direct contact and measuring traveltime. The laser distance sensor was calibrated by placing the transmitter and receiver into direct contact with each other and then by measuring a 2.5 cm long reference specimen. Quality control measurements were made daily by measuring velocity on acrylic standards with known lengths and acoustic velocities.

Measurements on cores from Hole C0002M were performed with the 230 kHz transducers to minimize attenuation on the less consolidated samples. Measurements on cuttings were performed with the 500 kHz transducers to minimize wavelength so that the ray path always remains more than half the wavelength. Measurements on deep cores (Holes C0002N and C0002P) were also performed with the 500 kHz transducers, as they provide more precision when picking the arrival times. The true average frequency of the wave train transmitted across the sample was found to be 270 and 400 kHz for the 230 and 500 kHz transducers, respectively. Heterogeneous or attenuating samples, as well as samples with irregular shapes, displayed important distortion of the wave train. As the automated pick was on the second zero crossing (rather than on the first arrival), these measurements were discarded as unreliable.

Because *P*-wave velocity is measured in the x -, y -, and z -directions, the anisotropy is calculated following the approach of Carlson and Christensen (1977). Some sources of anisotropy include (1) alignment of pores during consolidation, (2) fabric development due to alignment of mineral grains, and (3) microstructures such as microfractures and microcracks. The *P*-wave velocity horizontal-plane anisotropy (α_{VPhor}) and vertical-plane anisotropy (α_{VPvert}) calculation compares the horizontal (x and y) and vertical (z) components of *P*-wave velocity expressed as a percentage of the mean:

$$\begin{aligned}\alpha_{\text{VPhor}} (\%) &= 200[(V_{\text{px}} - V_{\text{py}})/(V_{\text{px}} + V_{\text{py}})] \text{ and} \\ \alpha_{\text{VPvert}} (\%) &= 200[(V_{\text{px}} + V_{\text{py}})/2 - V_{\text{pz}}]/[(V_{\text{px}} + V_{\text{py}})/2 + V_{\text{pz}}].\end{aligned}$$

Resistivity was measured on the same discrete cubic samples used for *P*-wave velocity measurements. A cube of known dimensions is held between two electrodes, and complex impedance is measured with a 40 Hz to 110 MHz frequency sweep with the Agilent 4294A impedance analyzer. Sample dimensions are obtained during *P*-wave velocity measurement. Coupling between the sample and each stainless steel

electrode is obtained through insulating plastic film for the measurements of dielectric properties and through a filter soaked in 35 g/L NaCl solution for the measurement of electrical conductivity. The impedance of the sample for each configuration is obtained by subtracting the impedance of the coupling layers from the measured impedance. The impedance of the coupling layers is evaluated by stacking of the two plastic films or the two filters between the electrodes immediately after measuring the impedance of the sample. Sample conductivity (σ_x) and dielectric permittivity (ϵ_x) in the x -direction are computed from measured real and complex impedance components R_x and X_x by

$$\sigma_x + j2\pi f\epsilon_x = (L_x/L_y L_z)[(R_x - R_0) - j(X_x - X_0)] / [(R_x - R_0)^2 + (X_x - X_0)^2],$$

where L_x , L_y , and L_z are the length of cubic discrete samples in the x -, y -, and z -direction, respectively; R_0 and X_0 refer to the measured impedance of the filter; and f is the frequency. Conductivities in the y - and z -directions are obtained by substitution.

In the case of cuttings, L_y and L_z are not known because the shape of the platelet was generally irregular. Instead, its area (equivalent to $L_y \times L_z$) was calculated by dividing the volume by the thickness (L_x). The volume was determined from the wet weight and dry weight of the platelet and by assuming a grain density as determined from MAD measurement on the corresponding bulk sample of cutting.

Resistivity is calculated as the inverse of the real conductivity. To minimize electrode polarization effects on conductance and to remain consistent with Expedition 315 data and reports, the values of conductivity and resistivity at 10 kHz are reported. Raw data from Expedition 338 have been reprocessed to yield conductivity at 10 kHz and are also given in “**Physical properties**” in the “Site C0002” chapter (Tobin et al., 2015) (resistivity at 2 kHz are given in Strasser et al., 2014b). The laboratory temperature is also reported for each measurement in order to allow correction to in situ temperature and comparison with logging data. The dielectric permittivity obtained in the 40–110 MHz frequency range of the Agilent 4294A impedance analyzer with saltwater-coupled electrodes is affected by electrode polarization effects and is not reported.

Similar to the P -wave velocity anisotropy, the electrical resistivity horizontal-plane anisotropy (α_{Rhor}) and vertical-plane anisotropy (α_{Rvert}) calculation compares the horizontal (x and y) and vertical (z) components of resistivity expressed as a percentage of the mean:

$$\alpha_{\text{Rhor}} (\%) = 200[(\sigma_x - \sigma_y)/(\sigma_x + \sigma_y)] \text{ and}$$

$$\alpha_{\text{Rvert}} (\%) = 200[(\sigma_x + \sigma_y)/2 - \sigma_z]/[(\sigma_x + \sigma_y)/2 + \sigma_z].$$

Dielectric permittivity and electrical conductivity (washed cuttings)

Dielectric permittivity is a measure of the electrical polarizability of a material (Von Hippel, 1954). The dielectric permittivity of a sample (ϵ) is often presented as a product of relative permittivity (ϵ_r) and vacuum permittivity (ϵ_0):

$$\epsilon = \epsilon_r \epsilon_0.$$

Typically dielectric processes occurring on a large scale provide a high dielectric permittivity, but because of extra work required to drive these processes, they also have a longer time constant and “turn off” at a lower frequency. Each dielectric process involves both the displacement of charge carriers (energy absorption), denoted by the real component of the dielectric permittivity (ϵ'), and work required to achieve polarization (energy dissipation), denoted by the imaginary dielectric permittivity (ϵ'') along with a characteristic frequency or speed at which it occurs governed by the momentum (and kinematics) of the charge carriers (Guéguen and Palciauskas, 1994), where

$$\epsilon = \epsilon' - j\epsilon''.$$

Note that conduction also gives rise to energy dissipation, and many dielectric analyses combine both loss mechanisms into one loss term, either expressed as an equivalent imaginary dielectric permittivity ($\epsilon''_{\text{equiv}}$) or an equivalent conductivity (σ_{equiv}).

The specific challenges and requirements of Expedition 348 included the need for a very portable system that can be deployed on a ship working at sea where rock and sample preparation opportunities are limited. We used a mobile dielectric laboratory based on the end-loaded transmission line method of Burdette et al. (1980) and Stuchly and Stuchly (1980). This particular method was selected because it is fast, requires <25 g of well-chosen sample, and can be applied to powdered sample, making it ideal for drill cuttings.

End-loaded transmission line dielectric probes use a section of transmission line of known characteristic impedance (determined by the geometry of the inner and outer conductor diameters) that is pressed against the sample. A network analyzer (Agilent 8753D) was used to investigate the change in electromagnetic impedance at the interface between the transmission line and the sample (measuring the so-

called scattering [S-] parameters), which were then used to calculate the real and imaginary dielectric permittivity. The network analyzer automatically swept the frequency during these measurements from 300 kHz to 3 GHz, so the dielectric relaxation of the sample could be recorded. Most of this is controlled automatically; however, a number of user-based procedures were carried out prior to measurement. These included the measurement of the scattering parameters for standard reference materials, which the machine uses to correct the scattering parameters of the test samples.

An Agilent (85092-60010) Ecal module was installed near the end of the transmission line so that routine drift corrections could be performed automatically. We used transmission line probes developed by Commonwealth Scientific and Industrial Research Organisation specifically for investigating rock samples (Fig. F18). This method is ideal for samples ranging in hardness from liquids to soft intact shales.

Drill cuttings samples were collected during Expedition 348 at 5 m intervals. We subsampled as many of these intervals using the drill cuttings selection procedure described elsewhere in the chapter to separate the drilling mud from the formation rock. We used the biggest drill cuttings fragments available to minimize the risk of drilling mud contamination. Subsamples of 20 g from the 1–4 mm fraction were ground into a fine powder using a ring mill (see “[X-ray diffraction](#)”) and mixed with 20 g of deionized water in a Nunc centrifuge bottle. The samples were shaken briefly by hand to ensure that the salts and agglomerates were dissolved, and then the mixture was centrifuged at 5000 rpm for 1 h. The excess water was decanted into a separate plastic jar to measure its salt content using the interstitial water analysis procedure (see “[Geochemistry](#)”).

The remaining cuttings paste inside the centrifuge bottle was extruded into a separate acrylic jar with known mass, molded gently to ensure uniformity (without excess water or trapped air bubbles), and pressed against the end-load coaxial transmission line. Four dielectric measurements were conducted at different locations on each paste sample for quality control. After measurement, the sample was weighed before and after oven drying at 105°C until mass stabilization (typically 24 h) to determine the moisture content of the paste. At completion, a number of physical attributes of the paste and the pore water salinity were estimated, including the salt content of the decanted water and porosity results of the cuttings (see “[Moisture and density measurements](#)” in the “[Site C0002](#)” chapter [Tobin et al., 2015]) to complement the real and imaginary dielectric permittivity spectrum.

Thermal conductivity

Thermal conductivity was measured on working-half cores using a half-space line source (Vacquier, 1985), which approximates an infinite line source. Samples were placed in a seawater bath for at least 15 min before measurement, and then the half-space probe was placed directly on the split core parallel to the core axis.

All measurements of thermal conductivity were made after the cores had equilibrated to room temperature. At the beginning of each measurement, temperature in the sediment was monitored to ensure that thermal drift was <0.4 mK/min (typically within 1–2 min). After it was established that the temperature was near equilibrium, a calibrated heat source was applied, and the rise in temperature was recorded for ~60 s. For optimal measurement conditions, heat source power was adjusted as a function of the thermal conductivity of the sample. Values of thermal conductivity were based on the observed rise in temperature for a given quantity of heat. The probe was calibrated at least once every 24 h. The calibration was performed on Macor blocks of known thermal conductivity, which is $1.652 \text{ W}/(\text{m}\cdot\text{K}) \pm 2\%$.

Anelastic strain recovery analysis

The anelastic strain recovery (ASR) technique is a core-based stress measurement that can evaluate both orientation and magnitude of three-dimensional present-day principal stress on rock. The ASR approach is to measure the anelastic strain change by releasing the stress soon after core recovery. The methodology used for ASR measurement during Expedition 348 is based on Matsuki (1991), following the guideline described in Lin et al. (2007). A ~15 cm long undisturbed whole-round core sample was corrected after XRCT scanning for screening for potential important structural sections. We did not perform MSCL-W measurements because ASR measurement is very time sensitive and requires instrumentation as soon as possible after core is extracted from the subsurface to capture early strain recovery. Core samples were pushed out of their core liners, and the outer surface was washed in seawater to remove drilling mud.

Before starting the ASR measurement, the dimensions of an elliptical section of core sample was measured by a 2-D measurement sensor (Keyence Corporation; TM-065) while rotating the core samples on the rotary table (Fig. F19). This measurement was carried out to capture initial elastic strain recovery in the core samples. The precision of the measurement is $\pm 0.2 \text{ }\mu\text{m}$.

The anelastic strains shown by elliptical shape of the specimens in nine directions, including six independent directions, were measured using 18-wire strain gauges (6 cross- and 6 single gauges; Fig. F20). In cases where a few fractures had developed in the specimen, the fractures were glued to prevent the sample from splitting into pieces. It took 1 to 2 h to mount 18 strain gauges, and the total elapsed time just after core on deck was 1–2 h before starting to record the strain recovery. The core samples were double-bagged (with plastic and aluminum) and submerged in a thermostatic water bath in which temperature changes were kept controlled at $22^\circ \pm 0.1^\circ\text{C}$ for the duration of the measurement. Strain values were collected every 10 min for up to a maximum of 15 days.

MSCL-I: photo image logger (archive halves)

Digital images of archive-half cores were acquired by a line-scan camera equipped with three charge-coupled devices (CCD). Each CCD has 2048 arrays. The reflected light from the core surface is split into three channels (red, green, and blue [RGB]) by a beam splitter inside the line-scan camera and detected by the corresponding CCD. The signals are combined, and the digital image is reconstructed. A correction is made for any minor mechanical differences among the CCD responses. A calibration is conducted before scanning each core to compensate for pixel-to-pixel response variation, uneven lighting, and lens effects. After colors of black (RGB = 0) and white (RGB = 255) are calibrated with an f -stop of $f/16$, the light is adjusted to have an adequate gray scale of RGB = 137 at an f -stop of $f/11$. Optical distortion is avoided by precise movement of the camera, and the spatial resolution is 100 pixels/cm.

MSCL-C: color spectroscopy (archive halves)

A diffuse-reflectance spectrophotometer is used to measure core color. The MSCL-C system is an xyz -type aluminum frame equipped with a color spectrophotometer (Konica-Minolta; CM-2600d). Six core sections can be scanned simultaneously by the sensor unit (including the spectrophotometer and small distance measuring system using a laser sensor). The sensor moves over each section and down at each measurement point to measure the split archive-core surface. The reflected light is collected in the color spectrophotometer's integration sphere and divided into wavelengths at a 10 nm pitch (400–700 nm). The color spectrum is then normalized by the source light of the reflectance and calibrated with the measurement of a pure white standard. The measured

color spectrum is normally converted to lightness (L^*) and chromaticity variables a^* and b^* (see Blum, 1997, for details). These parameters can provide information on relative changes in bulk material composition that are useful to analyze stratigraphic correlation and lithologic characteristics and cyclicity.

Downhole measurements

Leak-off test

A leak-off test (LOT) is used by drilling engineers to determine the maximum mud weight that can be used for drilling without damaging the formation by hydraulic fracturing. If properly conducted, results of LOTs may also become useful for inferring the magnitude of the least principal stress in the formation. In a LOT, pumping drilling fluid into a closed wellbore at a constant rate pressurizes a small section of the formation. By observing the pressure history during fluid injection, one can identify changes in pressurization rate, formation breakdown, and steady-state pressures to infer the progress of hydraulic fracture formation/propagation and, ideally, the magnitude of the least principal stress (e.g., Zoback, 2007).

Injection of mud into an elastically responding borehole leads to a linear relationship between the injected mud volume and the borehole pressure. The leak-off point (LOP) corresponds to the pressure and volume at which the relationship deviates from a linear-elastic trend as a result of fracture volume creation. At the LOP, the gradient of pressure versus injected volume decreases because drilling mud escapes into the formation. If injection continues beyond the LOP, the formation may break down as the peak pressure (formation breakdown pressure) is reached and a hydraulic fracture is created. If enough fluid volume is injected to cause a hydraulic fracture to propagate away from the near-wellbore region, pressure at shut-in or fracture closure pressure can be observed to infer the magnitude of the least principal stress (Zoback, 2007). Even if hydraulic fracture propagation is not achieved, pressure at the LOP is commonly thought to give the magnitude of the least principal stress (S_3), especially if there is a clear LOP. However, the mechanical correspondence between the pressure at LOP and S_3 is not well understood, and the pressure at the LOP is often observed to be higher than S_3 (Raaen et al., 2006). When the LOP is not clear, it is especially difficult to interpret the data other than to establish drilling engineering limits.

LOTs were carried out at the top of the 12¼ inch Hole C0002P borehole after a sidetrack hole was drilled out of Hole C0002N at 1936.75 mbsf (3904.25

m BRT). The test was conducted after 18 m of the formation was exposed (1936.75–1954.5 mbsf; 3904.25–3922.0 m BRT) in the sidetrack hole. The LOT was conducted with the outer annulus closed by the blow-out preventer, and mud pressure was measured at the cement pumps. The pressure at the bottom of the hole was calculated by the recorded pressure plus the static pressure of the mud column (mud density = 1.16 specific gravity). Two cycles of pressurization were conducted at 0.25–0.32 and 0.7–0.8 bbl/min injection rates. After shut-in, mud pressure was observed for ~10 min to monitor the pressure decay behavior. The drilling engineer provided pressure, volume, and pump-rate data after the test was conducted. Volume and pump-rate data, recorded based on counts of pump strokes, were known to be inaccurate, so they were corrected based on the consumed mud volume directly observed at the mud tank during the LOT operation.

Logging

LWD and MWD tools sample in situ physical properties and downhole drilling parameters that can be analyzed both in real time by using mud-pulse telemetry and after recovering the BHA and downloading the memory data. For Expedition 348, LWD/MWD acquisition was performed under contract by Halliburton Sperry Drilling Services. Because MWD/LWD data are recorded soon after initial drilling, these measurements are less affected by drill mud formation invasion and disturbance when compared to wireline logging. Time after drilling and exposure time are basic quality control parameters for the analysis and the interpretation of LWD data. Expedition 348 LWD/MWD data were integrated with, and compared to, data sets from cuttings, core, and seismic reflection imaging to constrain structure, lithology, and physical properties.

Two different BHAs were used while drilling the 17 inch diameter Hole C0002N in Run 1 and Run 2 (Fig. F21A, F21B), and another BHA was used for the 12¼ inch diameter Hole C0002P (Fig. F22). The BHA is chosen based on drilling requirements, borehole diameter, and tool availability. Tool specifications and acronyms are shown in Tables T12, T13, T14, and T15.

In Hole C0002N, LWD/MWD data were collected from 872 to 2329.5 mbsf. The LWD/MWD data were acquired in two logging runs using the two different BHAs: Run 1 from 872.5 to 2008.5 mbsf (2840.00–3976.00 m BRT) (Fig. F21A) and Run 2 from 2008.5 to 2329.5 mbsf (3976.00–4297.00 m BRT) (Fig. F21B). In Hole C0002P, LWD/MWD data were col-

lected from 2162.5 to 3058.5 mbsf (4130–5026 m BRT) (Fig. F22). No LWD/MWD data were recorded through the sidetrack kick-off section (3904–4130.5 m BRT) prior to coring. After coring, LWD/MWD recorded reaming of the cored interval (4130.5–4186.0 m BRT) and continued to Hole C0002P total depth.

The LWD/MWD tools recorded a complete data set of geophysical measurements including gamma radiation, annular pressure and mud temperature, resistivity logs and azimuthal resistivity images, compressional and shear sonic velocity, acoustic directional images, and ultrasonic caliper. LWD/MWD tools used in the acquisition of Expedition 348 data included Halliburton's MWD control unit, electromagnetic wave resistivity (EWR) (Figs. F23, F24), pressure while drilling (PWD), and dual gamma ray (DGR) (Fig. F21A) in the 17 inch Hole C0002N. The azimuthal focused resistivity (AFR) tool (Fig. F25), X-Bimodal AcousTic (XBAT) sonic tool (Fig. F26), and azimuthal gamma ray (AGR) tool were added to the LWD tool string for the Hole C0002P 12¼ inch section. EWR-PHASE4 was only run in Run 1 of Hole C0002N; the EWR-M5 was used for Hole C0002P.

LWD acquisition systems and tools

LWD/MWD equipment contains data memory and battery power within the tool string. Real-time monitoring of drilling and data analysis is performed by transmitting from the tool string to the ship via a modulated pressure wave within the drilling mud (mud-pulse telemetry). Only a subsample of recorded LWD data was sent because of limited bandwidth. Based on the type of information and relevance for formation characterization, specific channels were chosen for real-time transmission. MWD data on drilling parameters such as drilling speed, rate of penetration, and stick-slip indicators were transmitted together with the LWD logs for log quality check during the acquisition. The mud pulser failed at 2260.5 mbsf during drilling of Hole C0002P, ending real-time data transmission and monitoring for the hole. Full resolution logs from each tool's memory only became available when the BHA was recovered and downloaded. The resistivity imaging data acquired with the AFR tool could not be downloaded immediately due to a failure in the connector that was detected when the tool was retrieved. The AFR tool had to be offloaded and sent to a Halliburton facility for data retrieval and processing, which caused several weeks' delay before the data became available.

The individual tools that were used during Expedition 348 are described below.

Dual gamma ray

The DGR LWD tool provides a measurement of NGR in API units. Two Geiger-Müller detectors, each with independent counting circuits, create a redundant configuration (Halliburton, 2012a). This dual detection system provides two independent NGR logs, which are processed for best accuracy and precision of the measurement. LWD DGR logs generally produce a better vertical resolution compared to equivalent wireline logs because of slower drilling speeds. Gamma ray logs were corrected for borehole size, mud weight, and mud potassium content.

Azimuthal gamma ray

The AGR sensor measures the NGR activity of the formation. Using two scintillation crystals, this LWD tool has a measurement range of 0–849 gAPI with an accuracy of $\pm 5\%$. Because the AGR sensor is located only 1.8 ft (0.55 m) from the bottom of the tool (Fig. F21A), it provides a very early indication of changes in lithology while drilling with imaging capability and near-bit positioning.

EWR-PHASE4

This LWD resistivity measurement is based on electromagnetic wave propagation and utilizes a high-frequency induction resistivity sensor. The tool comprises four radio-frequency transmitters and a pair of receivers (Fig. F23). By measuring both the phase shift and the attenuation for each of the four transmitter-receiver spacings, eight resistivity curves with corresponding different depths of investigation are recorded. The measurement range for phase-shift resistivity is 0.05–2000 Ωm . The measurement range for attenuation resistivity is 0.1–100 Ωm (Halliburton, 2012b).

EWR-M5

This LWD resistivity measurement is similar to the EWR-PHASE4 but is optimized by use of data from vibration and pressure sensors. It contains a drill string dynamic sensor, which consists of a triaxial accelerometer to monitor and minimize vibrational noise (Halliburton, 2012c). The tool consists of six transmitters in two sets of three separated by three receivers (Fig. F24). Measurements include 30 unique compensated resistivity sets of both phase shift and attenuation resistivity at 2 MHz, 250 kHz, and 500 kHz. The measurement range for phase-shift resistivity is 0.05–2000 Ωm . The measurement range for attenuation resistivity is 0.1–100 Ωm .

Azimuthal focused resistivity

The AFR tool complements the EWR measurements for high-resolution resistivity images in highly conductive mud and collects electrical images of the formation, omnidirectional and azimuthal laterolog-type resistivity, and at-bit resistivity. Resistivity images are collected using two rows of imaging buttons with two depths of investigation for this 8 inch tool (Fig. F25). Full image coverage is obtained from each row containing three button electrodes separated by 120° . Image resolution is 10 mm for these high-resolution sensors, and the data are acquired in 128 discrete azimuthal bins with 16 bins available in real time for analysis (Halliburton, 2012d). Bedding and fracture orientation can be interpreted from these images, as well as drilling-induced fractures and borehole breakouts, which is used to help estimate the stress field orientation and constrain stress magnitudes.

Pressure while drilling

This LWD tool provides real-time downhole pressure information, including annular pressure and internal pressure measurements by using two high-accuracy quartz gauges (Fig. F24). It also records tool temperature. During mud noncirculation periods (e.g., LOTs and pumps-off phases), the minimum, maximum, and average pressures are recorded and later transmitted when circulation restarts. The tool can be used to detect well flows and kicks (Halliburton, 2012e), as well as equivalent circulating density (see “Introduction and operations”).

X-Bimodal AcousTic

The XBAT tool produces azimuthal sonic and ultrasonic measurements by using four azimuthal transmitters, four azimuthal arrays of receivers (6 receivers per array), and a 4-pinger-axis ultrasonic caliper (Fig. F26). Each transmitter can independently fire either a positive or negative wave. This allows acquisition in monopole, dipole, quadruple, and crossed-dipole modes. We used both the monopole and dipole modes with the source frequency between 2 and 25 kHz. Receivers record full waveform acoustic signals and are isolated from the drill collar to reduce bit noise and mud circulation noise. The ultrasonic caliper determines borehole size and shape with an accuracy of ± 3.8 mm, which can also help in the identification of wellbore failures not clearly identified in resistivity image logs.

The XBAT tool has a (manufacturer claimed) measurable limit of compressional slowness range of 40–

190+ $\mu\text{s}/\text{ft}$ (<1.6–7.6 km/s) and shear slowness range of 60–550+ $\mu\text{s}/\text{ft}$ (<0.55–5.1 km/s) (Halliburton, 2013).

Onboard data flow

The LWD tools recorded data at a preset frequency based on logging speed and tool-optimized resolution, providing measurements as a function of time. For standard interpretation and correlation with shipboard sample measurements, the LWD and MWD data need to be referenced to depth below seafloor (mbsf), reported for logging purposes as meters LSF. Halliburton's integrated logging and drilling surface system, which was installed onboard the *Chikyu*, was used to record and control the rate of penetration and depth of the drill string at any given time while logging. This was determined using the length of the drill string and derrick top drive position. A crown-mounted motion compensator on top of the derrick helped reduce errors from heave and improved weight-on-bit accuracy.

The real-time data were uploaded to the server every 12 h for initial interpretation by shipboard scientists. Due to the very deep drilling and long bit run times, recovery of the memory data occurred after each run. Data referenced in time were processed to meters BRT. The depth reference was then converted to meters LSF. Data were then distributed in DLIS format, and the main scalar logs were extracted and converted into LAS files.

Data quality assessment

Cross-correlating LWD/MWD data for primary quality assessment included the use of downhole drilling parameters, drilling control logs, and geophysical control logs. The logging staff scientists documented the LWD/MWD operations and converted the raw data received from the Halliburton engineer to the LSF depth scale. Resistivity scalar logs and ultrasonic caliper were used for data quality assessment, permitting analysis of borehole conditions (e.g., caving, washout, bridges, and invasion) for potential effects on logging data. Borehole images were also used to assess borehole conditions. However, regions of high stick-slip affect image quality. Time elapsed after passage of the drilling bit for the main geophysical measurements was also monitored for quality check along with drilling operations. Because of variations in sampling time, all measurements may have insufficient heave compensation and/or unaccounted movements, including bending, shocks, and vibrations of the BHA, creating errors in local depth measurements of up to tens of centimeters.

Real-time quality control

Logging scientists and the logging staff scientist continuously observed the real-time data feed and closed-circuit television feed from the rig floor. This provided an initial quality check on the data and tracking of events (e.g., time off bottom) that could affect the log response. Parameters included observations of sonic log values, resistivity, gamma radiation, annular pressures, torque, weight-on-bit, rate of penetration, and mud volume.

Log and image interpretation

Change in the log response, such as changing values and/or frequency of the signal, are often related to variation of the composition and/or texture of sediment and rock. Therefore, these features were used to define and characterize formation properties. Log units were characterized through both qualitative and quantitative methods.

Lithologic log unit characterization

The geometry of log unit boundaries and bedding information were defined based on scalar LWD logs and included borehole images for Hole C0002P. Trends were analyzed on all the available logs, and rock textures/structures were analyzed using borehole images. Sonic logs and resistivity images helped with textural interpretations. Gamma ray analysis aided in evaluation of composition.

Unit definition used all available LWD/MWD log variations to define distinct geological features and allowed for

- Defining and characterizing each log unit, sub-unit, and unit boundary;
- Categorizing composition and trends within each unit; and
- Interpreting geological features based on log data.

Lithology, from unit scale to bed scale, was primarily determined from gamma ray logs along with resistivity and sonic logs (for Hole C0002P). Higher or lower gamma radiation is the primary discriminant for clay-rich or sand-rich interval interpretation, respectively. Borehole images helped to characterize geological features such as bedding orientation, faults, fractures, sedimentary structures, bed boundaries, and unconformities. Log units were correlated to this and previous IODP expeditions' core, cuttings, and seismic data at Site C0002 (Expedition 314 Scientists, 2009; Expedition 332 Scientists, 2011; Strasser et al., 2014b) to further refine the interpretations (see "[Lithology](#)").

Structural interpretation from logs

Structural analysis was performed on AFR images in the lower section using TechLog software (Schlumberger). The azimuthal button resistivity data were displayed unwrapped as 360°-oriented images of the borehole wall for interpretation and dip measurements. As part of the workflow for image analysis, dynamic and static normalization were performed on the resistivity images. Static normalization shows overall change in resistivity in a single borehole, as it displays a color scale covering the entire range of resistivity (e.g., 0.2–200 Ωm) for a single borehole. Dynamic normalization recalculates the displayed color scale range for a specific interval of resistivity and is thus useful for bringing out subtle details in a log such as changes in facies or lithology, natural and drilling-induced fracture resistivity, or borehole breakout width.

Resistivity contrasts in the rock are the basis for the identification and interpretation of geological features on the resistivity images. Dipping planar surfaces are identified as sinusoidal curves of similar contrast in unwrapped AFR images. Dip and azimuth of fractures, faults, and bedding were determined by fitting sinusoids to the image data. Artifacts appear in the processed data due to stick-slip and insufficient heave corrections. Borehole diameter was obtained from the ultrasonic caliper. The borehole size was set to match a constant bit size (12¼ inches) to calculate dip in cases where an independent caliper measurement was missing. This assumption may cause dip overestimates in regions of large borehole diameter, introducing small dip angle errors. This means the reported dips should be viewed as maximum values. AFR depth of investigation was also one of the parameters used for dip angle calculation.

Using the background resistivity as a base, we classed fractures as conductive or resistive, in which we only classified unambiguous fractures. Clear crosscutting or dramatic variation in dip to bedding formed the bases for fracture classification in addition to azimuth orientation and fracture density.

Borehole wall analysis

Stress orientation within the borehole can, in principle, be determined by using both borehole breakouts and drilling-induced tensile fractures (DITFs). The vertical stress (S_v), two horizontal principal stresses (S_{HMIN} and S_{HMAX}), and fluid pressures are considered to control the circumferential stress azimuthal around the borehole. Borehole breakouts form when the maximum circumferential stress exceeds the formation compressive strength. In a vertical well, breakouts appear in resistivity images as parallel and

vertical conductive features 180° apart from each other in the direction of S_{HMIN} . The minimum circumferential stress arises in the direction of S_{HMAX} where DITFs form if the effective circumferential stress becomes negative (tensional). DITFs appear as vertical pairs of cracks 180° apart if the borehole axis is aligned with the vertical stress but could form en-echelon patterns of inclined cracks if the borehole axis is deviated from the vertical (Zoback, 2007).

Interpretation of shallow, medium, and deep button resistivity images provided the orientation of breakouts and DITFs, integrated with sonic data to constrain the results. Resistivity images were oriented to give measured azimuths and widths of breakouts along with DITFs in true azimuth for estimation of horizontal principal stress direction. The ultrasonic caliper provided a 3-D borehole shape image used to assess breakouts and/or borehole elongation and ellipticity.

Integration with lithologic interpretations helped determine variations in the formation's strength, stress, and/or pore pressure. Comparison with MWD drilling parameters assisted in analysis of borehole stability, mud pressure surges, and formation strength.

X-ray computed tomography

XRCT imaging provided information about structures and sedimentological features in the core and helped to assess sample locations and quality for whole-round samples. Our methods followed those in the measurement manual prepared by the Center for Deep Earth Exploration (X-ray CT scanning, version 1.00; 26 Dec 2008) and used on previous expeditions (e.g., Expeditions 315, 316, 319, 322, and 331). The manual is based on GE Healthcare (2006), Mees et al. (2003), and Nakano et al. (2000).

The XRCT scanner on the *Chikyu* is a LightSpeed Ultra 16 (GE Yokogawa Medical Systems, Ltd.), capable of generating sixteen 0.625 mm thick slice images every 0.5 s (the time for one revolution of the X-ray source around the sample). Data generated for each core consist of core-axis-normal planes of X-ray attenuation values with dimensions of 512 × 512 pixels. Data were stored as Digital Imaging and Communication in Medicine (DICOM) formatted files.

Background

XRCT has been well established through medical research and is very briefly outlined here. CT images are built up from spatial distribution of the "CT value":

$$\text{CT value} = [(\mu_t - \mu_w)/\mu_w]K,$$

where μ_t is the coefficient of absorption at scanning point, μ_w is the coefficient for absorption of water, and K is a constant (Hounsfield value) (Otani et al., 2010).

Analytical standards used during Expedition 348 were air (CT number = -1000), water (CT number = 0), and aluminum (2477 < CT number < 2487) in an acrylic core mock-up. All three standards were run once daily after air calibration. For each standard analysis, the CT number was determined for a 24.85 mm² area at fixed coordinates near the center of the cylinder.

XRCT scan data usage

XRCT scans were used during Expedition 348 to

- Examine 3-D features of deformation structures, bioturbation, and so on;
- Distinguish “natural” fractures or faults and drilling-induced fractures;
- Measure dip angles of structures such as faults, bedding, veins, and so on;
- Provide an assessment of core and core liner integrity;
- Determine locations for whole-round samples; and
- Identify important structural and sedimentological features to be avoided by whole-round sampling.

XRCT scanning was done immediately after core cutting for selection of time-sensitive (interstitial water, microbiology, and organic geochemistry) samples. All whole-round core sections were screened to avoid destructive testing on intervals that might contain interesting structural or sedimentological features. This also facilitated identifying intervals with minimal drilling disturbance for whole-round sampling and for assessing heterogeneity (essential for postexpedition studies of frictional, geotechnical, and hydrogeological properties).

References

ASTM International, 1990. Standard method for laboratory determination of water (moisture) content of soil and rock (Standard D2216-90). In *Annual Book of ASTM Standards for Soil and Rock* (Vol. 04.08): Philadelphia (Am. Soc. Testing Mater.). [revision of D2216-63, D2216-80]

Blum, P., 1997. Physical properties handbook: a guide to the shipboard measurement of physical properties of deep-sea cores. *ODP Tech. Note*, 26. doi:10.2973/odp.tn.26.1997

Burdette, E.C., Cain, F.L., and Seals, J., 1980. In vivo probe measurement technique for determining dielectric properties at VHF through microwave frequencies. *IEEE Trans. Microwave Theory Tech.*, 28(4):414–427. doi:10.1109/TMTT.1980.1130087

Byrne, T., 1984. Early deformation in melange terranes of the Ghost Rocks Formation, Kodiak Islands, Alaska. In Raymond, L.A. (Ed.), *Melanges: Their Nature, Origin, and Significance*. Spec. Pap.—Geol. Soc. Am., 198:21–52. doi:10.1130/SPE198-p21

Carlson, R.L., and Christensen, N.I., 1977. Velocity anisotropy and physical properties of deep-sea sediments from the western South Atlantic. In Supko, P.R., Perch-Nielsen, K., et al., *Init. Repts. DSDP*, 39: Washington, DC (U.S. Govt. Printing Office), 555–559. doi:10.2973/dsdp.proc.39.124.1977

Center for Deep Earth Exploration, 2012. Guide to Scientific Analysis of Cuttings for Composition and MAD.

Cohen, K.M., Finney, S., and Gibbard, P.L., 2013. International Chronostratigraphic Chart. *International Commission on Stratigraphy*. <http://www.stratigraphy.org/ICSchart/ChronostratChart2013-01.pdf>

Droser, M.L., and Bottjer, D.J., 1986. A semiquantitative field classification of ichnofabric. *J. Sediment. Res.*, 56(4):558–559. doi:10.1306/212F89C2-2B24-11D7-8648000102C1865D

Droser, M.L., and Bottjer, D.J., 1991. Trace fossils and ichnofabric in Leg 119 cores. In Barron, J., Larsen, B., et al., *Proc. ODP, Sci. Results*, 119: College Station, TX (Ocean Drilling Program), 635–641. doi:10.2973/odp.proc.sr.119.206.1991

Expedition 314 Scientists, 2009. Expedition 314 Site C0002. In Kinoshita, M., Tobin, H., Ashi, J., Kimura, G., Lallemand, S., Sreaton, E.J., Curewitz, D., Masago, H., Moe, K.T., and the Expedition 314/315/316 Scientists, *Proc. IODP*, 314/315/316: Washington, DC (Integrated Ocean Drilling Program Management International, Inc.). doi:10.2204/iodp.proc.314315316.114.2009

Expedition 315 Scientists, 2009a. Expedition 315 methods. In Kinoshita, M., Tobin, H., Ashi, J., Kimura, G., Lallemand, S., Sreaton, E.J., Curewitz, D., Masago, H., Moe, K.T., and the Expedition 314/315/316 Scientists, *Proc. IODP*, 314/315/316: Washington, DC (Integrated Ocean Drilling Program Management International, Inc.). doi:10.2204/iodp.proc.314315316.122.2009

Expedition 315 Scientists, 2009b. Expedition 315 Site C0002. In Kinoshita, M., Tobin, H., Ashi, J., Kimura, G., Lallemand, S., Sreaton, E.J., Curewitz, D., Masago, H., Moe, K.T., and the Expedition 314/315/316 Scientists, *Proc. IODP*, 314/315/316: Washington, DC (Integrated Ocean Drilling Program Management International, Inc.). doi:10.2204/iodp.proc.314315316.124.2009

Expedition 316 Scientists, 2009. Expedition 316 methods. In Kinoshita, M., Tobin, H., Ashi, J., Kimura, G., Lallemand, S., Sreaton, E.J., Curewitz, D., Masago, H., Moe, K.T., and the Expedition 314/315/316 Scientists, *Proc. IODP*, 314/315/316: Washington, DC (Integrated Ocean Drilling Program Management International, Inc.). doi:10.2204/iodp.proc.314315316.132.2009

- Expedition 319 Scientists, 2010a. Expedition 319 summary. *In* Saffer, D., McNeill, L., Byrne, T., Araki, E., Toczko, S., Eguchi, N., Takahashi, K., and the Expedition 319 Scientists, *Proc. IODP*, 319: Tokyo (Integrated Ocean Drilling Program Management International, Inc.). [doi:10.2204/iodp.proc.319.101.2010](https://doi.org/10.2204/iodp.proc.319.101.2010)
- Expedition 319 Scientists, 2010b. Methods. *In* Saffer, D., McNeill, L., Byrne, T., Araki, E., Toczko, S., Eguchi, N., Takahashi, K., and the Expedition 319 Scientists, *Proc. IODP*, 319: Tokyo (Integrated Ocean Drilling Program Management International, Inc.). [doi:10.2204/iodp.proc.319.102.2010](https://doi.org/10.2204/iodp.proc.319.102.2010)
- Expedition 322 Scientists, 2010. Methods. *In* Saito, S., Underwood, M.B., Kubo, Y., and the Expedition 322 Scientists, *Proc. IODP*, 322: Tokyo (Integrated Ocean Drilling Program Management International, Inc.). [doi:10.2204/iodp.proc.322.102.2010](https://doi.org/10.2204/iodp.proc.322.102.2010)
- Expedition 326 Scientists, 2011. NanTroSEIZE Stage 3: plate boundary deep riser: top hole engineering. *IODP Prel. Rept.*, 326. [doi:10.2204/iodp.pr.326.2011](https://doi.org/10.2204/iodp.pr.326.2011)
- Expedition 332 Scientists, 2011. Site C0002. *In* Kopf, A., Araki, E., Toczko, S., and the Expedition 332 Scientists, *Proc. IODP*, 332: Tokyo (Integrated Ocean Drilling Program Management International, Inc.). [doi:10.2204/iodp.proc.332.104.2011](https://doi.org/10.2204/iodp.proc.332.104.2011)
- Expedition 333 Scientists, 2012. Methods. *In* Henry, P., Kanamatsu, T., Moe, K., and the Expedition 333 Scientists, *Proc. IODP*, 333: Tokyo (Integrated Ocean Drilling Program Management International, Inc.). [doi:10.2204/iodp.proc.333.102.2012](https://doi.org/10.2204/iodp.proc.333.102.2012)
- Expedition 334 Scientists, 2012. Methods. *In* Vannucchi, P., Ujiie, K., Stroncik, N., Malinverno, A., and the Expedition 334 Scientists, *Proc. IODP*, 334: Tokyo (Integrated Ocean Drilling Program Management International, Inc.). [doi:10.2204/iodp.proc.334.102.2012](https://doi.org/10.2204/iodp.proc.334.102.2012)
- Expedition 337 Scientists, 2013. Methods. *In* Inagaki, F., Hinrichs, K.-U., Kubo, Y., and the Expedition 337 Scientists, *Proc. IODP*, 337: Tokyo (Integrated Ocean Drilling Program Management International, Inc.). [doi:10.2204/iodp.proc.337.102.2013](https://doi.org/10.2204/iodp.proc.337.102.2013)
- Fisher, A.T., and Underwood, M.B., 1995. Calibration of an X-ray diffraction method to determine relative mineral abundances in bulk powders using matrix singular value decomposition: a test from the Barbados accretionary complex. *In* Shipley, T.H., Ogawa, Y., Blum, P., et al., *Proc. ODP, Init. Repts.*, 156: College Station, TX (Ocean Drilling Program), 29–37. [doi:10.2973/odp.proc.ir.156.103.1995](https://doi.org/10.2973/odp.proc.ir.156.103.1995)
- GE Healthcare, 2006. *LightSpeed Series Learning and Reference Guide-Multi Slice CT*: Waukesha, Wisconsin (GE Healthcare).
- Guéguen, Y., and Palciauskas, V., 1994. *Introduction to the Physics of Rocks*: Princeton, NJ (Princeton Univ. Press).
- Halliburton, 2012a. DGR™ (Dual Gamma Ray) Tool. (H02936-A4) http://www.halliburton.com/premium/ss/contents/Data_Sheets/web/H02936-A4.pdf
- Halliburton, 2012b. EWR®-PHASE 4™ Sensors. (H02489-A4) http://www.halliburton.com/premium/ss/contents/Data_Sheets/web/H02489-A4.pdf
- Halliburton, 2012c. M5™ Integrated LWD Service. (H05237-A4) http://www.halliburton.com/premium/ss/contents/Data_Sheets/web/H05237-A4.pdf
- Halliburton, 2012d. AFR™ Azimuthal Focused Resistivity Sensor. (H05666-A4) http://www.halliburton.com/premium/ss/contents/Data_Sheets/web/H05666-A4.pdf
- Halliburton, 2012e. Pressure-While-Drilling (PWD) Sensor. (H02986-A4) http://www.halliburton.com/premium/ss/contents/Data_Sheets/web/H02986-A4.pdf
- Halliburton, 2013. XBAT™ Azimuthal Sonic and Ultrasonic LWD Service. (H010024-A4) http://www.halliburton.com/premium/ss/contents/Data_Sheets/web/H010024-A4.pdf
- Harris, R.N., Sakaguchi, A., Petronotis, K., Baxter, A.T., Berg, R., Burkett, A., Charpentier, D., Choi, J., Diz Ferreira, P., Hamahashi, M., Hashimoto, Y., Heydolph, K., Jovane, L., Kastner, M., Kurz, W., Kutterolf, S.O., Li, Y., Malinverno, A., Martin, K.M., Millan, C., Nascimento, D.B., Saito, S., Sandoval Gutierrez, M.I., Scream, E.J., Smith-Duque, C.E., Solomon, E.A., Straub, S.M., Tanikawa, W., Torres, M.E., Uchimura, H., Vannucchi, P., Yamamoto, Y., Yan, Q., and Zhao, X., 2013. Methods. *In* Harris, R.N., Sakaguchi, A., Petronotis, K., and the Expedition 344 Scientists, *Proc. IODP*, 344: College Station, TX (Integrated Ocean Drilling Program). [doi:10.2204/iodp.proc.344.102.2013](https://doi.org/10.2204/iodp.proc.344.102.2013)
- Heard, T.G., and Pickering, K.T., 2008. Trace fossils as diagnostic indicators of deep-marine environments, middle Eocene Ainsa-Jaca Basin, Spanish Pyrenees. *Sedimentology*, 55(4):809–844. [doi:10.1111/j.1365-3091.2007.00922.x](https://doi.org/10.1111/j.1365-3091.2007.00922.x)
- Lin, W., Yeh, E.-C., Ito, H., Hirono, T., Soh, W., Wang, C.-Y., Ma, K.-E., Hung, J.-H., and Song, S.-R., 2007. Preliminary results of stress measurements using drill cores of TCDP Hole-A: an application of anelastic strain recovery method to three-dimensional in-situ stress determination. *Terr. Atmos. Oceanic Sci.*, 18(2):379. [doi:10.3319/TAO.2007.18.2.379\(TCDP\)](https://doi.org/10.3319/TAO.2007.18.2.379(TCDP))
- Lourens, L.J., Hilgen, F.J., Laskar, J., Shackleton, N.J., and Wilson, D., 2004. The Neogene period. *In* Gradstein, F.M., Ogg, J., et al. (Eds.), *A Geologic Time Scale 2004*: Cambridge, UK (Cambridge Univ. Press), 409–440.
- Maltman, A.J., Byrne, T., Karig, D.E., and Lallemand, S., 1993. Deformation at the toe of an active accretionary prism: synopsis of results from ODP Leg 131, Nankai, SW Japan. *J. Struct. Geol.*, 15(8):949–964. [doi:10.1016/0191-8141\(93\)90169-B](https://doi.org/10.1016/0191-8141(93)90169-B)
- Manheim, F.T., 1966. A hydraulic squeezer for obtaining interstitial waters from consolidated and unconsolidated sediments. *Geol. Surv. Prof. Pap. (U.S.)*, 550-C:256–261.
- Marsaglia, K., Milliken, K., and Doran, L., 2013. IODP smear slides digital reference for sediment analysis, Part 1: Methodology and atlas of siliciclastic and volcanogenic components. *IODP Tech. Note*, 1. [doi:10.2204/iodp.tn.1.2013](https://doi.org/10.2204/iodp.tn.1.2013)
- Martini, E., 1971. Standard Tertiary and Quaternary calcareous nannoplankton zonation. *In* Farinacci, A. (Ed.),

- Proc. Second Planktonic Conf. Roma 1970*: Rome (Ed. Tecnosci.), 2:739–785.
- Matsuki, K., 1991. Three-dimensional in situ stress measurement with anelastic strain recovery of a rock core. *Proc.—Int. Congr. Rock Mech.*, 7:557–560. <http://www.onepetro.org/mslib/servlet/onepetroprevue?id=ISRM-7CONGRESS-1991-110>
- Mazzullo, J., and Graham, A.G. (Eds.), 1988. Handbook for shipboard sedimentologists. *ODP Tech. Note*, 8. [doi:10.2973/odp.tn.8.1988](https://doi.org/10.2973/odp.tn.8.1988)
- Mazzullo, J.M., Meyer, A., and Kidd, R.B., 1988. New sediment classification scheme for the Ocean Drilling Program. In Mazzullo, J., and Graham, A.G. (Eds.), *Handbook for shipboard sedimentologists*. ODP Tech. Note, 8:44–67. [doi:10.2973/odp.tn.8.1988](https://doi.org/10.2973/odp.tn.8.1988)
- Mees, F., Swennen, R., Van Geet, M., and Jacobs, P., 2003. Applications of X-ray computed tomography in the geosciences. *Geol. Soc. Spec. Publ.*, 215(1):1–6. [doi:10.1144/GSL.SP.2003.215.01.01](https://doi.org/10.1144/GSL.SP.2003.215.01.01)
- Nakano, T., Nakashima, Y., Nakamura, K., and Ikeda, S., 2000. Observation and analysis of internal structure of rock using X-ray CT. *Chishitsugaku Zasshi*, 106(5):363–378.
- Noorany, I., 1984. Phase relations in marine soils. *J. Geotech. Eng.*, 110(4):539–543. [doi:10.1061/\(ASCE\)0733-9410\(1984\)110:4\(539\)](https://doi.org/10.1061/(ASCE)0733-9410(1984)110:4(539))
- Okada, H., and Bukry, D., 1980. Supplementary modification and introduction of code numbers to the low-latitude coccolith biostratigraphic zonation (Bukry, 1973; 1975). *Mar. Micropaleontol.*, 5:321–325. [doi:10.1016/0377-8398\(80\)90016-X](https://doi.org/10.1016/0377-8398(80)90016-X)
- Otani, J., Watanabe, Y., and Chevalier, B., 2010. Introduction of X-ray CT application in geotechnical engineering—theory and practice. *IOP Conf. Ser.: Mater. Sci. Eng.*, 10:012089. [doi:10.1088/1757-899X/10/1/012089](https://doi.org/10.1088/1757-899X/10/1/012089)
- Perch-Nielsen, K., 1985. Cenozoic calcareous nannofossils. In Bolli, H.M., Saunders, J.B., and Perch-Nielsen, K. (Eds.), *Plankton Stratigraphy*: Cambridge, UK (Cambridge Univ. Press), 427–554.
- Raaen, A.M., Horsrud, P., Kjørholt, H., and Økland, D., 2006. Improved routine estimation of the minimum horizontal stress component from extended leak-off tests. *Int. J. Rock Mech. Min. Sci.*, 43(1):37–48. [doi:10.1016/j.ijrmms.2005.04.005](https://doi.org/10.1016/j.ijrmms.2005.04.005)
- Raffi, I., Backman, J., Fornaciari, E., Pälke, H., Rio, D., Lourens, L., and Hilgen, F., 2006. A review of calcareous nannofossil astrobiochronology encompassing the past 25 million years. *Quat. Sci. Rev.*, 25(23–24):3113–3137. [doi:10.1016/j.quascirev.2006.07.007](https://doi.org/10.1016/j.quascirev.2006.07.007)
- Richter, C., Acton, G., Endris, C., and Radsted, M., 2007. Handbook for shipboard paleomagnetists. *ODP Tech. Note*, 34. [doi:10.2973/odp.tn.34.2007](https://doi.org/10.2973/odp.tn.34.2007)
- Rothwell, R.G., 1989. *Minerals and Mineraloids in Marine Sediments: An Optical Identification Guide*: London (Elsevier).
- Saffer, D., McNeill, L., Byrne, T., Araki, E., Toczko, S., Eguichi, N., Takahashi, K., and the Expedition 319 Scientists, 2010. *Proc. IODP*, 319: Tokyo (Integrated Ocean Drilling Program management International, Inc.). [doi:10.2204/iodp.proc.319.2010](https://doi.org/10.2204/iodp.proc.319.2010)
- Sakamoto, T., Kuroki, K., Sugawara, T., Aoike, K., Iijima, K., and Sugisaki, S., 2006. Non-destructive X-ray fluorescence (XRF) core-imaging scanner, TATSCAN-F2. *Sci. Drill.*, 2:37–39. http://www.iodp.org/iodp_journals/9_Non_Destructive_X_Ray_SD2.pdf
- Shepard, F.P., 1954. Nomenclature based on sand-silt-clay ratios. *J. Sediment. Res.*, 24(3):151–158. [doi:10.1306/D4269774-2B26-11D7-8648000102C1865D](https://doi.org/10.1306/D4269774-2B26-11D7-8648000102C1865D)
- Shipboard Scientific Party, 1991. Explanatory notes. In Taira, A., Hill, I., Firth, J.V., et al., *Proc. ODP, Init. Repts.*, 131: College Station, TX (Ocean Drilling Program), 25–60. [doi:10.2973/odp.proc.ir.131.104.1991](https://doi.org/10.2973/odp.proc.ir.131.104.1991)
- Strasser, M., Dugan, B., Kanagawa, K., Moore, G.F., Toczko, S., Maeda, L., Kido, Y., Moe, K.T., Sanada, Y., Esteban, L., Fabbri, O., Geersen, J., Hammerschmidt, S., Hayashi, H., Heirman, K., Hüpers, A., Jurado Rodriguez, M.J., Kameo, K., Kanamatsu, T., Kitajima, H., Masuda, H., Milliken, K., Mishra, R., Motoyama, I., Olcott, K., Oohashi, K., Pickering, K.T., Ramirez, S.G., Rashid, H., Sawyer, D., Schleicher, A., Shan, Y., Skarbek, R., Song, I., Takeshita, T., Toki, T., Tudge, J., Webb, S., Wilson, D.J., Wu, H.-Y., and Yamaguchi, A., 2014a. Methods. In Strasser, M., Dugan, B., Kanagawa, K., Moore, G.F., Toczko, S., Maeda, L., and the Expedition 338 Scientists, *Proc. IODP*, 338: Yokohama (Integrated Ocean Drilling Program). [doi:10.2204/iodp.proc.338.102.2014](https://doi.org/10.2204/iodp.proc.338.102.2014)
- Strasser, M., Dugan, B., Kanagawa, K., Moore, G.F., Toczko, S., Maeda, L., Kido, Y., Moe, K.T., Sanada, Y., Esteban, L., Fabbri, O., Geersen, J., Hammerschmidt, S., Hayashi, H., Heirman, K., Hüpers, A., Jurado Rodriguez, M.J., Kameo, K., Kanamatsu, T., Kitajima, H., Masuda, H., Milliken, K., Mishra, R., Motoyama, I., Olcott, K., Oohashi, K., Pickering, K.T., Ramirez, S.G., Rashid, H., Sawyer, D., Schleicher, A., Shan, Y., Skarbek, R., Song, I., Takeshita, T., Toki, T., Tudge, J., Webb, S., Wilson, D.J., Wu, H.-Y., and Yamaguchi, A., 2014b. Site C0002. In Strasser, M., Dugan, B., Kanagawa, K., Moore, G.F., Toczko, S., Maeda, L., and the Expedition 338 Scientists, *Proc. IODP*, 338: Yokohama (Integrated Ocean Drilling Program). [doi:10.2204/iodp.proc.338.103.2014](https://doi.org/10.2204/iodp.proc.338.103.2014)
- Stuchly, M.A., and Stuchly, S.S., 1980. Coaxial line reflection methods for measuring dielectric properties of biological substances at radio and microwave frequencies—a review. *IEEE Trans. Instrum. Meas.*, 29(3):176–183. [doi:10.1109/TIM.1980.4314902](https://doi.org/10.1109/TIM.1980.4314902)
- Su, X., 1996. Development of late Tertiary and Quaternary coccolith assemblages in the northeast Atlantic. *GEO-MAR-Rep.*, 48.
- Tauxe, L., Tucker, P., Peterson, N.P., and LaBrecque, J.L., 1984. Magnetostratigraphy of Leg 73 sediments. In Hsü, K.J., LaBrecque, J.L., et al., *Init. Repts. DSDP*, 73: Washington, DC (U.S. Govt. Printing Office), 609–621. [doi:10.2973/dsdp.proc.73.123.1984](https://doi.org/10.2973/dsdp.proc.73.123.1984)
- Tobin, H., Hirose, T., Saffer, D., Toczko, S., Maeda, L., Kubo, Y., Boston, B., Broderick, A., Brown, K., Crespo-Blanc, A., Even, E., Fuchida, S., Fukuchi, R., Hammerschmidt, S., Henry, P., Josh, M., Jurado, M.J., Kitajima, H., Kitamura, M., Maia, A., Otsubo, M., Sample, J., Schleicher, A., Sone, H., Song, C., Valdez, R., Yamamoto, Y., Yang, K., Sanada, Y., Kido, Y., and Hamada, Y., 2015. Site

- C0002. In Tobin, H., Hirose, T., Saffer, D., Toczko, S., Maeda, L., Kubo, Y., and the Expedition 348 Scientists, *Proc. IODP*, 348: College Station, TX (Integrated Ocean Drilling Program). doi:10.2204/iodp.proc.348.103.2015
- Underwood, M.B., Basu, N., Steurer, J., and Udas, S., 2003. Data report: normalization factors for semiquantitative X-ray diffraction analysis, with application to DSDP Site 297, Shikoku Basin. In Mikada, H., Moore, G.F., Taira, A., Becker, K., Moore, J.C., and Klaus, A. (Eds.), *Proc. ODP, Sci. Results*, 190/196: College Station, TX (Ocean Drilling Program), 1–28. doi:10.2973/odp.proc.sr.190196.203.2003
- Underwood, M.B., Saito, S., Kubo, Y., and the Expedition 322 Scientists, 2009. NanTroSEIZE Stage 2: subduction inputs. *IODP Prel. Rept.*, 322. doi:10.2204/iodp.pr.322.2009
- Vacquier, V., 1985. The measurement of thermal conductivity of solids with a transient linear heat source on the plane surface of a poorly conducting body. *Earth Planet. Sci. Lett.*, 74(2–3):275–279. doi:10.1016/0012-821X(85)90027-5
- Von Hippel, A.R., 1954. *Dielectric Materials and Applications*: Cambridge, MA (MIT Press).
- Wheat, C.G., Boulègue, J., and Mottl, M.J., 1994. A technique for obtaining pore water chemical composition from indurated and hydrothermally altered sediment and basalt: the ground rock interstitial normative determination (GRIND). In Mottl, M.J., Davis, E.E., Fisher, A.T., and Slack, J.F. (Eds.), *Proc. ODP, Sci. Results*, 139: College Station, TX (Ocean Drilling Program), 429–437. doi:10.2973/odp.proc.sr.139.234.1994
- Wiersberg, T., and Erzinger, J., 2007. A helium isotope cross-section study through the San Andreas Fault at seismogenic depths. *Geochem., Geophys., Geosyst.*, 8(1):Q01002. doi:10.1029/2006GC001388
- Young, J.R., 1998. Neogene. In Bown, P.R. (Ed.), *Calcareous Nannofossil Biostratigraphy*: Dordrecht, The Netherlands (Kluwer Academic Publ.), 225–265.
- Zoback, M.D., 2007. *Reservoir Geomechanics*: Cambridge, UK (Cambridge Univ. Press).

Publication: 29 January 2015
MS 348-102

Figure F1. Cuttings analysis flow, Hole C0002P. NGR = natural gamma radiation, MAD = moisture and density, Mag. Sus. = magnetic susceptibility, XRF = X-ray fluorescence, XRD = X-ray diffraction, CA = carbonate analyzer, EA = elemental analyzer.

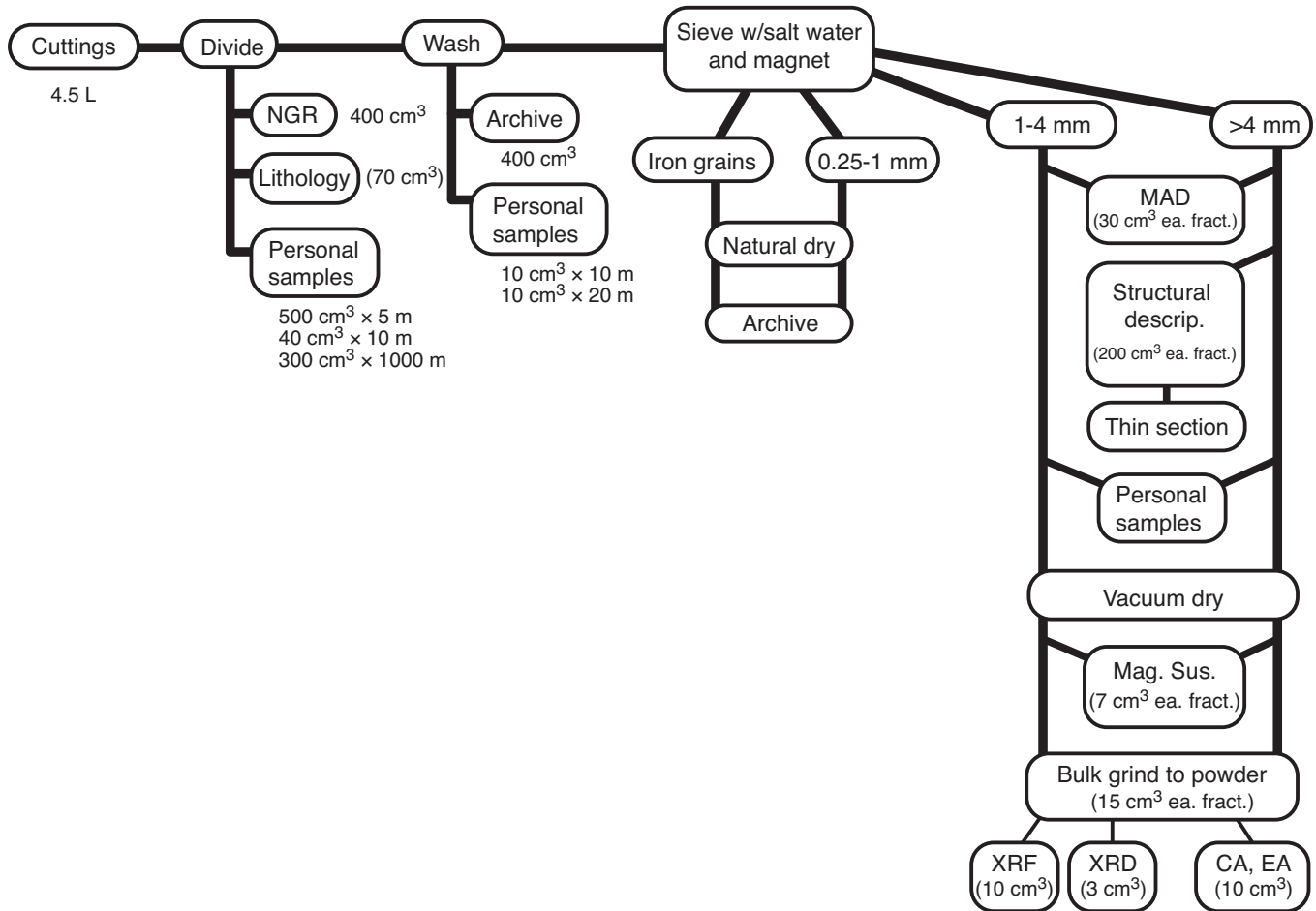


Figure F2. Representative cuttings. **A.** Drilling-induced cohesive aggregate of clay-sized fraction easily disaggregated in water (Sample 338-C0002F-289-SMW; >4 mm; 2004.5 mbsf). **B.** Pillowed cutting (Sample 41-SMW; >4 mm; 1010.5 mbsf). **C.** Intact cuttings (Sample 348-C0002P-77-SMW; handpicked; 2185.5 mbsf).

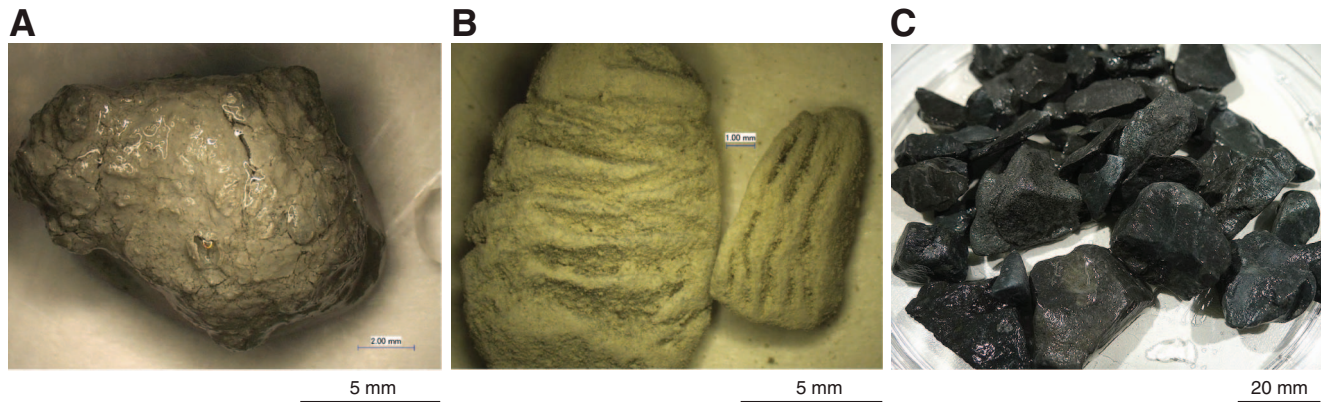


Figure F3. Core analysis flow, Expedition 348. GC-FID = gas chromatograph–flame ionization detector, HC = hydrocarbon. IW = interstitial water, ASR = anelastic strain recovery, RMS = routine microbiology sample, CT = computed tomography, WR = whole round, MSCL-W = whole-round multisensor core logger, GRA = gamma ray attenuation, MS = magnetic susceptibility, PWV = P-wave velocity, NCR = noncontact electrical resistivity, NGR = natural gamma radiation, MSCL-I = photo image logger, VCD = visual core description, MSCL-C = color spectroscopy logger, SRM = superconducting rock magnetometer, MAD = moisture and density, SEM-EDS = scanning electron microscope–energy dispersive spectrometry. GRIND = ground rock interstitial normative determination. ICP-AES = inductively coupled plasma–atomic emission spectroscopy, ICP-MS = inductively coupled plasma–mass spectrometry, IC = ion chromatography, UV = ultraviolet visible spectrophotometry. XRD = X-ray diffraction, XRF = X-ray fluorescence, CA = carbonate analyzer, EA = elemental analyzer.

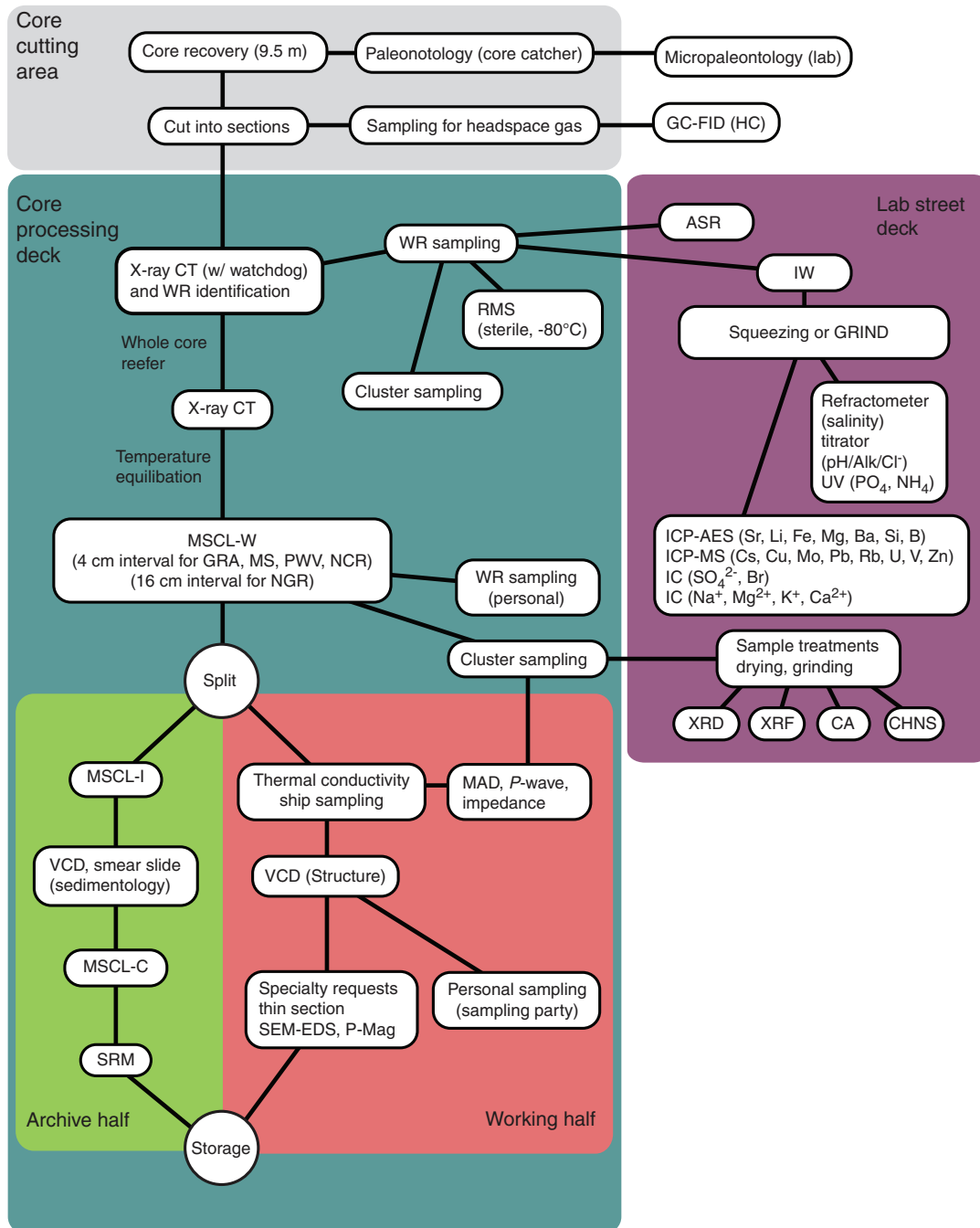


Figure F4. Graphic patterns and symbols used for visual core descriptions, Expedition 348 (see also Strasser et al., 2014a).




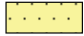
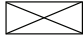




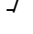















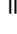





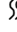
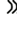
Lithology		Shipboard samples	
	Silty claystone	CARB	Inorganic carbon
	Siltstone	HS	Headspace gas analysis
	Silty sandstone	IMP	Resistivity/Impedence
	Sandstone	IW	Interstitial water
	Extracted core (sample)	IWP	Interstitial water/Plastic
Deformation structure		PAL	Paleontology
	Vein	PMAG	Paleomagnetism
	Normal fault	PP	Moisture and density
	Reverse fault	PWVD	<i>P</i> -wave velocity
	Deformation band	SEM	Images for paleontology
	Shear fracture	SS	Smear slide
	Slickenline	TSS	Thin section slide
Core disturbance (drilling and/or splitting)		XRD	X-ray diffraction
	Slightly disturbed	XRF	X-ray fluorescence
	Moderately disturbed	LCL	Liquid from core liner
	Heavily disturbed	RMS	Routine M-biological sample
	Soupy	GW	Interstitial water extracted by GRIND method
	Biscuit	HSECD	PFC contamination check
	Slightly fractured	HSECDM	PFC contamination check/Mud
	Moderately fractured	IWT	IW/TRIMMINGS small
	Highly fractured	MWIC	Mud water without acid
	Drilling breccia	MWICH	Mud water after alkaline measurement
	Gas expansion	MWICP	Mud water with acid
		MWP	Mud water/Plastic
		VCD	Visual core description
Sedimentary structure			
	Fining upward		
	Planar bedding (lamination)		
	Wavy bedding		
	High-angle bedding		
	Vertical bedding		
Lithologic accessories			
	Py Pyritized grain		
	Black band		
	Color banding		
	Mottled		
Bioturbation - Ichnofossil			
	Slight bioturbation		
	Moderate bioturbation		
	Heavy bioturbation		

Figure F5. Graphic patterns and symbols used for descriptions of cuttings, Expedition 348 (see also Strasser et al., 2014a).

Macroscopic cuttings

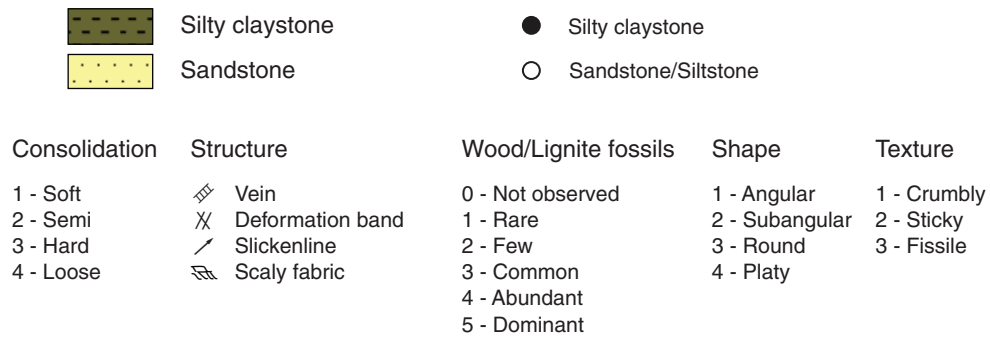


Figure F6. Examples of X-ray diffractograms for mixtures of standard minerals showing the positions of diagnostic peaks used to calculate relative mineral abundance, Expedition 348. Green line represents baseline subtraction.

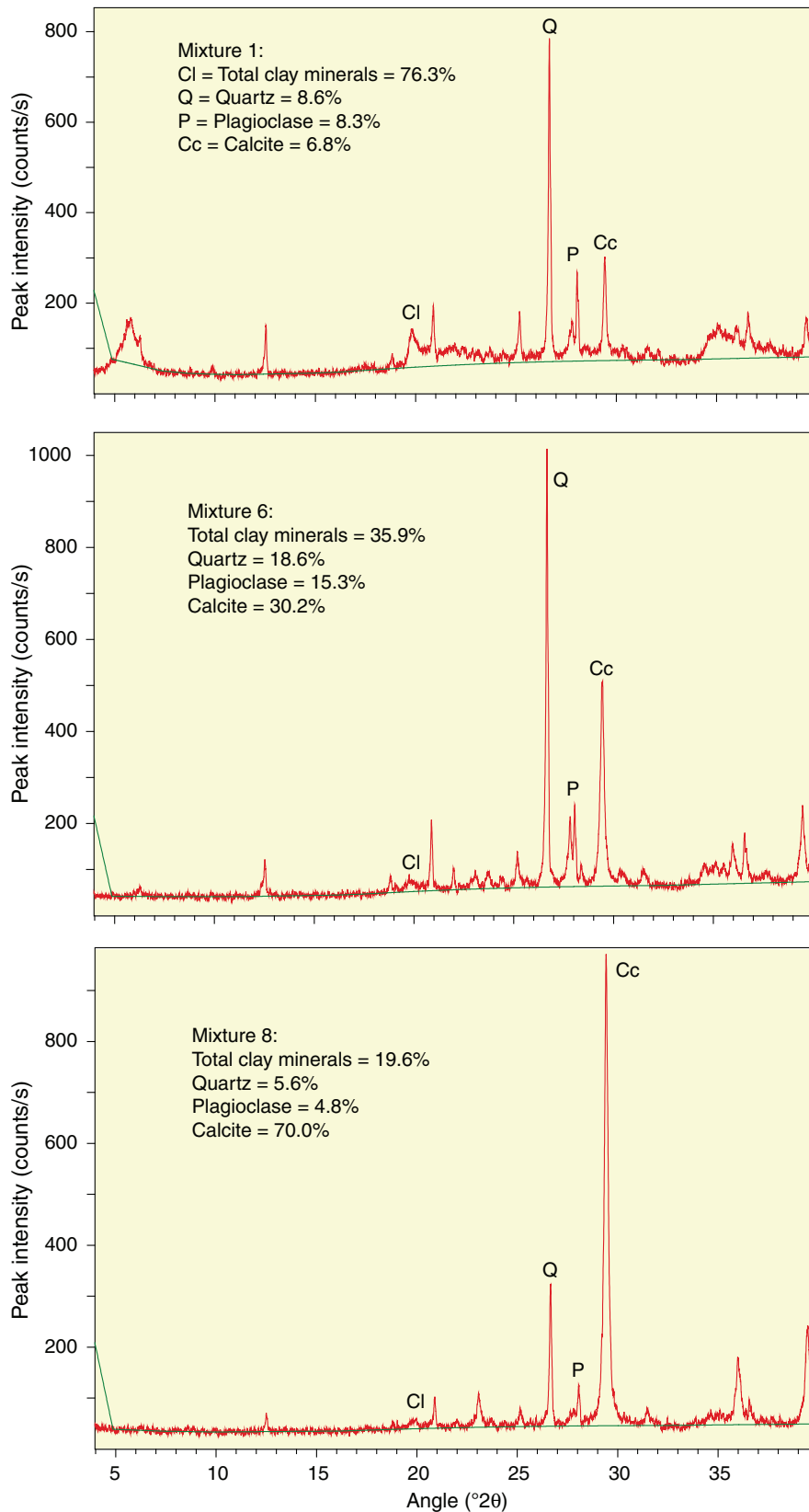




Figure F7. Example of log sheet (structural geology observation sheet) used to record structural observations and measurements from the core working half of split cores, Expedition 348.

CHIKYU Operation

Last Update 3/June/2011

Structural Geology Observation Sheet

No. _____

Exp. : _____ Site : _____ Hole : _____ Core : _____ Observer : _____ Summary: _____

Section No.	Structure ID	Top of Struct	Bottom of Struct	ave. depth	Thickness of Struct	Core face app. Dip		2nd app. Dip		Striation on surface		Coherent interval (for P-mag)		P-mag pole		Notes	
						az.	dip	az.	dip	rake (< 90)	from (+, - 90 or 270) * Top ---"1" Bottom ---"1"	top	bottom	az./trend	dip		

Figure F8. Modified protractor used to measure apparent dip angles, bearings, plunge angles, and rakes of planar and linear features in the working half of split cores, Expedition 348.

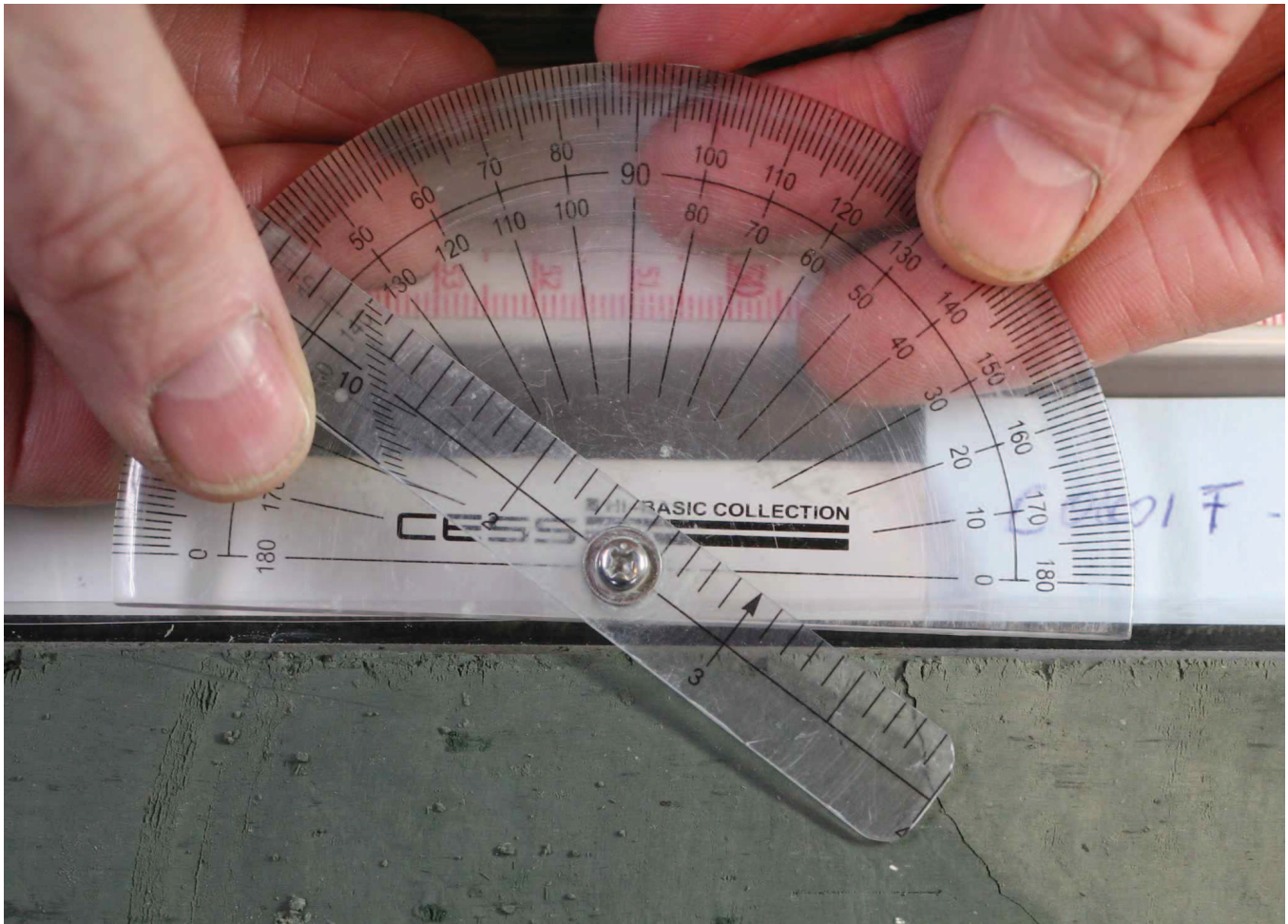


Figure F9. Core coordinate system with x -, y -, and z -axes used for orientation data measurements, Expedition 348.

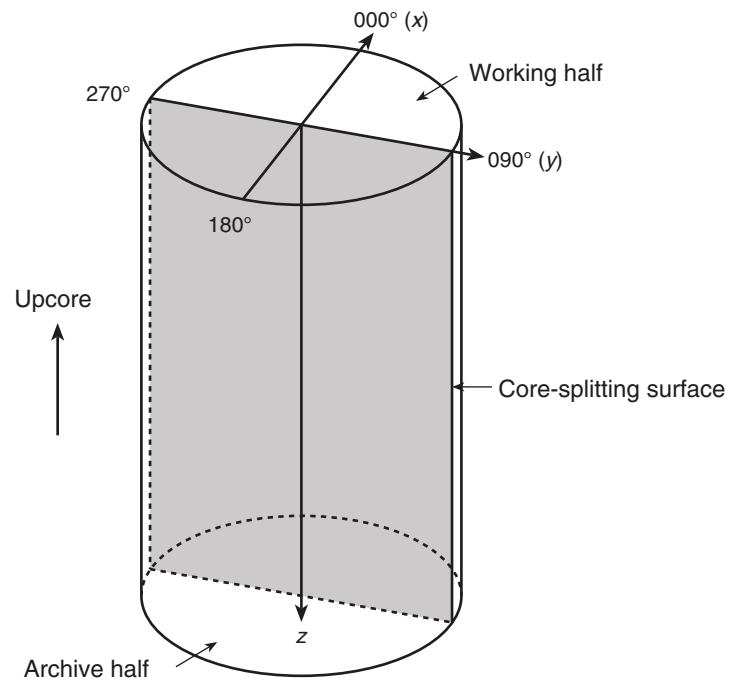


Figure F10. Determination of the orientation of a geological plane (shaded) from two auxiliary measurements. The first auxiliary measurement is done on the flat-lying split core surface and consists of measuring the bearing α_1 and the plunge angle β_1 of the trace of the plane on the split surface. The second auxiliary measurement is done on a surface perpendicular to the flat-lying split core surface and contains the core axis and consists of measuring the bearing α_2 and the plunge angle β_2 of the trace of the plane on the surface.

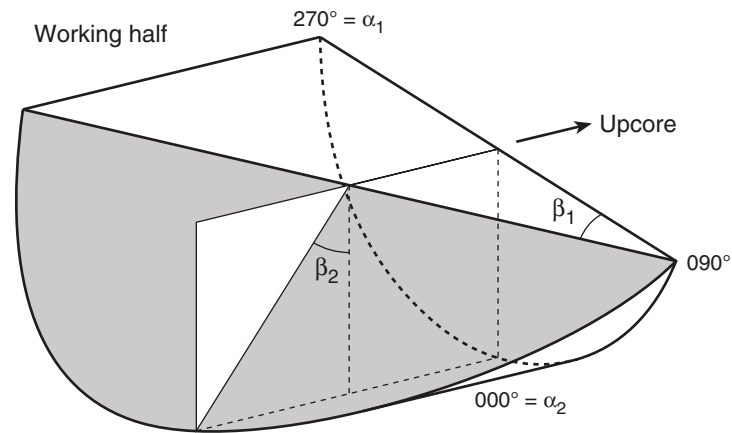


Figure F11. Rake (ϕ_a) measurement of slickenlines on a fault surface. In this example, the slickenlines rake from the azimuth of the plane that points in the western (270°) quadrant in the core reference frame.

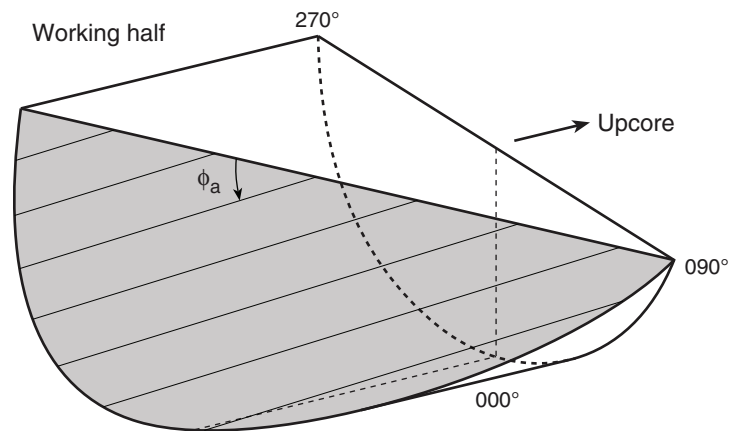


Figure F12. Example of the spreadsheet used for recording and calculating orientation data, Expedition 348.

C00018 depth	hole ID	core ID	sect	structure ID	top of struct	bottom of struct	average depth	core face app. dip		2nd app. dip		striation on surface		plane-normal orientation				plane orientation (RHR)			fault			coherent interval (for P-mag)		P-mag pole		corrected orientation (RHR)			fault		notes		
								az	dip	az	dip	rake	from	l	m	n	az	dip	dip dir	strike	dip	csf rake	str rake	slip sense	top	bottom	Dec	Inc	dip dir	strike	dip	str rake		slip sense	
1.86	A	1H	3	bedding	44.0	45.0	44.5	90	14	332	0	-0.11	0.21	-0.86	62	-74	62	332	16	0	140	288.861	53.662	133	43	16									
29.52	A	4H	3	bedding	86.0	87.0	86.5	270	1	180	9	-0.16	-0.02	-0.99	186	-81	186	96	9	0	92	37.8078	54.335	148	58	9									
54.33	A	7H	1	dewatering structure?	14.0	21.0	17.5																												
64.30	A	7H	11	fault	135.0	137.0	136	90	38	59	0	-0.53	0.32	-0.41	149	-33	149	59	57	17	144	267.54	65.815	241	151	57									
64.27	A	8H	2	bedding	35.0	37.0	36	90	27	56	0	-0.38	0.25	-0.50	146	-48	146	56	42	0	98	10.1184	45.135	136	46	42									
65.97	A	8H	3	bedding	59.0	60.0	59.5	90	3	323	0	0.03	0.04	-0.80	53	-86	53	323	4	52	115	10.1184	45.135	43	313	4									
67.15	A	8H	4	disturbed layers	50.0	75.0	62.5																												
69.47	A	8H	8	fault	8.0	21.0	14.5	270	66	325	0	0.52	0.75	0.33	55	20	235	145	70	0	147	10.1184	45.135	225	135	70							offset = 8 mm		
73.51	A	8H	10	fault	118.0	129.0	123.5	90	66	319	0	0.60	0.69	-0.31	49	-19	49	319	71	108	148	10.1184	45.135	39	309	71							offset = 8.5mm		
105.56	A	12H	7	fault	22.0	26.0	24	90	37	287	0	0.58	0.18	-0.23	17	-21	17	287	69	0	140	230.055	57.395	147	57	69									
106.10	A	12H	7	bedding	77.0	78.0	77.5	90	1	0	0	0.00	0.02	-1.00	90	-89	90	0	1	0	140	230.055	57.395	220	130	1									
110.72	A	13H	4	fault	0.0	10.0	5	270	64	337	0	0.35	0.83	0.40	67	24	247	157	66	0	54	67.1364	43.259	180	90	66								syn-sedimentary	
112.32	A	13H	5	bedding	23.0	24.0	23.5	270	2	62	0	-0.03	0.02	0.47	152	86	332	242	4	15	46	67.1364	43.259	265	175	4									
114.53	A	13H	9	fault	6.0	14.0	10	90	52	16	0	-0.22	0.76	-0.59	106	-37	106	16	53	0	89	67.1364	43.259	39	309	53								offset = 20 mm	
117.65	A	13H	11	fault	35.0	48.0	41.5	270	62	20	0	-0.30	0.83	0.44	110	27	290	200	63	0	49	67.1364	43.259	223	133	63								offset = 28 mm	
119.29	A	13H	13	fault	130.0	137.0	133.5	270	63	150	0	-0.45	-0.77	-0.39	240	-24	240	150	66	0	138	67.1364	43.259	173	83	66									
141.96	A	16H	10	fault	17.0	26.0	21.5	90	50	180	45	0.45	-0.54	0.45	310	33	130	40	57	0	76	350.371	-70.37	320	230	57									
143.09	A	16H	11	fault	54.0	60.0	57	90	40	312	0	0.48	0.43	-0.51	42	-39	42	312	51	12	122	350.371	-70.37	232	142	51									
141.09	A	16H	4	fault (not healed)	79.0	88.0	83.5	90	57	32	0	-0.44	0.71	-0.46	122	-29	122	32	61	0	149	350.371	-70.37	312	222	61									
141.57	A	16H	4	fault (not healed)	129.0	135.0	132	90	56	35	0	-0.48	0.68	-0.46	125	-29	125	35	61	0	149	350.371	-70.37	315	225	61									
142.91	A	16H	11	fault (not healed)	35.0	42.0	39	90	46	310	0	0.55	0.46	-0.45	40	-32	40	310	58	12	121	350.371	-70.37	230	140	58									
143.09	A	16H	11	fault (not healed)	54.0	60.0	57	90	40	312	0	0.48	0.43	-0.51	42	-39	42	312	51	12	121	350.371	-70.37	232	142	51									
145.38	A	17H	1	bedding	72.0	73.0	72.5	90	21	338	0	0.13	0.33	-0.87	68	-68	68	338	22	0	82	345.925	-68.26	262	172	22									
145.18	A	17H	1	shear zone	49.0	57.0	53	90	51	320	0	0.50	0.60	-0.48	50	-32	50	320	58	34	143	345.925	-68.26	244	154	58									
149.60	A	17H	4	shear zone	69.0	75.0	72	270	63	45	0	-0.63	0.63	0.32	135	20	315	225	70	0	141	345.925	-68.26	149	59	70									
151.54	A	17H	7	web structure	10.0	52.0	31																												
152.27	A	17H	7	shear zone	103.0	105.0	104	270	17	80	0	-0.29	0.05	0.17	170	30	350	260	60	0	143	345.925	-68.26	184	94	60									
152.51	A	17H	7	shear zone	123.0	133.0	128	90	66	308	0	0.72	0.56	-0.25	38	-15	38	308	75	0	143	345.925	-68.26	232	142	75									

±90 ±1, 90 or 270
top->"1"
bottom->"-1"

Red means uncertain data



Figure F13. Late Cenozoic magnetostratigraphic and biostratigraphic events used during Expedition 348, modified after Strasser et al. (2014a). FO = first occurrence, LO = last occurrence, X = crossover. Polarity: black = normal, white = reversed.

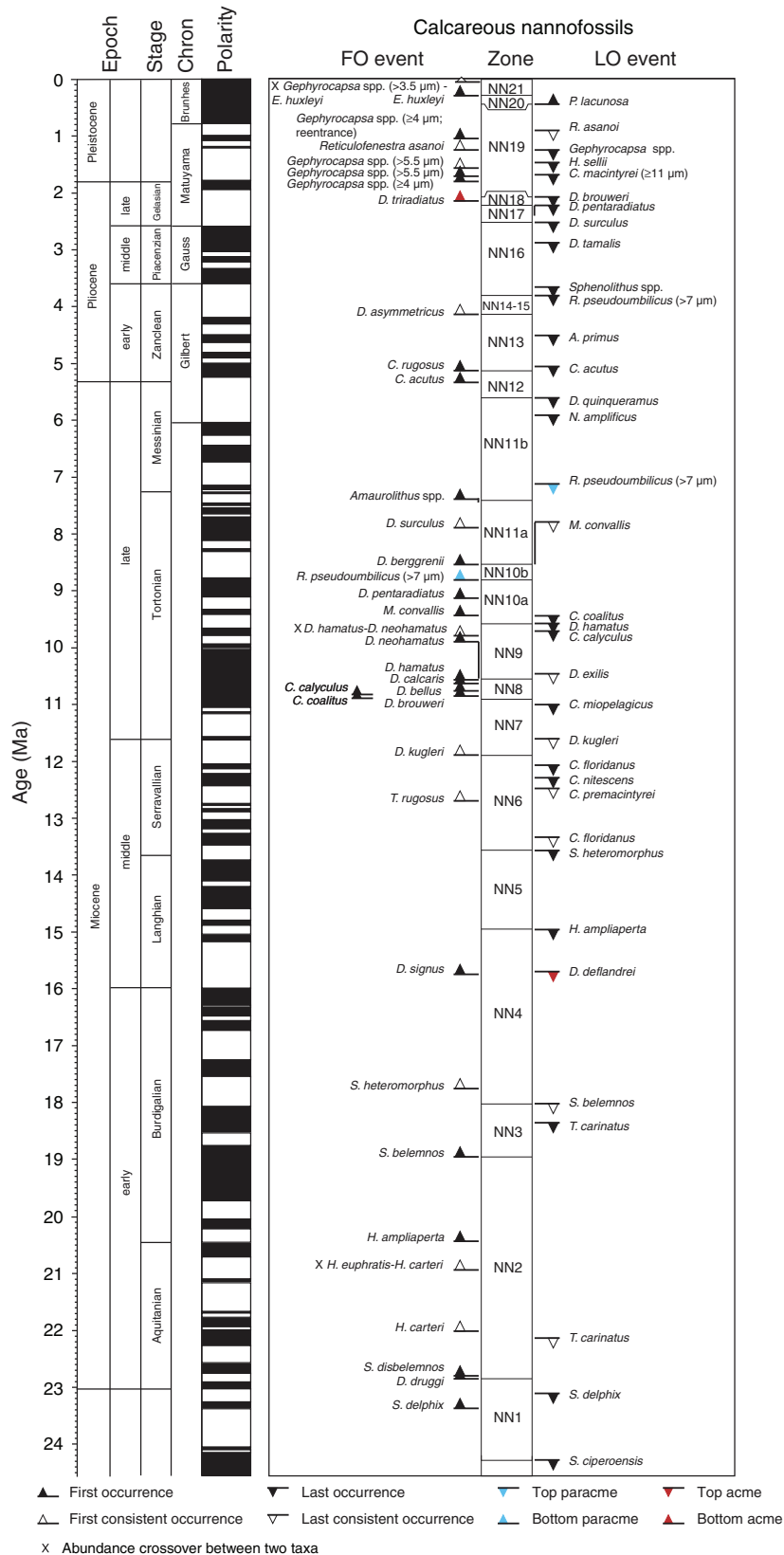


Figure F14. Orientation system used during Expedition 348 and coordinates for superconducting rock magnetometer (modified from Richter et al., 2007). SQUID = superconducting quantum interference device.

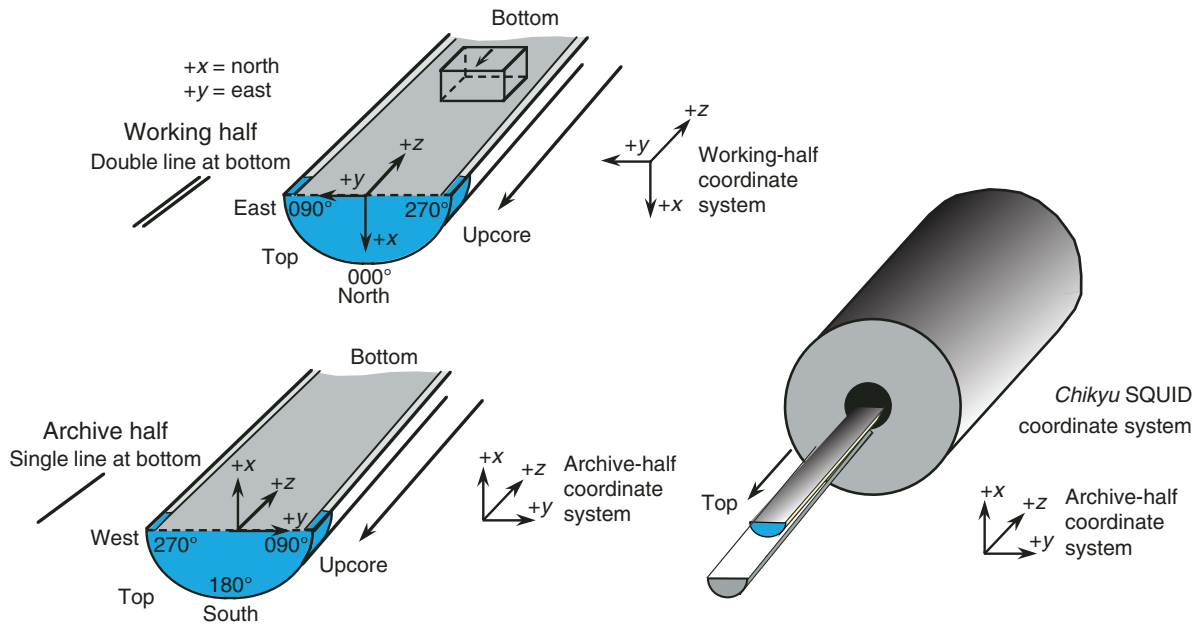


Figure F15. The two small Manheim squeezer assemblies used for the first time during Expedition 348. Inner diameter of jacket is 55 mm. **A.** Squeezer with water-sampling port in the base. **B.** Squeezer with two water-sampling ports.

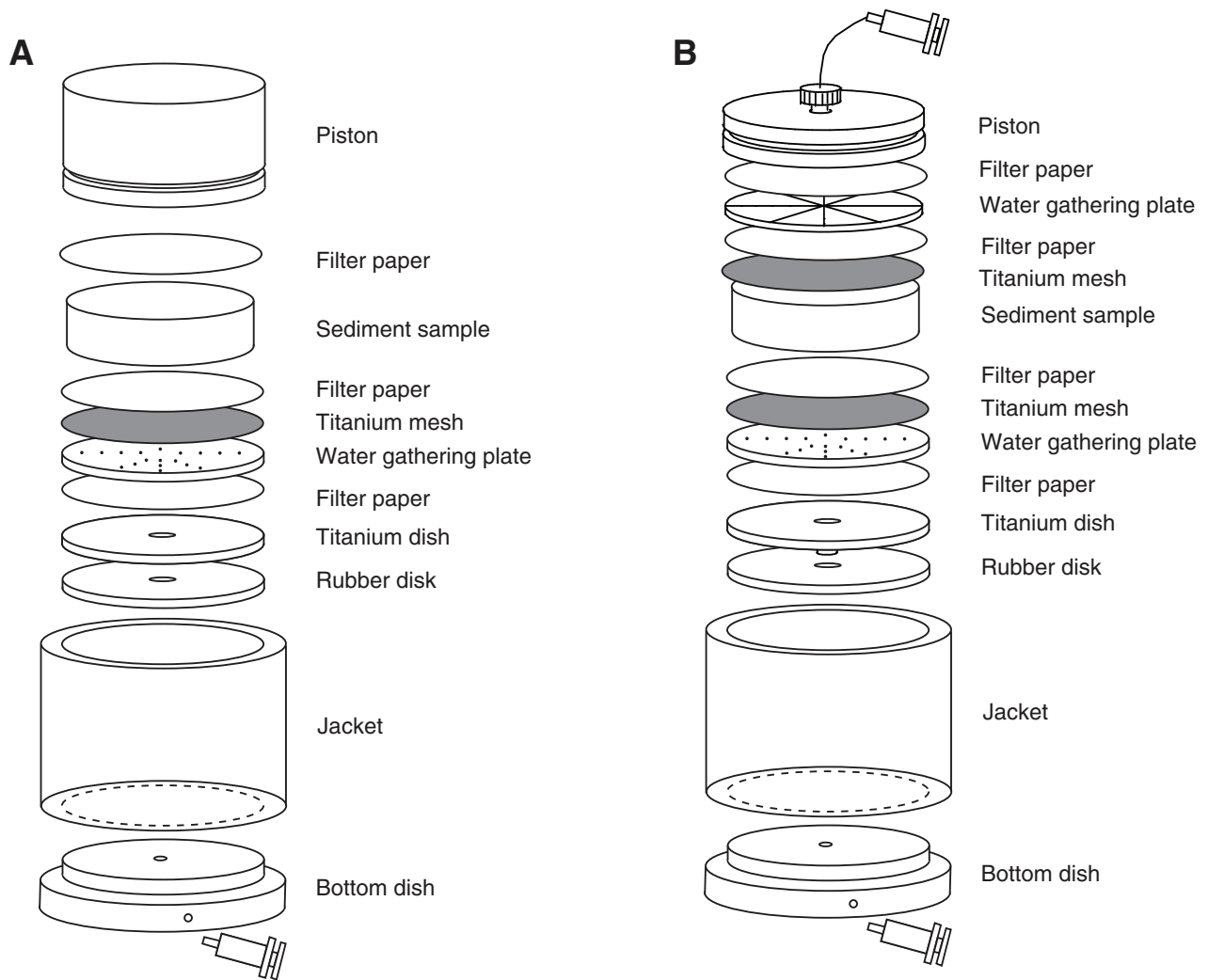


Figure F16. Mud extraction system, third-party sampling tools, and mud-gas monitoring laboratory (modified from Expedition 319 Scientists, 2010b; Expedition 337 Scientists, 2013; Strasser et al., 2014a). **A.** The gas-enriched drilling mud is transported upward and enters the main mud flow line, where it passes a flow splitter. One flow branch leads to a degasser, where the gas is extracted and forwarded to a mud gas monitoring laboratory (position D1). The position of the degasser was changed during the cruise; thus, for the depth interval from 2330 to 3058 mbsf, the degasser was in the mud trough (position D2). The mud is then forwarded to the shaker screens, where cuttings are removed. This is followed by transport of the drilling mud to and storage in mud tanks, where it can be pumped down again. **B.** After degassing, the gas is directed through an IsoTube sampling system to the dehydration module through a third-party sampling line, which consisted of glass flasks and copper tubes. After the gas is dried and cleaned, another IsoTube sampling system can collect gas samples for later analyses; a gas chromatograph with flame ionization detector (FID), quadrupole mass spectrometer, radon detector, and methane carbon isotope analyzer are connected to the pipeline to permit real-time monitoring of gas and methane carbon isotope composition.

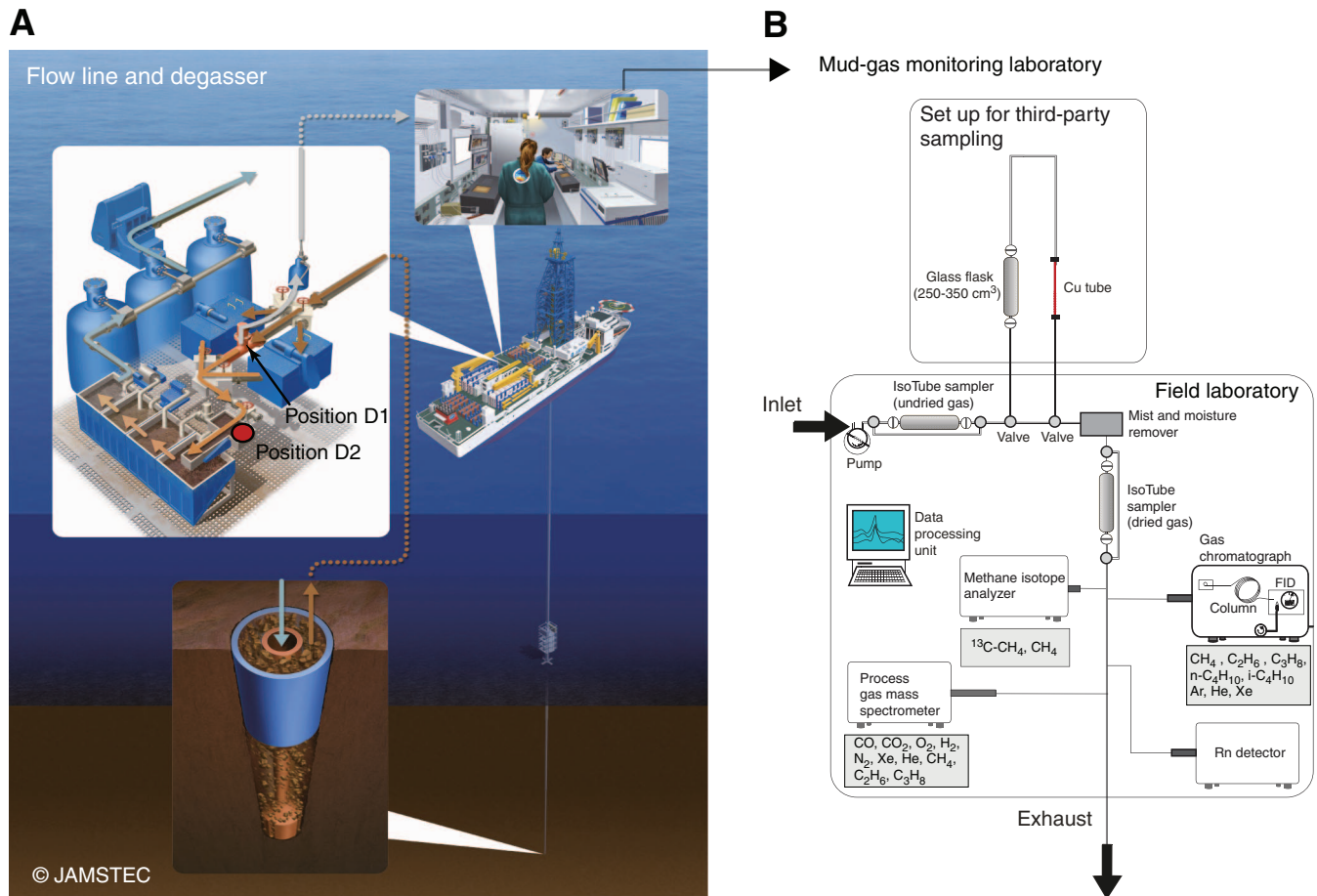


Figure F17. Overview of background concentrations of hydrocarbon gases in the drilling mud, Expedition 348.

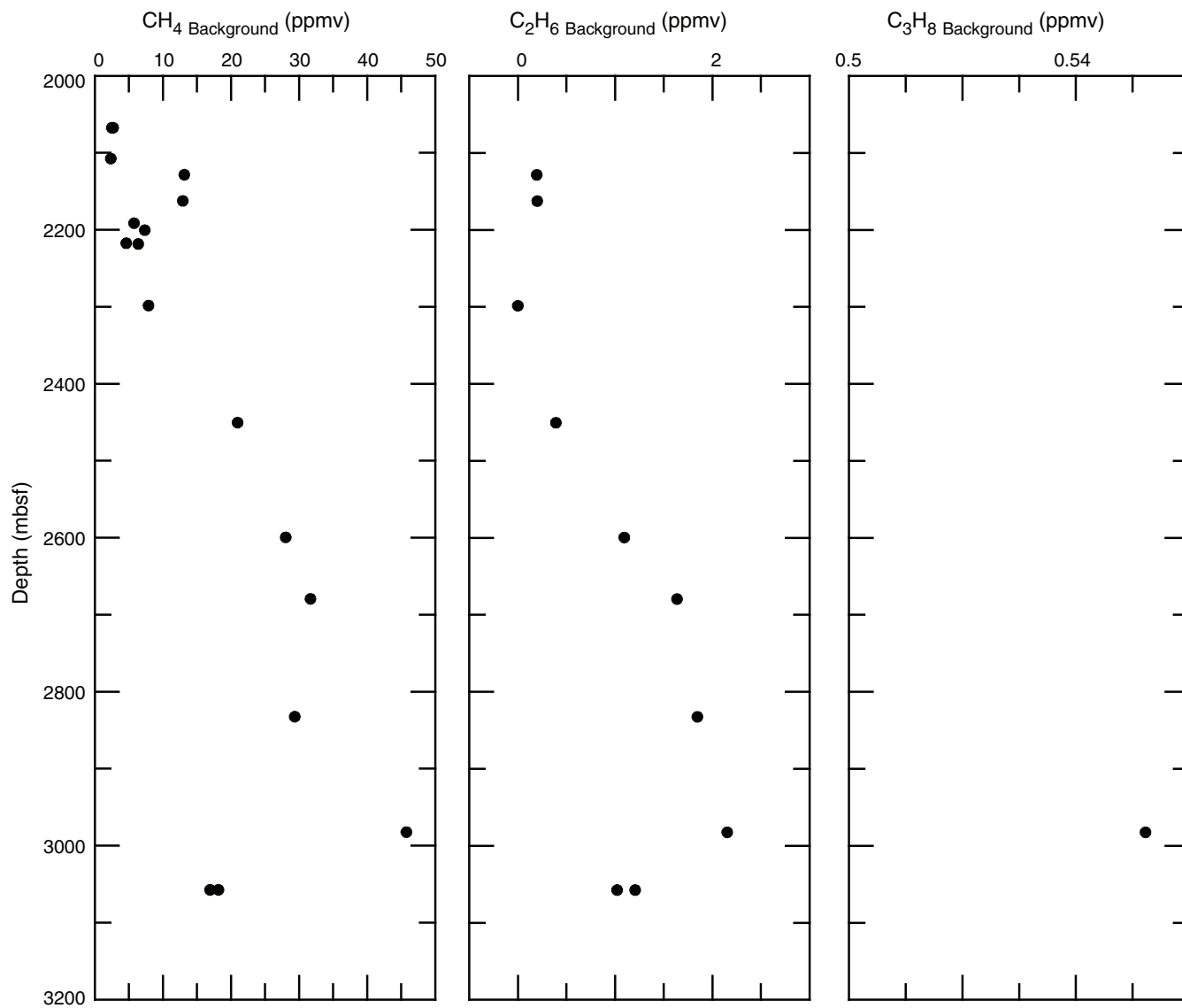


Figure F18. End-loaded transmission line probe, Expedition 348. Small quantities of sample material are prepared into pastes, which are pressed against the flat measuring surface.



Figure F19. Two-dimensional measurement system for the elliptical section of whole-round cores, Expedition 348.

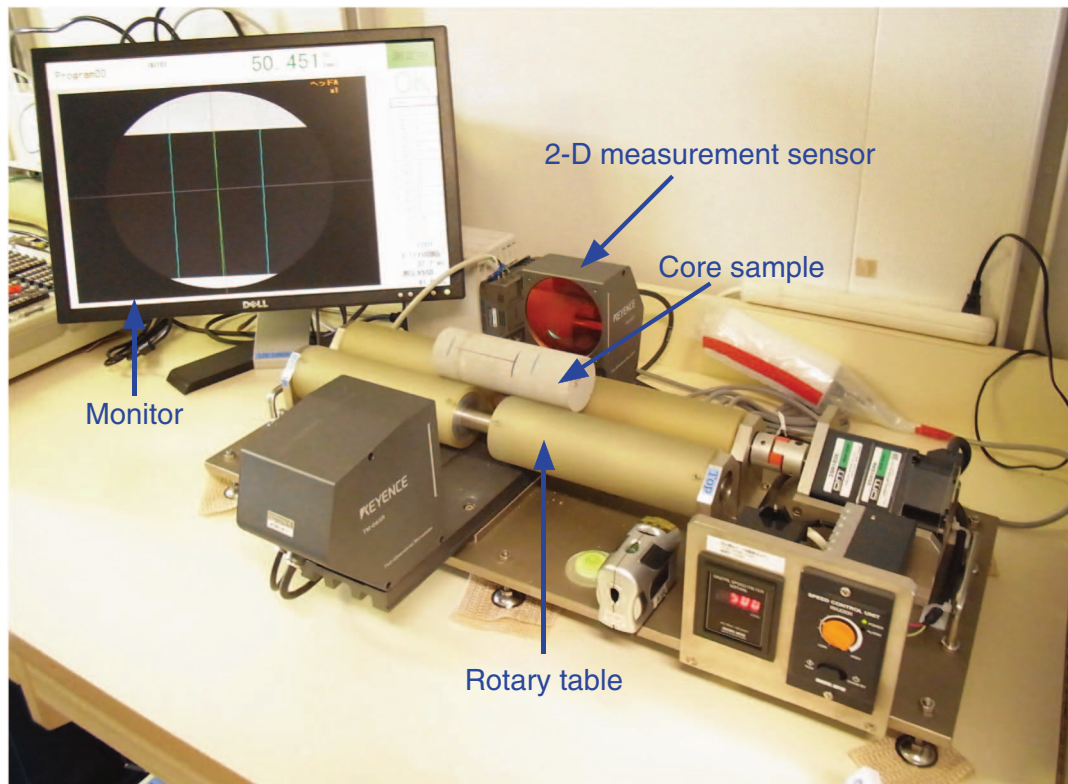


Figure F20. Procedures and equipment for anelastic strain recovery measurement (ASR), Expedition 348. **A.** A total of 18 strain gauges were put on the core sample. **B.** Core samples were double-bagged. This photo was taken after it was placed in a plastic bag. The bagged sample was subsequently placed in an aluminum bag. **C.** Instruments for ASR measurement. UPS = uninterruptible power supply.

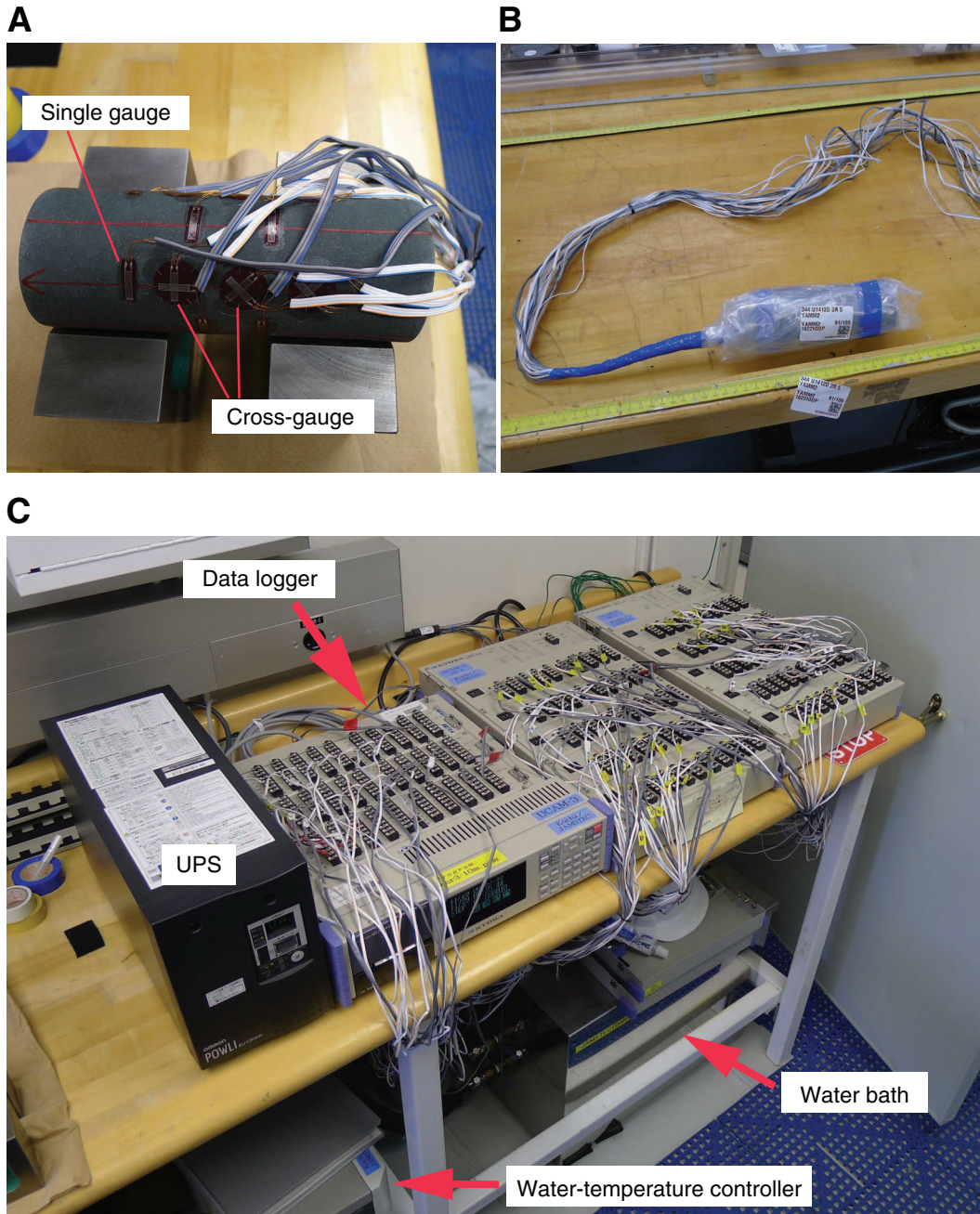


Figure F21. Measurement-while-drilling/logging-while-drilling (MWD/LWD) bottom-hole assembly 17 inch configurations, Hole C0002N. PDC = polycrystalline diamond compact. **A.** Run 1. (Continued on next page.)

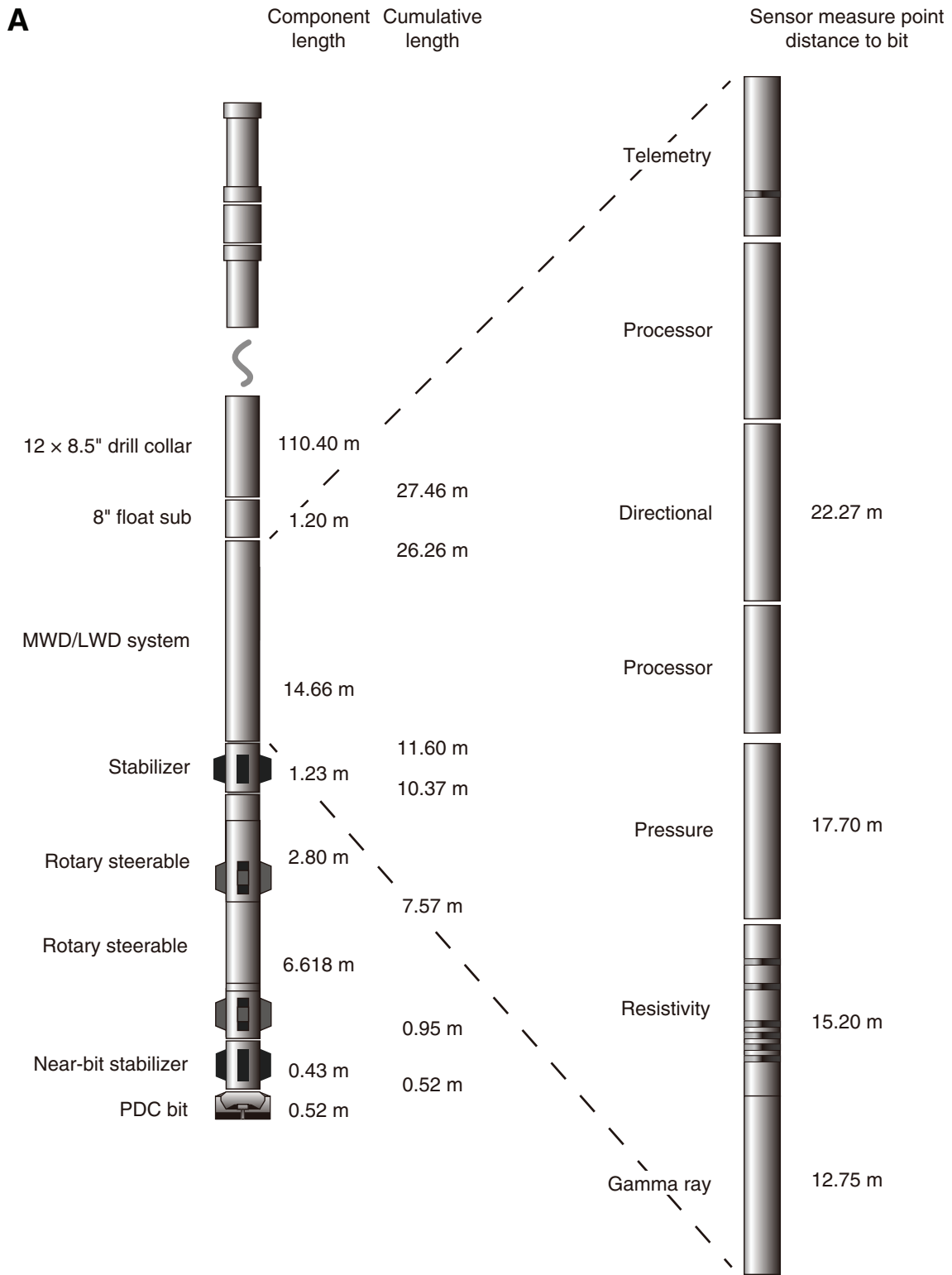


Figure F21 (continued). B. Run 2.

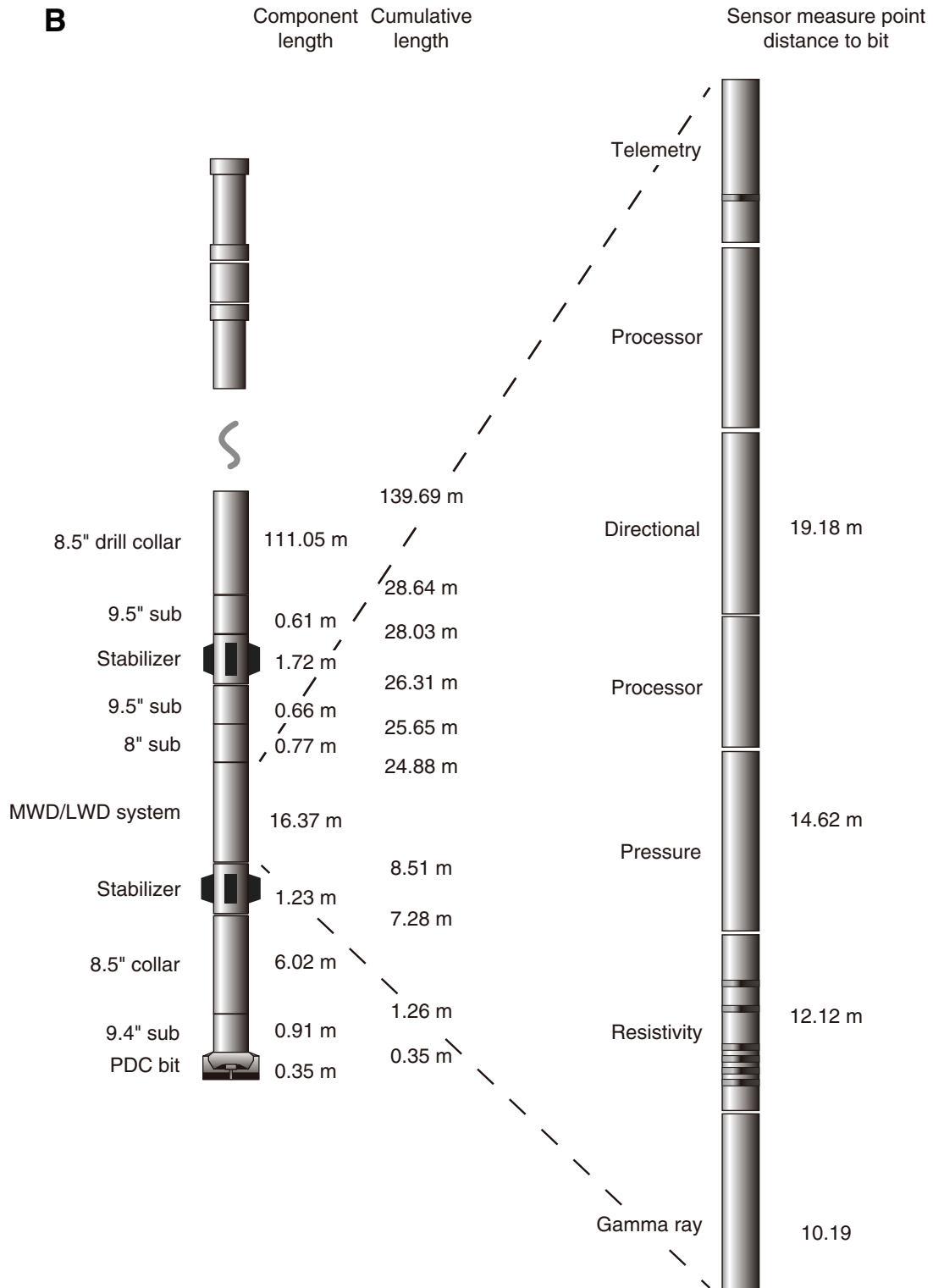


Figure F22. Measurement-while-drilling/logging-while-drilling (MWD/LWD) bottom-hole assembly 12.25 inch configuration, Hole C0002N. PDM = positive displacement motor, PDC = polycrystalline diamond compact. XBAT = X-Bimodal AcousTic sonic, EWR = electromagnetic wave resistivity, DDS = drill string dynamic sensor, AGR = azimuthal gamma ray, PWD = pressure while drilling, AFR = azimuthal focused resistivity.

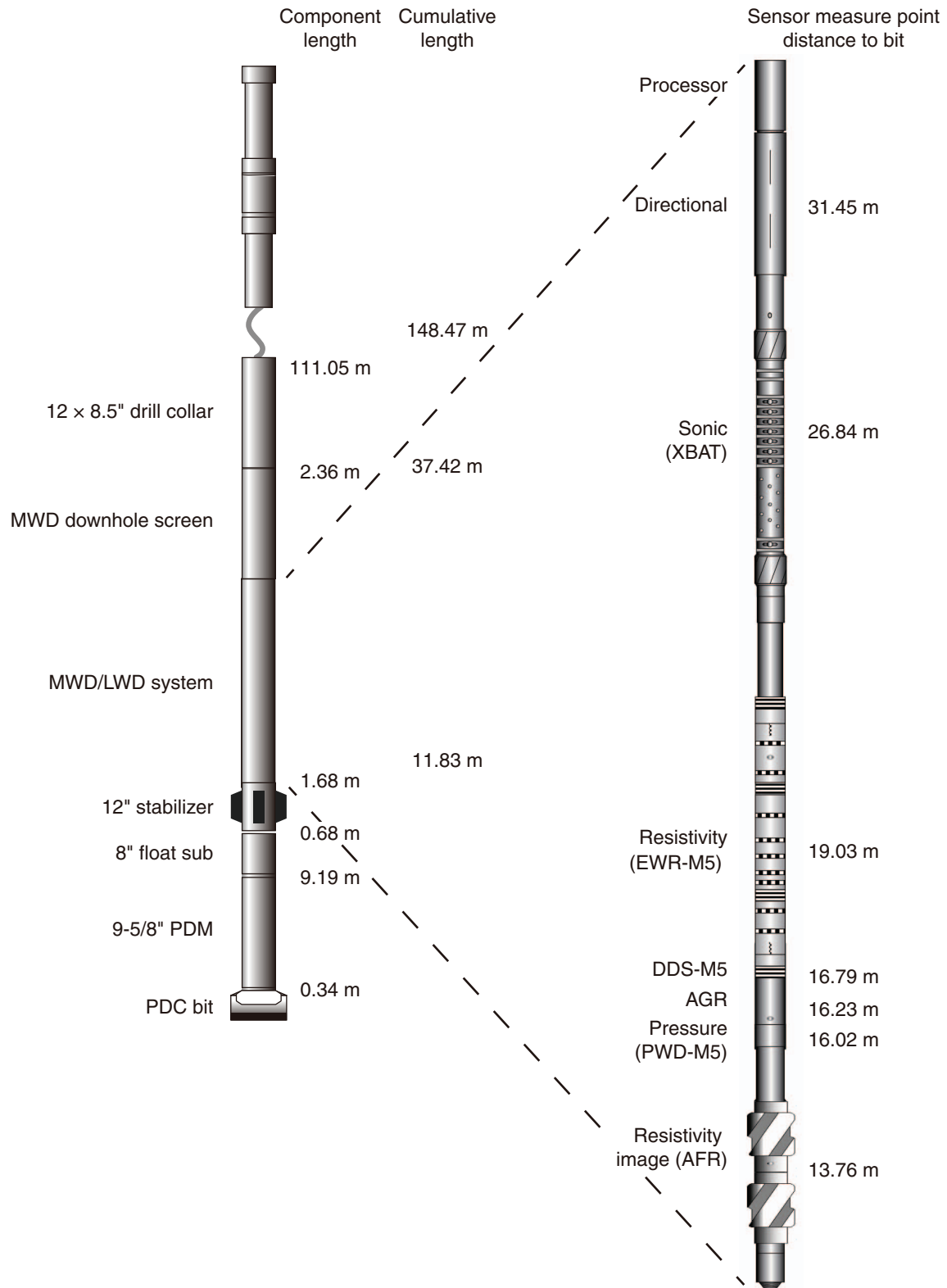


Figure F23. Electromagnetic wave resistivity (EWR)-PHASE4 tool geometry used in Hole C0002N.

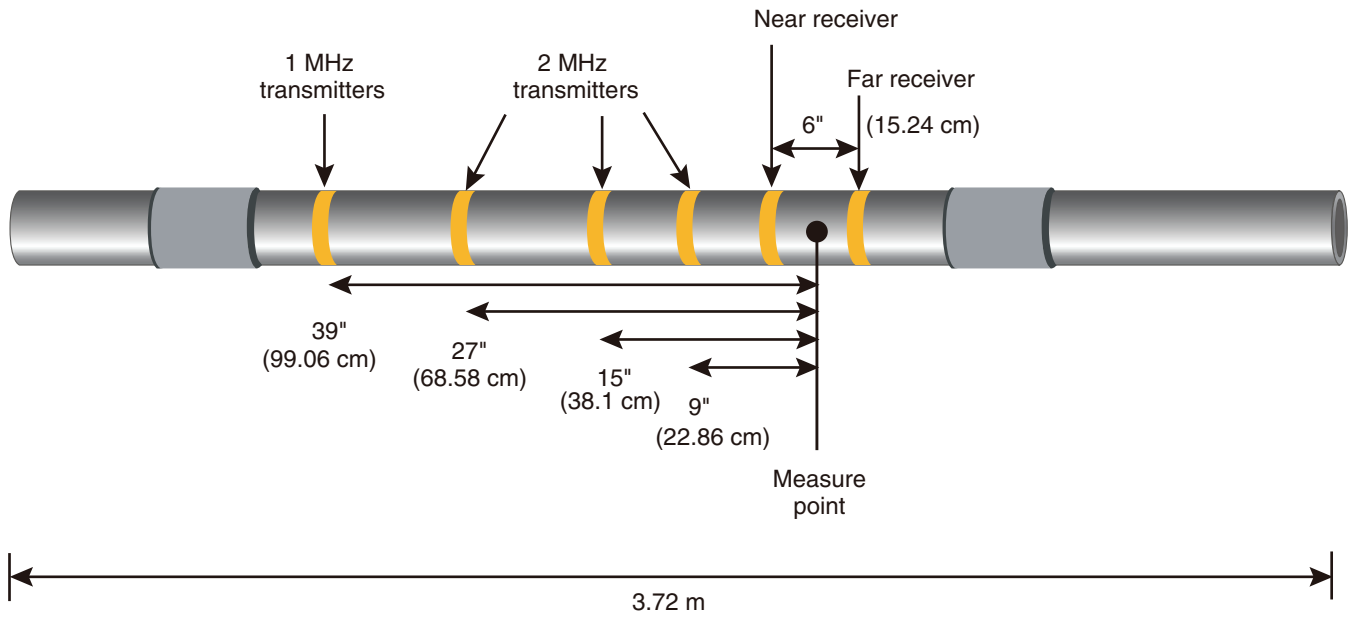


Figure F24. Electromagnetic wave resistivity (EWR)-M5 tool used in Hole C0002P, showing the locations of the six transmitters and three receivers. PWD = pressure while drilling.

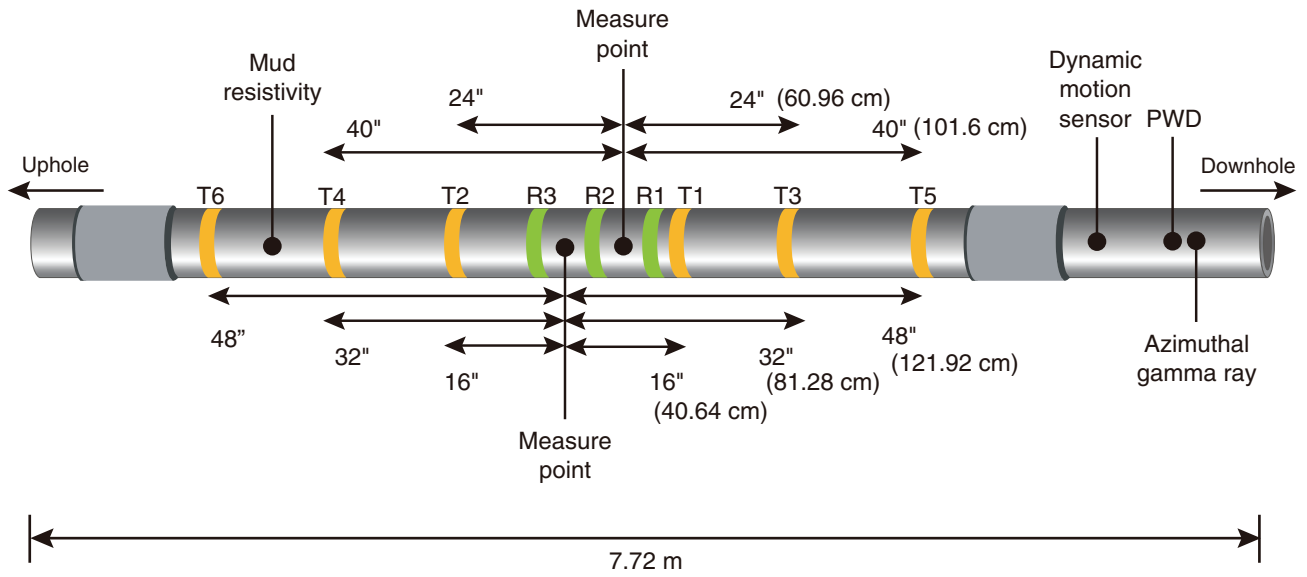


Figure F25. The 8 inch azimuthal focused resistivity (AFR) tool, with high-resolution button configuration, used in Hole C0002P.

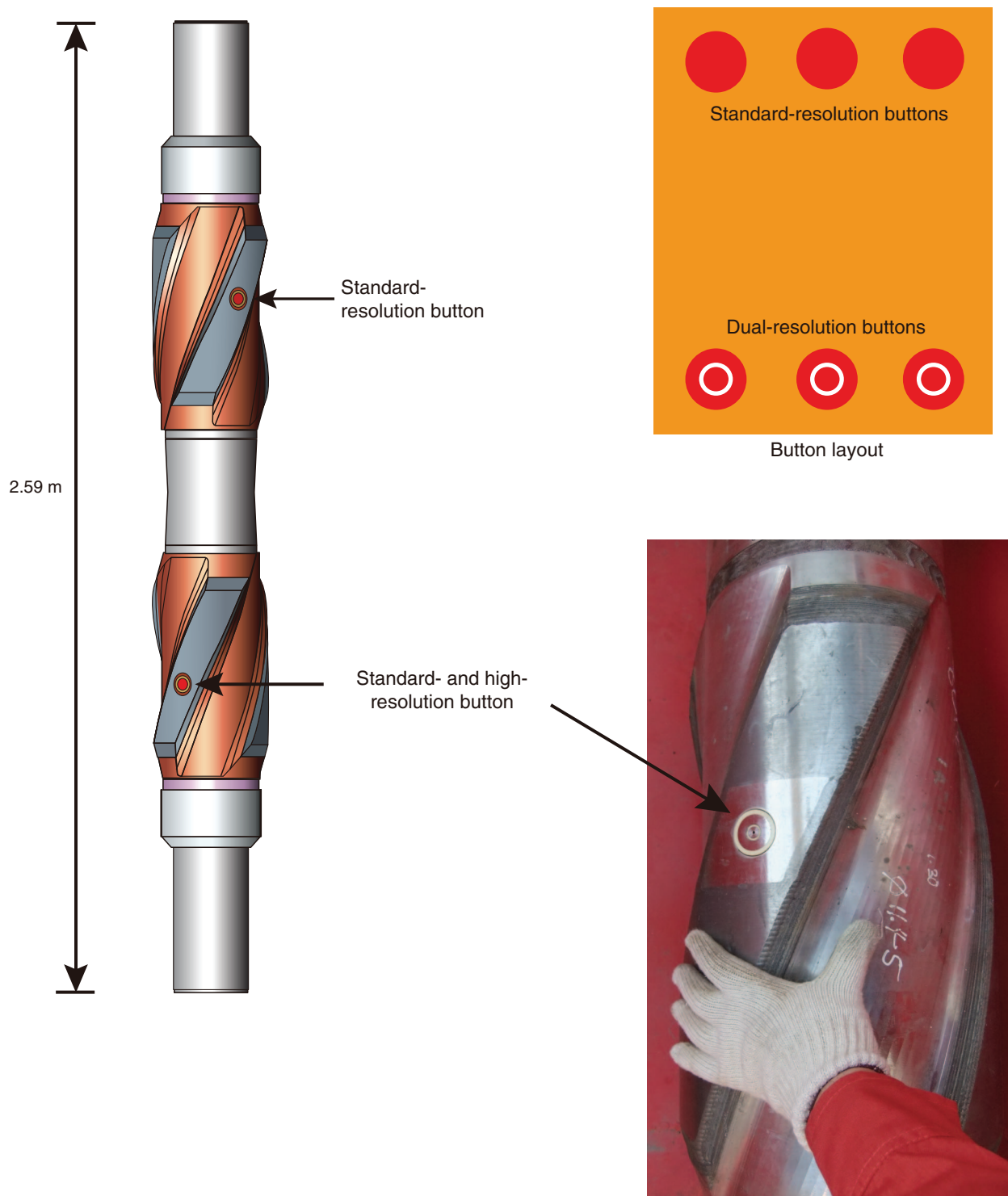
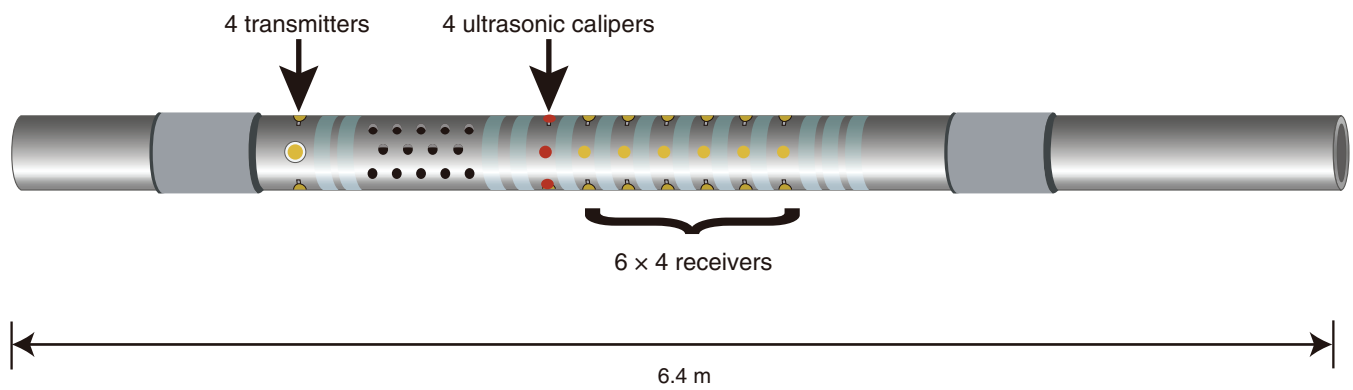


Figure F26. X-Bimodal AcousTic (XBAT) azimuthal sonic and ultrasonic measurement tool used in Hole C0002P.



**Table T1.** Integrated Ocean Drilling Program (IODP) depth scales used during Expedition 348.

Depth scale	Depth scale name	Acronym	Datum	Description	Previous unit	Type depth
Drillers	Drilling depth below rig floor	DRF	Rig floor	The sum of lengths of all drill string components deployed beneath the rig floor. Includes length of all components and the portions thereof below rig floor.	mbrf	Measured
	Drilling depth below seafloor	DSF	Seafloor	The length of all drill string components between seafloor and target.	mbsf	Processed
LWD and MWD	LWD depth below rig floor	LRF	Rig floor	The sum of lengths of all drill string components deployed beneath the rig floor reference.	mbrf	Measured
	LWD depth below seafloor	LSF	Seafloor	The length of all drill string components between seafloor and target.	mbsf	Processed
Mud	Mud depth below rig floor	MRF	Rig floor	The length of all drill string components between where cuttings and gas originate and the rig floor based on lag time of arrival at rig floor and mud pump rate.	NA	Processed
	Mud depth below seafloor	MSF	Seafloor	MRF with seafloor depth below rig floor subtracted.	NA	Processed
Core	Core depth below seafloor	CSF-A	Seafloor	Distance from seafloor to target within recovered core. Combines DSF to top of cored interval with curated section length to target within cored material. This method allows overlap at cored interval and section boundaries.	mbsf	Processed
Seismic	Seismic depth below seafloor	SSF	Seafloor	Distance below seafloor and target derived from seismic traveltime, velocity, and water depth.	m	Processed
	Seismic depth below sea level	SSL	Sea level	Distance below sea level derived from seismic traveltime and velocity.	m	Processed

LWD = logging while drilling, MWD = measurement while drilling. NA = not applicable. See IODP depth scale terminology at www.iodp.org/program-policies/procedures/guidelines.

Table T2. Correlation between measured and true vertical depths at key depths, Expedition 348.

Key location	Measured depth BRT (m)	Measured depth DSF (m)	True vertical depth DSF (m)
Seafloor	1967.5	0.0	0.0
20 inch CSG shoe	2827.8	860.3	860.3
Top of Hole C0002N (sidetrack kickoff)	2827.8	860.3	860.3
Top of Hole C0002P (sidetrack kickoff)	3904.3	1936.8	1935.4
13-3/8 inch CSG shoe	3977.5	2010.0	2008.9
Bottom of Hole C0002N	4297.5	2330.0	2328.9
Top of coring interval	4130.5	2163.0	2161.7
Bottom of coring interval	4186.0	2218.5	2216.6
11-3/4 inch CSG shoe	4890.0	2922.5	2920.65
Bottom of Hole C0002P	5026.0	3058.5	3056.6

Water depth is 1939 m below sea level. CSG = casing.

Table T3. Types of cuttings used for description and analysis, Expedition 348.

Analysis	Bulk	DICA/ pillowed cutting	Intact cutting (handpicked)	DICA		Pillowed cutting		Intact cutting (handpicked)	
				1–4 mm	>4 mm	1–4 mm	>4 mm	1–4 mm	>4 mm
Lithology	X			XX	XX	XX	XX		
Structure			X					X	X
MAD	X	X*	X	X	X	X	X		X
Magnetic susceptibility	X			X	X	X	X		
XRF	X	X*	X*	X	X	X	X		
XRD	X	X*	X*	X	X	X	X		
CARB	X	X*	X*	X	X	X	X		
NGR	X			X	X	X	X		

* = optional, DICA = drilling-induced cohesive aggregate, X = washed, XX = unwashed. MAD = moisture and density, XRF = X-ray fluorescence, XRD = X-ray diffraction, CARB = carbonate, NGR = natural gamma radiation.

Table T4. Characteristic X-ray diffraction peaks for semiquantitative analysis of composite clay minerals, quartz, plagioclase feldspar, and calcite, Expedition 348.

Mineral	Reflection	d-value (Å)	Peak position (°2θ; area)
Composite clay	Multiple	4.478	19.4–20.4
Quartz	101	3.342	26.3–27.0
Plagioclase	2	3.192	27.4–28.2
Calcite	104	3.035	29.1–29.7

Table T5. Normalization factors for calculation of relative mineral abundance using bulk powder X-ray diffraction analysis as revised during Expedition 338.

In standard mixture	Normalization factors			
	Total clay	Quartz	Plagioclase	Calcite
Influencing mineral:				
Total clay	0.11006193E-01	-0.20231483E-03	-0.29246596E-03	-0.11871842E-02
Quartz	-0.14089397E-04	0.58841606E-03	-0.24897352E-04	-0.23400669E-04
Plagioclase	0.49289758E-03	-0.71762974E-04	0.11238736E-02	-0.41371561E-04
Calcite	0.56265158E-04	-0.41641979E-05	-0.50802228E-05	0.13876300E-02

Singular value decomposition was used to compute factors, following Fisher and Underwood (1995).

Table T6. Analytical conditions for major element analysis of glass beads on the Supermini (Rigaku) X-ray fluorescence spectrometer, Expedition 348.

Element-line	Filter	Crystal	Peak angle (°)	Count time (s)	BG 1 angle (°)	Count time (s)	BG 2 angle (°)	Count time (s)	Detector
Na-K α	OUT	RX25	47,129	40	49,450	10	—	—	PC
Mg-K α	OUT	RX25	38,802	40	35,450	10	41,550	10	PC
Al-K α	OUT	PET	144,647	40	140,150	10	147,750	10	PC
Si-K α	OUT	PET	108,980	40	106,000	10	119,900	10	PC
P-K α	OUT	PET	89,360	40	91,550	10	—	—	PC
K-K α	A 140	PET	50,648	40	48,600	10	—	—	PC
Ca-K α	OUT	PET	45,176	40	43,200	10	—	—	PC
Ti-K α	OUT	LiF1	86,138	20	87,380	10	—	—	SC
Mn-K α	OUT	LiF1	62,959	20	64,380	10	—	—	SC
Fe-K α	OUT	LiF1	57,527	20	58,820	10	—	—	SC

PC = proportional counter, SC = scintillation counter. — = no data.

Table T7. Average measured values and 3 σ standard deviations for major elements determined on the Supermini (Rigaku) X-ray fluorescence spectrometer from a selection of standard samples, Expedition 348.

Major element oxide	JB-1b				JSd-1			
	Reference value (100%)	Measured value (average)	SD (3 σ)	RSD (%)	Reference value (100%)	Measured value (average)	SD (3 σ)	RSD (%)
Na ₂ O	2.687	2.678	0.154	1.900	2.815	2.807	0.167	2.000
MgO	8.318	8.475	0.123	0.500	1.872	1.809	0.058	1.100
Al ₂ O ₃	14.694	14.411	0.088	0.200	15.123	14.999	0.133	0.300
SiO ₂	52.226	52.336	0.177	0.100	68.698	68.422	0.218	0.100
P ₂ O ₅	0.262	0.263	0.014	1.800	0.126	0.124	0.009	2.500
K ₂ O	1.349	1.320	0.042	1.100	2.253	2.245	0.048	0.700
CaO	9.810	9.776	0.052	0.200	3.132	3.094	0.024	0.300
TiO ₂	1.288	1.266	0.031	0.800	0.664	0.665	0.036	1.800
MnO	0.150	0.148	0.006	1.400	0.095	0.095	0.007	2.600
Fe ₂ O ₃	9.217	9.147	0.078	0.300	5.222	5.192	0.028	0.200

SD = standard deviation, RSD = relative standard deviation.

Table T8. Astronomically calibrated age estimates of calcareous nannofossil datums used as biostratigraphic tie points, Expedition 348. (Continued on next page.)

Nannofossil event	Zone (base)	Degree of reliability	Age (Ma)
X medium <i>Gephyrocapsa</i> (>3.5 μ m)— <i>Emiliana huxleyi</i>			0.082–0.063
FO <i>Emiliana huxleyi</i>	NN21	B	0.291
LO <i>Pseudoemiliana lacunosa</i>	NN20	A	0.436
LCO <i>Reticulofenestra asanoi</i>		A	0.905–0.901*
RE medium <i>Gephyrocapsa</i> (≥ 4 μ m) and FO <i>Gephyrocapsa</i> sp. 3 (<i>G. parallela</i>)		A	1.04
FCO <i>Reticulofenestra asanoi</i>		D	1.136–1.078*
LO large <i>Gephyrocapsa</i> (>5.5 μ m)		A	1.24
LO <i>Helicosphaera sellii</i>		C	1.34
FCO large <i>Gephyrocapsa</i> (>5.5 μ m)			1.46
FO large <i>Gephyrocapsa</i> (>5.5 μ m)		B	1.560–1.617*
LO <i>Calcidiscus macintyreii</i> (≥ 11 μ m)		C	1.60
FO medium <i>Gephyrocapsa</i> (>3.5 μ m)		A	1.67
LO <i>Discoaster brouweri</i>	NN19	A	2.06
AB <i>Discoaster triradiatus</i>		A	2.135–2.216*
LO <i>Discoaster pentaradiatus</i>	NN18	C	2.393–2.512*
LO <i>Discoaster surculus</i>	NN17	C	2.52
LO <i>Discoaster tamalis</i>		C	2.87
LO <i>Sphenolithus</i> spp.		C	3.65
LO <i>Reticulofenestra pseudoumbilicus</i> (>7 μ m)	NN16	A	3.79

Table T8 (continued).

Nannofossil event	Zone (base)	Degree of reliability	Age (Ma)
FCO <i>Discoaster asymmetricus</i>	NN15–N14	B	4.13
LO <i>Amaurolithus primus</i>			4.50
LO <i>Ceratolithus acutus</i>		B	5.04
FO <i>Ceratolithus rugosus</i>	NN13	D	5.12
LO <i>Triquetrorhabdulus rugosus</i>			5.279*
FO <i>Ceratolithus acutus</i>		B	5.32
LO <i>Discoaster quinqueramus</i>	NN12	A	5.59
LO <i>Nicklithus amplificus</i>		A	5.978–5.939*
FO <i>Nicklithus amplificus</i>		C	6.909–6.684*
PE <i>Reticulofenestra pseudoumbilicus</i> (>7 µm)		D	7.077–7.167*
FO <i>Amaurolithus</i> spp./ <i>Amaurolithus primus</i>	NN11b	A	7.362–7.424*
FCO <i>Discoaster surculus</i>		B	7.88
LCO <i>Minylitha convallis</i>		D	7.78–8.3
FO <i>Discoaster berggrenii</i>	NN11a	D	8.52
PB <i>Reticulofenestra pseudoumbilicus</i> (>7 µm)	NN10b	A	8.785–8.761*
FO <i>Discoaster pentaradiatus</i>			9.1
FO <i>Minylitha convallis</i>		D	9.416
LO <i>Discoaster hamatus</i>	NN10a	C	9.560
LO <i>Catinaster calyculus</i>		D	9.674*
LO <i>Catinaster coalitus</i>		D	9.687*
X <i>Discoaster hamatus</i> – <i>Discoaster neohamatus</i>			9.762*
FO <i>Discoaster neohamatus</i>		C	9.867–10.521*
LCO <i>Discoaster exilis</i>			10.427
FO <i>Discoaster hamatus</i>	NN9	C	10.541
LO <i>Coccolithus miopelagicus</i>		C	10.613
FO <i>Discoaster calcaris</i>			10.676
FO <i>Discoaster bellus</i> gr.		C	10.72
FO <i>Discoaster brouweri</i>		A	10.734–10.764*
FO <i>Catinaster calyculus</i>		D	10.785*
FO <i>Catinaster coalitus</i>	NN8	D	10.886–10.733*
LCO <i>Discoaster kugleri</i>		A	11.578–11.596*
FCO <i>Discoaster kugleri</i>	NN7	B	11.863–11.905*
LO <i>Cyclicargolithus floridanus</i>		D	12.037
LO <i>Coronocyclus nitescens</i>			12.254
LCO <i>Calcidiscus premacintyreii</i>		A	12.447
FCO <i>Triquetrorhabdulus rugosus</i>			12.671
LCO <i>Cyclicargolithus floridanus</i>		A	13.294
LO <i>Sphenolithus heteromorphus</i>	NN6	C	13.532–13.654*
LO <i>Helicosphaera ampliapertura</i>	NN5		14.914*
AE <i>Discoaster deflandrei</i>			15.663*
FO <i>Discoaster signus</i>			15.702*
FCO <i>Sphenolithus heteromorphus</i>			17.721*
LCO <i>Sphenolithus belemnus</i>	NN4		17.973*
LO <i>Triquetrorhabdulus carinatus</i>		D	18.315*
FO <i>Sphenolithus belemnus</i>	NN3		18.921*
FO <i>Helicosphaera ampliapertura</i>			20.393*
X <i>Helicosphaera euphratis</i> – <i>Helicosphaera carteri</i>			20.894*
FCO <i>Helicosphaera carteri</i>			21.985*
LCO <i>Triquetrorhabdulus carinatus</i>			22.092
FO <i>Sphenolithus disbelemnus</i>		C	22.413
FO <i>Discoaster druggii</i>	NN2	D	22.824*
LO <i>Sphenolithus delphix</i>		A	23.089
FO <i>Sphenolithus delphix</i>		A	23.356
LO <i>Sphenolithus ciperoensis</i>	NN1	C	24.389

Datums are based on Pacific records if not otherwise stated; an asterisk (*) denotes datums based on Atlantic or Mediterranean records. Age estimates adopted from Raffi et al. (2006). Nannofossil event: X = abundance crossover, FO = first occurrence, LO = last occurrence, LCO = last consistent occurrence, RE = reentrance, FCO = first consistent occurrence, AB = acme beginning, AE = acme end, PE = paracme end, PB = paracme beginning. Degree of reliability: A = distinct, well defined, and isochronous worldwide; B = indistinct and less well defined but reasonably isochronous; C = distinct and well defined but diachronous; D = indistinct, poorly defined, and diachronous. See Raffi et al. (2006) for detailed explanation.

Table T9. Ages used for geomagnetic polarity timescale, Expedition 348.

Interval (Ma)		Chron/ Subchron
Top	Bottom	
0	0.781	C1n
0.988	1.072	C1r.1n
1.173	1.185	C1r.2n
1.778	1.945	C2n
2.581	3.032	C2An.1n
3.116	3.207	C2An.2n
3.33	3.596	C2An.3n
4.187	4.3	C3n.1n
4.493	4.631	C3n.2n
4.799	4.896	C3n.3n
4.997	5.235	C3n.4n
6.033	6.252	C3An.1n
6.436	6.733	C3An.2n
7.14	7.212	C3Bn
7.251	7.285	C3Br.1n
7.454	7.489	C3Br.2n
7.528	7.642	C4n.1n
7.695	8.108	C4n.2n
8.254	8.3	C4r.1n
8.769	9.098	C4An
9.321	9.409	C4Ar.1n
9.656	9.717	C4Ar.2n
9.779	9.934	C5n.1n
9.987	11.04	C5n.2n
11.118	11.154	C5r.1n
11.554	11.614	C5r.2n
12.041	12.116	C5An.1n
12.207	12.415	C5An.2n
12.73	12.765	C5Ar.1n
12.82	12.878	C5Ar.2n
13.015	13.183	C5AAn
13.369	13.605	C5ABn
13.734	14.095	C5ACn
14.194	14.581	C5ADn
14.784	14.877	C5Bn.1n
15.032	15.16	C5Bn.2n
15.974	16.268	C5Cn.1n
16.303	16.472	C5Cn.2n
16.543	16.721	C5Cn.3n
17.235	17.533	C5Dn
18.056	18.524	C5En
18.748	19.722	C6n
20.04	20.213	C6An.1n
20.439	20.709	C6An.2n
21.083	21.159	C6AAn
21.659	21.688	C6AAr.2n
21.767	21.936	C6Bn.1n
21.992	22.268	C6Bn.2n
22.564	22.758	C6Cn.1n
22.902	23.03	C6Cn.2n

Data from Lourens et al., 2004.

Table T10. Applied pressures for standard squeezing and GRIND methods, Expedition 348.

Core, section, interval (cm)	Depth (mbsf)	Water aliquot/ Method	Applied pressure steps and time (lb/min)	Applied maximum force (lb)	Applied maximum pressure (MPa)
348-C0002M-1R-1, 87–107	475.00	A	15,000/5; 17,000/7; 20,000/10	20,000	37
		B	21,500/10; 23,000/10; 25,000/10	25,000	47
		C	30,000/10; 40,000/10; 50,000/10; 60,000/720	60,000	112
2R-2, 111–131	485.91	A		20,000	37
		B		25,000	47
		C		60,000	112
3R-1, 90–110	493.50	A		20,000	37
		B		25,000	47
		C'	30,000/10; 40,000/10; 50,000/10	50,000	94
		C''	60,000/720	60,000	112
4R-2, 113–133	504.41	A		20,000	37
		B		25,000	47
		C'		50,000	94
		C''		60,000	112
348-C0002P-2R-3, 96–137.5	2176.28	GRIND	5,300/75; 10,700/67	5,300	11
				10,700	20
3R-2, 84–104	2184.25	GRIND	5,300/95; 10,700/59	5,300	11
				10,700	20
4R-2, 47–57	2193.08	GRIND	5,300/87; 10,700/82	5,300	11
				10,700	20
5R-2, 89–99	2203.33	GRIND	5,300/72; 10,700/67	5,300	11
				10,700	20
6R-2-1, 80–90	2211.21	GRIND	5,300/70; 10,700/190; 16,000/1125	5,300	11
				10,700	20
				16,000	30
6R-2, 80–90	2211.21	GRIND	5,300/72; 10,700/190; 16,000/340	5,300	11
				10,700	20
				16,000	30

Press calibration was done on 24 December 2013. GRIND = ground rock interstitial normative determination.

Table T11. Background gas concentrations in drilling mud water, Expedition 348.

Mud-water sample	Methane (ppmv)	Ethane (ppmv)	Propane (ppmv)	Depth MSF (m)
39-LMW	2.68	0.00	0.00	2067.5
41-LMW	2.49	0.00	0.00	2067.5
55-LMW	13.15	0.19	0.00	2128.5
65-LMW	12.92	0.20	0.00	2162.5
68-LMW	2.33	0.00	0.00	2107.5
75-LMW	5.75	0.00	0.00	2191.5
80-LMW	7.33	0.00	0.00	2200.5
84-LMW	4.61	0.00	0.00	2217.5
87-LMW	6.37	0.00	0.00	2218.5
119-LMW	7.88	0.00	0.00	2298.5
153-LMW	20.95	0.39	0.00	2450.5
194-LMW	28.04	1.09	0.00	2599.5
212-LMW	31.67	1.64	0.00	2679.5
252-LMW	29.36	1.85	0.00	2832.5
275-LMW	45.76	2.15	0.55	2982.5
301-LMW	16.92	1.21	0.00	3057.5
303-LMW	18.15	1.02	0.00	3057.5

Table T12. Measurement performance specifications for the azimuthal focused resistivity (AFR) tool, Expedition 348.

Feature	Specification
Operating frequencies (kHz)	4 and 36
Resistivity measurement operating range (Ωm)	0.2 to 20,000
Resistivity measurement accuracy (Ωm)	0 to 200 \pm 2% 500 \pm 3% 1,000 \pm 10% 2,000 \pm 20% >10,000—gross indication of change
Depths of investigation (mm)	76 and 254 from borehole wall
Azimuthal bins (mm)	64 (standard) and 128 (high resolution)
Image resolution (mm)	25 (standard) and 10 (high resolution)
Mud resistivity operating range (Ωm)	0.01–10
Mud resistivity measurement accuracy (Ωm)	5% for conductivity <1 10% for conductivities between 1 and 10 20% for conductivities >10
Power supply	Lithium battery
Memory size (GB)	1

Table T13. Measurement performance specifications for the azimuthal sonic and ultrasonic tools, Expedition 348.

Feature	Specification
Normal tool OD	8 inches; 203 mm
Hole sizes	10-5/8 to 12-1/4 inches; 270–311 mm
Length	21 ft; 6.4 m
Weight	2,940 lb; 1,334 kg
Connections	6-5/8 reg box \times box
Make-up torque	46,000–49,000 ft-lb; 62.5–66.6 kNm
Max dogleg severity	
Rotating	8°; 100 ft
Nonrotating	14°; 100 ft
Maximum operating temperature	302°F; 150°C
Maximum pressure	30,000 psi; 2,069 bar
Maximum mass flow rate	20,000 lb/min; 9,072 kg/min
Maximum sand content	2%
Typical pressure loss	
250 gal/min; 950 L/min	4 psi; 0.3 bar
450 gal/min; 1700 L/min	13 psi; 0.9 bar
1200 gal/min; 4550 L/min	76 psi; 5.2 bar
Transducer type	Piezoelectric
Measurements	dT compressional, dT shear (refracted and slower than fluid)
Operating range	dT compressional $-40 \sim +180 \mu\text{s/ft}$; dTt shear $-60 \sim +550 \mu\text{s/ft}$
Accuracy	
dt compressional and refracted shear	$\pm 1 \mu\text{s/ft}$
dt slow shear	$\pm 2.5 \mu\text{s/ft}$
Measurement point from	9 ft; 2.74 m
Bottom of tool	8.8 ft; 2.7 m
Equivalent bending stiffness	7.53 inches OD \times 2.81 inches ID; 191 mm OD \times 71 mm ID
Power supply	Battery
Downhole memory capacity	2 GB
Standoff measurement	± 0.1 inch; 2.54 mm
Accuracy	
Range at <12 lb/gal	4 inches; 10.16 cm
Range at 12–15 lb/gal	2.5 inches; 6.35 cm
Range at >15 lb/gal	1.5 inches; 38.1 cm
Hole size and shape	± 0.15 inch; 3.81 mm
Maximum hole size	Tool OD + 2 \times maximum range

OD = outer diameter, ID = inner diameter.

Table T14. Logging-while-drilling tool acronyms, Expedition 348.

Acronym	Tool name	Tool type
ABG	At-bit gamma ray	Gamma ray sensor
ACAL	Acoustic caliper	Caliper
ADR	Azimuthal deep resistivity	Propagation resistivity
AFR	Azimuthal focused resistivity	Laterolog imager
AGR	Azimuthal gamma ray	Gamma ray sensor
BAT	Bimodal acoustic tool	Sonic sensor
DDS	Drill string dynamics sensor	Vibration and shock sensors
DDS2	Drill string dynamics sensor 2 (mounted in EWR-M5)	Vibration and shock sensors
DGR	Dual gamma ray	Gamma ray sensor
DM	Directional module	Directional survey of wellbore inclination and azimuth
DrillDOC	Drilling downhole optimization collar	Weight, torque, and bending moment
EWR-M5	Electromagnetic wave resistivity – 5 spacings	Multispacing propagation resistivity sensor
EWR-P4	Electromagnetic wave resistivity – phase	Multispacing propagation resistivity sensor
GABI	Gamma ray and at-bit inclination	Gamma ray sensor
GM	Gamma module	Gamma ray module
HCIM	Central interface module	Processor of tool string
IVSS	Insert vibration severity sensor	Vibration sensor
PWD	Pressure while drilling	Real-time borehole pressure sensor
TM	Telemetry module	Real-time telemetry sensor
XBAT	Telemetry module real-time telemetry sensor	Real-time telemetry sensor

Table T15. Logging-while-drilling log identifier descriptions and units, Expedition 348.

Log	Description	Unit
DEPT	Reference depth	m
DGRCC	DGR combine gamma ray	gAPI
EWTEMP	EWR temperature	°C
EWXT	EWR formation expedition time	h
PWEA	PWD annular EMW	lb/gal
PWPA	PWD annular pressure	psig
R09AC	9 inch attenuation resistivity BC	Ωm
R09PC	9 inch phase resistivity BC	Ωm
R15AC	15 inch attenuation resistivity BC	Ωm
R15PC	15 inch phase resistivity BC	Ωm
R27AC	27 inch attenuation resistivity BC	Ωm
R27PC	27 inch phase resistivity BC	Ωm
R39AC	39 inch attenuation resistivity BC	Ωm
R39PC	39 inch phase resistivity BC	Ωm
ROPA	Average rate of penetration	ft/h

DGR = dual gamma ray, EWR = electromagnetic wave resistivity, PWD = pressure while drilling, BC = borehole compensated.